Toward a Robust Electromagnetic Tracking System for Use in Medical Applications

Der Fäkultät für Elektrotechnik und Informationstechnik der
Otto-von-Guericke-Universität Magdeburg zur Erlangung des akademischen Grades

Doktoringenieur
(Dr.-Ing.)

am 07.08.2017 vorgelegte Dissertation
von M.Sc. Mengfei Li.

Contents

List of Figures

List of Tables

Abstract

Electromagnetic tracking systems have become increasingly used in clinical contexts, primarily employed in assisting image–guided surgery in the last decades. The non–line–of–sight requirement of electromagnetic tracking systems makes it especially appealing for particular tracking applications, such as the navigation of flexible instruments inside the patient's body. Manufacturers have offered generations of commercially available electromagnetic tracking systems for use in clinical applications. Nevertheless, significant tracking errors caused by metallic objects in the operating room located in proximity to the magnetic sensor coil remain an unresolved problem that limits the technology's wider application.

The primary focus of this thesis is to introduce a novel approach to the dynamic reduction of the sensor pose errors, caused by the proximate conductive material. Instead of using sine–wave signals, this method applies ramp excitations as the system input, which has been implemented in the system prototype and statistically evaluated.

For the system to achieve the most real–time application possible, a rapid data acquisition method has been developed to improve the refresh rate in sensor pose estimation up to $12.7Hz$. The suggested method applying ramp excitations requires no hardware modifications to improve the tracking robustness due to sources of metallic distortions in proximity. This software–based method can potentially also be implemented in commercial systems to improve the safety and outcome of image–guided surgeries.

Additionally, this thesis introduces an electromagnetic tracking simulator developed by the author, which allows performing advanced system analysis without any hardware requirement. Based on the simulator, an optimization of the transmitter coils' spatial placement has been performed. Other system parameters and theoretical performances of EM tracking systems have been systematically evaluated using the simulator.

The background of electromagnetic tracking technology, the range of its clinical applications, and system construction have also been discussed in this dissertation.

Zusammenfassung

Elektromagnetische Trackingsysteme werden immer häufiger im klinischen Umfeld eingesetzt, insbesondere bei der Unterstützung der bildgeführten, minimalinvasiven Chirurgie. Im Gegensatz zu optischen Tracking benötigen die elektromagnetischen Systeme keine Sichtverbindung, so dass diese auch für die Navigation von flexiblen Instrumenten im Körper des Patienten genutzt werden können. Das größte Problem der kommerziell erhältlichen Systeme ist jedoch, dass diese durch metallische Objekte, welche sich in der Nähe der magnetischen Sensorspule befinden, gestört werden. Der daraus resultierende Fehler bei der Bestimmung der Positionsgenauigkeit ist ein noch weitgehend ungelöstes Problem, welches die breite Anwendung der Technologie begrenzt.

Im Mittelpunkt dieser Dissertation steht die Untersuchung und Entwicklung eines neuartigen Ansatzes zur dynamischen Reduktion von Fehlern bei der Positionsbestimmung elektromagnetischer Trackingsysteme, welche durch elektrisch leitfähige Materialien verursacht werden. Zur Lösung dieser Problematik wurde die herkömmliche Anregung der magnetischen Sendespulen modifiziert. Anstelle von Sinussignalen benutzt die neu entwickelte Methode Rampensignale am Systemeingang. Mithilfe dieses Verfahrens konnte der durch leitende Objekte verursachte Fehler bei der Positionsbestimmung deutlich reduziert werden. Das entwickelte Verfahren, welches ausschließlich auf einer Modifikation der Eingangssignale beruht, erfordert keine Modifikation der Hardware. Somit kann es prinzipiell auch in kommerziellen Systemen implementiert wer-

den, um die Sicherheit und das Ergebnis von minimalinvasiven Operationen zu verbessern. Um eine bestmögliche Echtzeitanwendung des Trackingsystems zu gewährleisten wurde die Datenerfassungsmethode optimiert, wodurch eine Abtastfrequenz von $12,7Hz$ erreicht wurde.

Darüber hinaus stellt diese Dissertation einen vom Autor entwickelten Simulator für elektromagnetische Trackingsysteme vor, welcher eine fortgeschrittene Systemanalyse ohne jegliche Hardwarebeschränkungen erlaubt. Basierend auf dem Simulator wurde eine Optimierung der räumlichen Platzierung der Sendespulen durchgeführt. Andere Systemparameter und theoretische Leistungen von elektromagnetischen Trackingsystemen wurden systematisch mit dem Simulator ausgewertet.

Der Hintergrund der elektromagnetischen Trackingtechnologie sowie das vielfältige Spektrum der klinischen Anwendungen und der Systemaufbau wurden in dieser Dissertation ebenfalls diskutiert.

Chapter 1

Introduction

1.1 Overview

This chapter draws an outline of the thesis. The clinical applications of electromagnetic tracking systems (EMTS) are introduced here, as well as the technology's advantages and restrictions. The motivation and the structure of the dissertation are presented.

X–ray scans and computed tomography (CT) are the most commonly applied imaging modalities used during image-guided surgeries (IGS). [CP10]. The biggest obstacle to CT–guided surgery is the length of X–ray radiation exposure experienced by patients and clinicians [Fre04], which poses clinical safety issues. Consequently, medical navigation systems have been proposed to provide instrument tracking information to assist IGS.

Mechanic, ultrasound, optic, and electromagnetic tracking technologies are currently the most frequently applied tracking modalities used during IGS. Among them, optical tracking systems (OTS) and EMTS are the most popular, and each is extensively employed in different clinical applications [BHWC08]. While both system types present their own benefits and limitations, OTSs are much more accurate in a relatively large working volume [WTF04, Glo09]. The main drawback for OTS

Figure 1.1: The principle of EMTS for intra–operative applications. (Image Source: [FHB+14])

is its line–of–sight requirement, which limits the application scope of OTS, such as flexible instrument tracking inside of the patients' bodies. For EMTS, the tiny magnetic sensors integrated into tips of needles and catheters, thus make the EMTS ideal for flexible tracking in soft tissue or vascular systems [NHP+07, PBI+09]. Since the concept of electromagnetic tracking firstly appeared in the patent in 1975 [Kui75], the technology has been significantly advanced by manufacturers and researchers over the last few decades. Manufacturers today provide magnetic sensor coils that are small enough to be mounted in the tips of different medical instruments such as needles and catheters [YWLC09]. During surgical procedures, EMTS navigate the position and orientation (pose) of the tracker tool relative to the patients' pre–scanned anatomy. The principle of clinical EMTS is presented in Figure 1.1.

As presented in Figure 1.1, the patient is fixed on a surgical table during a typical intra–operative procedure. The field generator (FG) of

EMTS, which produces low–frequency magnetic fields, is positioned close to the surgical region of interest (SROI). The EMTS navigates the pose of the sensor inside patients' bodies in real time. After registering the pre–scanned patient anatomy with the three–dimensional (3D) space of the EMTS, the relative sensor poses inside of the patients' bodies can be acquired. Results from multiple studies have shown that EMTSs are compatible with CT–, C–arm– [NHP+07, SHOM15, LSP+15], and ultrasound (US–) guided [FHB+14, SHA+16] interventional therapies in providing reliable tracking data on surgical instruments.

For other specific surgical applications, EMTS have been evaluated to be sufficiently accurate at providing tracking information for needle–based thermal ablation and biopsy guidance [KXG+07]. A feasibility study on interventional radiology was also performed by Wood *et al.* [WZD+05], to prove that EMTS allow real–time medical instrument tracking during angiography. A preliminary study on the use of an EMTS in abdominal procedures was performed using phantom and animal tests [PGMH05]. Moreover, EMTS were also proven to be sufficiently precise, being for use in needle–based spine surgeries [BPN+09], and it has been used in dental Implantology [EST+04a], endoscopic sinus surgery [RTL+02], neck mobility measurement [KWVH03], and eye tracking [PSPK10] among other applications. Franz *et al.* reported [FHB+14], that more than 79 scientific papers documenting the clinical applications of EMTS had already appeared on *PubMed*.

1.2 Clinical Requirements

To provide precise tracking information while meeting the clinical safety issues, the important features of electromagnetic tracking systems have been discussed in the literature. The following features are the most vital requirements for EMTS to be utilized in clinical applications.

Tracker Accuracy. As is reported in the literature [YWLC09], system accuracy is one of the most significant challenges to the clinical application of EMTS. The pose of the medical instruments' tips must be precisely tracked to ensure safety during IGS. Multiple studies have been conducted to evaluate commercially available EMTSs. Both the technical tracking accuracy [FWLK03, KKK13, LAH03] and actual tracking accuracy during intra–operative procedures [FKG+97] have been reported. The results have shown that EMTS are sufficiently precise for use in clinical applications in metal–free environments [PA02].

Volume of Interest. While commercial OTSs, such as the *NDI Polaris Spectra* (Northern Digital, Canada), which has an up to $1.6m^3$ pyramid volume for highly accurate tracking [WTF04], EMTS generally has a much smaller volume. Within a cube volume with the size of $500mm \times 500mm \times 500mm$, the commercial EMTS was reported to have a small root–mean–square (RMS) tracking error in the range of $1mm$ [BHWC08]. The jitter error becomes larger as the distance between the transmitter and the sensor increases. To ensure sufficient tracking accuracy for IGS, the field generator should be placed near to the SROI–typically below the surgical table or directly facing the patient using an additional arm support.

Refresh Rate. The fast system refresh rate in updating estimated sensor pose signal is another important feature for real–time applications. The *NDI Aurora* (Northern Digital, Canada), a commercially available EMTS, has a refresh rate of $40Hz$ for single–coil and $25Hz - 30Hz$ for multiple–coil tracking, which was reported to be sufficiently fast for real–time guidance[YWLC09].

Robustness. System robustness is another significant clinical requirement of EMTS. The system should not be negatively affected by the

ambient environment in the OR. Generally, an EMTS's tracker accuracy is influenced by proximate objects, such as surgical instruments, surgical tables, imaging apparatus, and other electronic devices. The sources of distortions are not easy to be noticed by clinicians, which may endanger patient safety during IGS. Where the sources of distortions cannot be removed, EMTSs with weak robustness are not always reliable [BWW+98, WBW+99, YWLC09, BRF+15]. This is the primary obstacle preventing the wider acceptance of EMTSs in clinical applications.

Other Features. In addition to the frequently discussed requirements listed above, other features often referred to in the literature include multiple sensor tracking, system stability, and five and six degrees–of–freedom (DOF) tracking capability [YWLC09]. As these issues have already been well resolved by manufacturers, they will not be further discussed in this thesis.

1.3 Thesis Objectives

While EMTS have existed for over 40 years and are widely applied in clinical settings, their weak robustness to metallic interference is still a critical issue, i.e. the tracker accuracy is significantly reduced by metal objects located in proximity to the magnetic sensor coil.

Distinct sources of metallic distortions exist in all clinical OR during surgical interventions and therapies; examples include the metallic drill body used in dental implant surgery [WBW+99], such as the metallic arm support placed near the tracker tool in interstitial brachytherapy treatments [BRF+15] and electronic devices e.g. ultrasound scanner probes [BWW+98]. Most of the methods listed in the literature concentrate on reducing the errors caused by stationary distorters in the OR. For the distortions resulted from mobile instruments and devices, there are no

perfect solutions without the demand of extra hardware or large changes in the established clinical workflows [LHR17].

This thesis aims to introduce a software–based solution to the development of an accurate and robust EMTS that can significantly reduce sensor positioning errors caused by nearby metallic objects in real time.

Additionally, this thesis introduces an EMTS simulator developed by the author that allows for an advanced analysis of theoretical performance. System parameters can be individually and systematically studied using this simulator without the need to take electrical noises and other real-life uncertainties into consideration.

1.4 Thesis Structure

This thesis is divided into five main work chapters.

Chapter 1 is an introduction to the use of EMTS in clinical applications and presents the technology's features and limitations.

Chapter 2 provides background information on electromagnetic tracking technology and presents an overview of the commercially available systems and the prototype developed by research groups around the world. The hardware of the author's EMTS prototype is also discussed.

Chapter 3 introduces a novel concept that uses ramp signals as system input excitation signal for EMTS to reduce the tracking errors caused by proximate metallic materials. The theory, methods have been introduced in this chapter. Using the developed EMTS prototype, the proposed method was comprehensively evaluated.

Chapter 4 examines field programmable gate array (FPGA)–based implementations of signal generation and data acquisition. Band–pass filters (BPF) were implemented in the FPGA to enable the parallel executions and to accelerate tracking processes for the sine–wave excitation based method. In order to increase the refresh rate of the ramp–excitation–based method, an approach to moving–average–like data ac-

quisition was developed and realized by using multiple first in, first out (FIFO) element in the FPGA. Direct memory access (DMA) was applied to transfer the data between the FPGA and the host PC.

Chapter 5 presents a fully self–developed software tool that simulates the entire tracking processes. The ground truth of the sensor poses can be directly defined in the simulator without considering the errors caused by the reference positioning systems and registration processes. Additionally, sources of errors can be analyzed separately in the simulator, which is not possible for the real-world system. Further, advanced system analyses were conducted using the simulator, including an evaluation of Kalman filtering performance.

Lastly, the main findings of this thesis are listed and discussed in Chapter 6. Proposed future works regarding further improvements to system performance, which allow for real clinical applications, are also discussed.

Chapter 2

Background in EM Tracking

2.1 Chapter Overview

This chapter concentrates on introducing the background of electromagnetic tracking technology. Firstly, the principle of the EM tracking technology is introduced. After that, the widely applied commercial EMTS and the various system setups proposed by global groups have been surveyed and discussed. The setup of the self–developed EMTS prototype is also introduced in this chapter.

2.2 Background Theory

The 5–DOF EM sensor is most commonly applied in clinical settings [FHB+14]. For the 6-DOF tracker, at least one additional sensor coil is needed to provide the tracker' rotation. For catheter or needle based navigation, the tracker's rotation is generally not necessary to be measured.

Based on measuring the voltages induced in the sensor coil to get the gradient of the magnetic field flux density [Han86], EMTS estimate the sensor position – along three axes in the Cartesian coordinate system, and orientation – pitch and yaw Euler angles of the small–sized

magnetic sensor coil. EMTS have commonly multiple transmitter coils and at least one sensor coil [RBSJ79], in order to simulate the magnetic field generated by the transmitter coils in a 3D space, the magnetic dipole model was widely employed to simplify the computational process [SHL+13a, DDSR95, SS07].

For a typical 5–DOF EMTS, multiple transmitter coils and one magnetic sensor were required to build up the system. The calculation of magnetic dipole moment of the transmitter coil is given by:

$$\overrightarrow{m_{t,i}} = \pi \cdot N_{t,i} \cdot I_{t,i} \cdot R_{t,i}^2 \cdot \overrightarrow{r_{t,i}} \cdot \begin{pmatrix} \sin\Theta_{t,i}\cos\Phi t, i \\ \sin\Theta_{t,i}\sin\Phi t, i \\ \cos\Theta_{t,i} \end{pmatrix}. \tag{2.1}$$

Here, $N_{t,i}$ is the turns of the $i-th$ transmitter coil. $I_{t,i}$ is the current flow and $R_{t,i}$ is the radius, $\Phi_{t,i}$ and $\Theta_{t,i}$ are the pitch and yaw Euler angles of the $i-th$ transmitter coil. The magnetic dipole moment is a vector along each axis in 3D Cartesian coordinate system.

$$\overrightarrow{m_{t,i}} = \begin{pmatrix} \overrightarrow{m_{X_{t,i}}} \\ \overrightarrow{m_{Y_{t,i}}} \\ \overrightarrow{m_{Z_{t,i}}} \end{pmatrix}. \tag{2.2}$$

Using the magnetic dipole moment simplifies the calculation of the magnetic field flux density. The calculation is given as:

$$\overrightarrow{B_i} = \frac{\mu}{4\pi}\left(\frac{(3(\overrightarrow{x_s} - \overrightarrow{r_{t,i}}) \cdot (\overrightarrow{m_{t,i}} \cdot (\overrightarrow{x_s} - \overrightarrow{r_{t,i}}))}{|\overrightarrow{x_s} - \overrightarrow{r_{t,i}}|^5} - \frac{\overrightarrow{m_{t,i}}}{|\overrightarrow{x_s} - \overrightarrow{r_{t,i}}|^3}\right). \tag{2.3}$$

In this equation, $\overrightarrow{x_s} = \begin{pmatrix} X_s \\ Y_s \\ Z_s \end{pmatrix}$ is the position of the sensor coil and $\overrightarrow{r_{t,i}} = \begin{pmatrix} X_{t,i} \\ Y_{t,i} \\ Z_{t,i} \end{pmatrix}$ is the position of the $i-th$ transmitter coil towards X, Y

and Z direction in the 3D Cartesian coordinate system of the magnetic field. The B-field vector is given by:

$$\overrightarrow{B_i} = \begin{pmatrix} B_{X_i} \\ B_{Y_i} \\ B_{Z_i} \end{pmatrix}. \tag{2.4}$$

By knowing the magnetic field flux density and the parameters of the transmitter and sensor coil, the voltage induced across the magnetic sensor coil is given by:

$$\overrightarrow{U_{est,i}} = \omega \cdot A_s \cdot N_s \cdot \overrightarrow{B_i} \cdot \begin{pmatrix} \sin\Theta_s \cos\Phi s \\ \sin\Theta_s \sin\Phi s \\ \cos\Theta_s \end{pmatrix}. \tag{2.5}$$

Wherein, ω is the angular frequency of the generated alternating–current (AC) magnetic field: $\omega = 2\pi f$, A_s is the cross–sectional area of the sensor coil, and N_s is the number of the turns of the sensor coil. The pitch and yaw angles of the sensor are represented by Φ_s and Θ_s in the presence of the coil's orientation $\overrightarrow{n_s}$.

In equations 2.1 –2.5, the pose of the sensor coil is presented by the variables: X_s, Y_s, Z_s, Φ_s and Θ_s. The rest of the parameters in these equations are known from the exsisting system setups. Assuming the measured voltage induced in the sensor coil is $U_{mea,i}$. The pose of the sensor presented as:

$$F(X_s, Y_s, Z_s, \Phi s, \Theta_s) = \sum_{i=1}^{k} (U_{mea,i} - U_{est,i})^2. \tag{2.6}$$

Here, k represents the number of the transmitter coils, which should be equal or greater than 5 in order to estimate the five variables. The mathematical optimization method such as Quasi-Newton or Levenberg–Marquardt (LM) algorithm [NB04, SLPD07] is utilized to optimize the 5-DOF non-linear parameters (X_s,Y_s,Z_s,Φ_s,Θ_s). Figure 2.1 shows the estimated sensor pose described by the 5-DOF parameters.

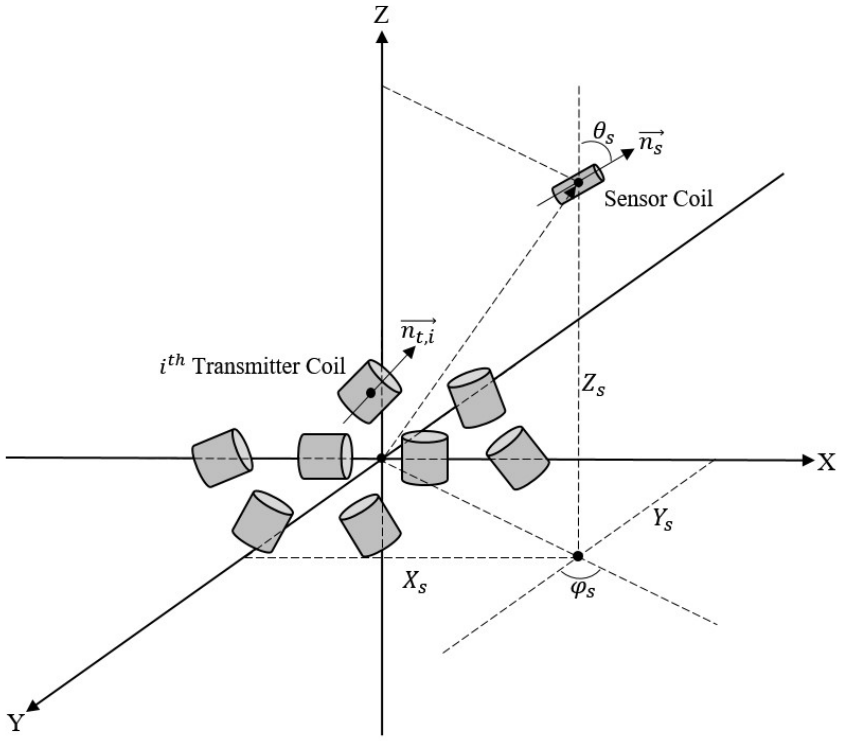

Figure 2.1: The estimated 5-DOF sensor pose. X_s,Y_s,Z_s present the estimated sensor location in 3D Cartesian coordinate systems while Φ_s and Θ_s present the yaw and pitch Euler angles. In this example, the EMTS has eight transmitter coils and one sensor coil.

The arrangement of the transmitter coils shown in Figure 2.1 is an example according to the published work [LBR13]. Different spatial placements of the transmitter coils have been proposed by research groups [OEG+14, RBSJ79, PSPK10], which will be discussed in Subsection 2.3.1. As shown in equation 2.1 and 2.3, the strength of the magnetic dipole field is related to the positions and orientations of the transmitter coils.

2.3 Extensions and the State of the Art in EM Tracking

2.3.1 EMTS Prototypes Proposed by Research Groups

Since Kuipers introduced the EMTS concept firstly in 1975 [Kui75], groups from worldwide started their research work parallel to the manufacturers. They built their own EMTS prototypes and showed simulation results on technological advantages in general tracking applications or focusing on medical applications. Some famous approaches are listed in the following.

Raab *et al.* The first and most well–known academic paper, which is cited by 683 other scientific publications, introducing a general electromagnetic tracking system was published in 1979 [RBSJ79]. In this paper, the authors proposed a basic EMTS setup with a 3-axis orthogonal magnetic transmitter and a magnetic sensor. The system scheme is shown in Figure 2.2.

The system observes the changes in sensor's position and orientation by recognizing the minor modifications in sensor output vectors, i.e. it measures the gradient of magnetic field density, which is linearly proportional to the changes of the sensor's position. Rotating orthogonal magnetic fields generated by the transmitter coils were calculated using the magnetic dipole model. In this work, the 3–axis magnetic coils were mounted together to form the magnetic sensor. The specific structure limits the size of the magnetic sensor while adds the complexity to the construction work.

The method introduced within the paper was utilized, extended and improved by other groups, for examples by [HSW+12, SHL+13b, WMH06].

Figure 2.2: System block diagram of a typical magnetic tracking system in the 20–th century. (Image modified due to [RBSJ79])

Paperno *et al.* A method based on using 2-axis orthogonal coils instead of 3 was proposed to simplify the system setup, tracking algorithm and further increase the system speed [PSL01]. In this paper, the method of continuously rotating elliptically the two orthogonal magnetic coils was proposed. Figure 2.3 shows the principles of the system setup.

In this approach, feeding the mutually orthogonal coils with phase-quadrature currents are similar to rotating the magnetic dipole in one axis, and thus simplifies the system to use only two orthogonal transmitter coils. This method has been studied, extended and further improved with proved results being evaluated by a self–built–up prototype in Shenzhen [SHL+13a].

Plotkin *et al.* Plotkin proposed to apply large 2D transmitter coil array using 64 uniaxial coils and a sensor coil for EMTS trying to increase the measured signal to noise ratio (SNR) so as to improve system

Figure 2.3: Scheme of EMTS with rotating orthogonal magnetic fields (Image modified due to [PSL01]

accuracy [PP03]. This setup was simplified by utilizing only eight planar coils [PSPK10] since it provides sufficient information for tracker pose estimation while considering the tracker accuracy. The system scheme diagram is shown in Figure 2.4.

Similar to this concept, O'Donoghue *et al.* developed low-cost EMTS for catheter tracking using standard 5-DOF technology, aiming to use clinics for catheter tracking [OEG+14, OCM15]. They used an *Arduino Due* (Ivrea, Italy) microcontroller for the data acquisition (DAQ) and the signal demodulation trying to bring down the cost down to below 900 Euro. The price are usually much higher for commercial EMTS. In their studies, the EMTS prototype with a planar field generator including eight coils on a printed circuit board (PCB) was constructed. According to their published work, although the planar PCB–based planar placement

Figure 2.4: Scheme of the EMTS with large 2D planar transmitter coils array (Image Source: [PSPK10])

of the transmitter coils are not the optimized solution, the system is sufficiently accurate in a well–defined volume of interest (VOI).

2.3.2 Commercial EMTS

Manufacturers have improved the general engineering science in EM tracking with their own features. Nowadays, for standard EMTS offered in the market which are the most popular are from Northern Digital Inc. (Canada), Polhemus Inc. (USA) and Ascension Technology Corporation (USA). The three leading manufacturers have produced several generations of products in the last decades. Table 2.1 shows the three manufacturers and their products.

These three standard EMTS are widely tested and utilized by research groups [SFD+05b, Wil06, NJBA06a, Zac97, BHKS09]. Moreover, regarding their performances in accuracy, robustness, clinical studies have also been performed using such systems for different applica-

Table 2.1: Commercial electromagnetic tracking systems of three well-known manufacturers: (a) Northern Digital, Canada [1], (b) Polhemus, Canada [2] and (c) Ascension Technology, USA [3], their models, and features.

tions [YWLC09, KXG+07, FKG+97, KWVH03]. Compatible EMTS constructed directly for use in medical applications have also existed since many years and offered on the market. Figure 2.5 shows some examples of the EMTS built for specialized clinical applications.

There are likewise other surgical systems also applying electromagnetic tracking technology. For instance, *Scopis Hybrid Navigation sys-*

[1] http://www.ndigital.com/medical/products/aurora
[2] http://polhemus.com/motion-tracking/all-trackers/fastrak
[3] http://www.ascension-tech.com/products

Figure 2.5: Examples of commercial EMTS for use in clinical applications: (a) ig4TM IR System [4] (Veran Medical, USA) for assisting biopsies and ablations for lungs, liver, and kidneys; (b) Fiagon Navigation System [5] (Fiagon, Germany) for endoscopy and microscopy; (c) Calypso [6] (Varian, USA) for real-time tumor tracking in radiation oncology.

tem [7] (Scopis Medical, Germany) fuses OPS with EMTS for anatomic targets tracking before and during operations to provide higher accuracy and robustness, depending on the clinical requirement; *Niobe* [8] (Stereotaxis, USA) was produced for remote magnetic catheter motion control and navigation in interventional medicine using two permanent magnetics. Electromagnetic tracking systems have been seamlessly integrated into the complex surgical information system *Stealthstation S7 System* [9] (Medtronic, USA) for IGS applications. The EM sensors have also been embedded into the ultrasound system *Logiq E9 system* [10] (GE Healthcare, USA) to track the US probe motion within surgical processes or for diagnose imaging.

[4] http://www.veranmedical.com/ig4.html
[5] http://www.fiagon.com
[6] https://www.varian.com/oncology/products/real-time-tracking/calypso-extracranial--tracking

In this section, only a few examples of medical-integrated systems using electromagnetic tracking techniques are given. There are likewise more related products offered on the market already, or currently under development.

2.4 The Experimental Setup

The EMTS prototype employed in this thesis being previously developed, is similar to the general concept of 5DOF tracking [PSPK10, OEG+14]. The difference are, instead of using eight planar transmitter coils, cylinder coils located at the same Z plane with distinct orientations. This advance is considered to allow the users to customize the coils' arrangement with respect to the required system accuracy, speed, and robustness.

A prototype of EMTS had already been developed by K. Will, S. Söffner, M. Grundmann and T. Bien before starting the work conducted in this dissertation. The constructed EMTS prototype consists of self-made parts: amplifier circuits and eight transmitter coils. *NDI 5–DOF sensor* (Northern Digital, Canada) was chosen to measure the voltage induced in the AC magnetic field. The prototype utilized a USB device *NI 6221* (National Instruments, USA) to generate waveform signals and acquire data. Additionally, a laptop was employed as the system computational unit to calculate the sensor pose and program the DAQ device. In this thesis, most system components remained unchanged except the

[7] http://www.scopis.com/en/products/scopis-hybrid-navigation
[8] http://www.stereotaxis.com/products/niobe
[9] http://www.medtronic.com/us-en/healthcare-professionals/products/neurological/surgical-navigation-imaging/surgical-navigation-systems/systems-software-instruments.html
[10] http://www3.gehealthcare.com/en/products/categories/ultrasound/logiq/new_logiq_e9

Figure 2.6: Schematic diagram showing the experimental setup of the ETMS' prototype, (a) eight self–developed transmitter coils placed with a randomly predefined position and orientation, (b) sensor coil, (c) eight current–feedback amplifiers for signal generation, (d) pre–amplifier for the measured signals, and (e) the system for pose estimation, signal generation and data acquisition consisting of a PC and an FPGA.

DAQ device. A more advanced system unit *NI PXI System* (National Instrument, USA) was used to improve the system refresh speed and realizing parallel executions in the tracking process. Figure 2.6 illustrats the system block diagram of the current EMTS prototype.

The FPGA within the PXI system generates the waveform signals through its digital to analog converter (DAC) and sends out the signal through the analog output (AO) terminals. The generated voltage signals were driven by eight current–feedback amplifiers *–LT1210* (Linear Technology, USA). After being amplified, they are sent to the transmitter coils to produce magnetic fields. A magnetic sensor, *NDI 5–DOF catheter* (Northern Digital, Canada) with an embedded single axis sensor coil with the diameter of $0.5mm$ and the length of $8mm$, measures the gradient of the magnetic flux density by means of the voltage in-

duced in the magnetic fields. After being increased by the pre–amplifier – *LT1167a* (Linear Technology, USA), the voltage is measured by the analog to digital converter (ADC) before sending to the FPGA inside the PXI system. After that, the FPGA sends the signals to the host PC, which is utilized to process the measured signals and estimate the sensor pose. The experimental setup was programmed by using LabVIEW (National Instrument, USA) for hardware control and MATLAB for sensor pose estimation (MathWorks, USA). Instead of a using laptop and the old version data acquisition (DAQ) board – *NI USB–6221* (National Instrument, USA) using digital signal processing (DSP) chip, an NI PXI system — *NI PXIe–1078, NI PXIe–8133 and NI PXI–7854R* was proposed with respect to realizing parallel executions and increasing the tracking speed without losing the accuracy. Figure 2.7 presents the scheme of the communications between the modules in NI PXI system.

Here, *PXIe–1078* is the system chassis which establishes data communications and synchronizes the trigger information between distinct system modules through PCI/PXI bus and PXI trigger bus. *PXIe–8133* serves as a PC with 32–bit *Windows 7* (Microsoft, USA) running on it. It controls the entire PXI system and is utilized for running the sensor pose estimation algorithm in *MATLAB*. The NI R Series module *NI PXI–7854R*, with an embedded *Virtex–5 LX110* FPGA (Xilinx, USA), is selected for analog and digital output signal generation.

The DAQ device, NI *PXI–7854R* contains eight 16–bit analog inputs with a maximum sampling rate of $750kHz$, eight 16–bit analog outputs and 96 digital I/Os. Through a bus interface, the FPGA transfers information such as data, address, and control order to other devices in the PXI system with the PCI/PXI bus. The onboard ADC and DAC enable the signal generation and data acquisition using the FPGA.

Figure 2.7: The *PXI* system (National Instrument, USA): (a) block diagram of internal system communications (b) PXI Chassis – PXIe–1078 ; (c) PXI Controller PXIe 8133; (d) PXI DAQ board consisting an FPGA, PXI 7854R.

2.5 Chapter Discussion

Although EM tracking technology has already existed over 40 years and manufacturers have provided mature products being applied in the clinical context, there are still potential improvements in the technology which will lead EMTS to be wider applied in medical settings. With respect to the tracking accuracy, robustness and working volume, Bien *et al.* have developed an EMTS prototype [BR12]. The research conducted within this thesis is based on this previously constructed system prototype. The sole alteration in the system hardware is the computa-

tion unit and the DAQ board. In order to realize parallel executions and more advanced DAQ implementations, the previous hardware needs to be modified. Therefore, an *NI PXI system* consists of a host PC, and on–board FPGA was recommended to replace the old measurement board utilized by Bien *et al.* The faster communications between the memory of the FPGA and host PC using DMA, as well as the parallel features of the FPGA enables the whole system to process much more rapidly than applying the combination of PC and an extra USB DAQ board as utilized in the previous work. Moreover, the FPGA allows a much faster moving–average–like data acquisition method, which is introduced in Chapter 4, implemented to further increase the tracking speed.

Chapter 3

Reduction of Metallic Distortions

3.1 Chapter Overview

As discussed in Chapter 2, although EMTS have achieved high acceptance in clinical settings already, the weak robustness against metallic distortions in OR environment is still a remaining issue which prevents its wider applications [OCM15, BWW+98, SFD+05a]. This chapter introduces a novel approach to reduce the tracking errors caused by metallic objects, which are positioned in proximity to the magnetic sensor coil. The proposed method is a purely software–based solution which could seamlessly be integrated into other setups of AC EMTS with no changes in the system hardware. This approach has a potential to improve the safety and outcome when applying EMTS to assist IGS.

3.2 Classifications of Metallic Distortions

The metallic objects which are positioned in proximity to the sensor coil cause tracking errors for EMTS. For example, surgical instruments, metallic arm support and electronic devices such as ultrasound probe [WBW+99, BRF+15, BWW+98, PA02] can cause significant tracking errors. The sources of metal distortions can be classified into ferromagnetic

and electrically conductive distortions. In order to analyze the influences from the different sources of distorters, the magnetic flux density through the material should be discussed. Considering the magnetization, the magnetic flux density across the material is given by [KCB+03]:

$$B = \mu_0(1 + \chi)H = B_0 + \mu_0\chi H. \tag{3.1}$$

In this equation, B represents the magnetic flux density in the material, and B_0 represents the reference magnetic flux density outside. μ_0 is the vacuum's magnetic permeability, H is the magnetic field strength and χ is the magnetic susceptibility [KCB+03]. For the paramagnetic and diamagnetic materials, the magnetic susceptibility χ is linear while for ferromagnetic materials, it is non-linear. Due to the magnetic hysteresis effects [GCJ88], it is difficult to analytically characterize the secondary magnetic field generated by the ferromagnetic object. Commonly used surgical instruments, such as hammers, trocars, and needles, are usually made of non–ferromagnetic materials such as aluminum and non–ferromagnetic stainless steel. For the distortions resulting from electrically conductive objects, the eddy current induced in the material generates secondary magnetic fields appending to the reference magnetic fields, which are generated by the transmitter coils. This chapter focuses on introducing a method for reducing distortions caused by materials which are electrically conductive but non–ferromagnetic.

3.3 Related Work

In minimizing the tracking errors caused by metallic objects in the OR, different groups have proposed their solutions trying to overcome this problem. In this section, the methods listed in the literature are surveyed.

3.3.1 Increasing Source Distance

The level of sensor pose errors is substantially affected by the size, type, proximity and the shape of the metallic objects. As a straightforward solution to avoid metallic distortions, Poulin *et al.* suggested that placing the source of distortions at a maximum distance to the EM sensor will allow the EMTS to minimize the tracking errors [PA02]. Measurements have been conducted by using different surgical instruments, devices, and OR tables as sources of distortions and placing them with the various distances to the sensor of EMTS.

The results illustrate that the estimated sensor pose errors caused by most sources of distortions in OR can be reduced to an ultra-low level when there is a larger than $30cm$ distance between the sensor and the distorter [PA02]. This concept has been further studied by Faustin *et al.*, and they concluded that a $10cm$ between the sensor and the metallic distorter is sufficient to reduce the sensor pose error to a a very level which is negligible for clinical applications [SCK+10]. However, such operations cannot always be achievable in the well-established clinical workflows. For some specific applications, such as dental surgeries [EST+04b], the distance of the metallic objects cannot be increased far enough from the EM sensor. On the other hand, the sources of distortions for EMTS in OR are not always recognizable by the medical doctors during the interventional procedures. Therefore, this proposed method is only the perfect solution, when the distorters are well understood and not necessary to be located in proximity to the EM sensor during the interventional procedures.

3.3.2 Calibration Technology

Research groups proposed their calibration methods to minimize the sensor position and orientation errors caused by the metallic or electronic surroundings and other uncertainties of EMTS. The first concept

of EMTS tracker calibration to correct sensor pose errors was referred by Raab [RBSJ79]. A strict precondition is that the transmitter's position should remain unchanged to the surrounding metallic objects, and therefore the calibrations can only correct the sensor pose errors caused by stationary metallic distorters.

The commonly applied calibration methods are classified by analytical and numerical solutions [IBHH01]. For the analytical solution, the distortion is assumed as a polynomial function of the sensor position. By fitting the polynomial to the collected data, the computed coefficient of the polynomial is utilized to correct the distorted sensor positions [Kin99]. For the numerical solutions, instead of using an analytical polynomial model, a uniformly spaced lookup table (LUT), which contains information about actual and distorted tracker locations, can be employed. For these calibration methods, external tracking systems are needed to provide multiple reference locations of the EM sensor. Typically, calibration phantoms with fixed structures or more accurate tracking systems, such as optical tracking system, are utilized as the external reference positioning system for performing such calibrations. Tracker calibration technology has been proved to significantly reduce the tracking errors caused by the approximate metallic object. However, it only reduces the pose errors resulting from the static source of distortions.

A novel method of dynamically performing distortion detection and calibration was proposed by Sadjadi *et al.* [SHZF16]. The concept of this work is to locate multiple EM sensors with a fixed distances to each other. Additionally, an optical marker is also attached with fixed distances between the EM sensors.

In this approach, the extra EM sensor is utilized to detect the changes of the magnetic field due to the sources of distortions in proximity. The measured distances between the EM sensors change when the field is distorted. The pose of the optical marker measured by an OTS is used as a reference to correct the distortions simultaneously during the tracking

Figure 3.1: The design of the tool to fix the EM sensors and optical marker for dynamic distortion detection and correction (Image Source:[SHZF16]).

process. This study provides a concept for dynamically correcting the EM tracking error by an OTS. However, this approach still has its limitations due to its relatively large and fixed structure. The line–of–sight requirement is an additional issue, could still exist in pose rectification process. This approach could potentially fit some specific applications, such as tracking of an ultrasound probe. It does not support applications which require small–size sensor and non–line–of–sight requirements, such as the flexible catheter tracking inside of the patient's body.

A concept to simplify the calibration procedures, which does not require external reference positioning systems, was proposed by Plotkin *et al.* [PKHP08]. As figure 3.2 shows, a sensor housing support which is utilized to fix the distance between the sensor coil's locations. By moving the sensor linearly along the housing support to collect multiple data sets of changes in the sensor distance, the calibration can be performed. In this approach, multiple measurements are still required which prevents the correction of tracking errors being performed in real time.

3.3.3 Magnetic Shielding

Commercial EMTS commonly employ a table–top or planar field generator which can be placed below the patient during interventional proce-

Figure 3.2: The housing structure for tracker calibration of EMTS (Image Source: [PKHP08]).

dures [FHB+14]. Most operating tables are made of a distinct grade of stainless steel which adds eddy current and ferromagnetic distortions to the generated magnetic field [NJvJ08]. Manufacturers have integrated the magnetic shield in their field generator to protect the generated EM field from the distortions below the patient [FHB+14]. Since the designs of shielding for commercial systems are confidential of the manufacturers, O'Donoghue *et al.* built the shielding panels and evaluated the shielding performances based on their self-developed EMTS prototype. It was reported in their published work that mu–metal and ferrite provide excellent shielding performances to the magnetic distorters below their field generator [OCM15].

Similar to the basic shielding scheme, side shielding method to metallic distorters was claimed in the patent [JSKS03]. If the adjacent metallic distorters are well noticed, side-shielding to the sources of distorters could also significantly reduce the distortions to the reference magnetic field caused by the metal object. Still, the limitation of this method is obvious, only when the distortion sources are recognized, the shielding can be applied. For individual metal objects, the special design of the shielding board is required. In practice, when there are multiple metallic

Figure 3.3: Planar shielding scheme for electromagnetic tracking system (Image Source: [OCM15]).

distorters in the proximity with the more complicated spatial arrangement in OR, performing special shielding could be difficult. Moreover, the additional multiple shielding panels could potentially influence the well–established clinical workflows.

Another shielding method of designing and constructing additional shielded coils was put forward in the patent [Dum01]. The aim of this invention was utilizing an extra coil to generate an "image" magnetic field which can compensate the secondary magnetic field produced by the eddy current flowing within the electrically conductive material. For this method, although there is no extra shielding panels need to be built, the parameter optimization of the coil design is highly dependent on the level of the distortions. For larger distortions, larger coil size and more turns of windings, are needed to provide better shielding performance. This invention was solely originated in the patent, no further evaluations of this method have been found in the literature.

Manufacturers have produced shielded sensors, e.g. , *Aurora Shielded and Isolated 5DOF sensor* (Norther Digital, Canada) but within another concept. No magnetic shielding but the electrical shielding is being considered. It isolates the external electrical fields to the sensors to reduce the electrical interference.

3.3.4 Paused DC Tracking

Aside from AC EMTS which commonly utilize up to $14kHz$ operation frequencies, DC EMTS, also called paused DC EMTS, were invented aiming to minimize the conductive distortions caused by the eddy current flow inside of the proximate metal objects [PC08a]. For AC-driven EMTS, the eddy currents induced in the electrically conductive materials generate secondary magnetic fields which are adapted to the reference fields produced by transmitter coils. The adaptive AC magnetic field due to the eddy current has the same frequency of the magnetic field generated by the transmitter coils. The idea of the DC-driven EMTS is to supply the transmitter coils with pulsed DC signals. This concept permits the current flow decay to approximately zero to minimize the eddy-current distortions caused by commonly utilized conductive materials in clinics, such as stainless steel (300 series) and aluminum. DC EMTS cannot reduce the tracking errors caused by materials consisting of ferromagnetic materials with high magnetic permeability [Kin00]. To achieve this, large–size flux–gate magnetic sensors need to be applied to increase the accuracy in measuring system steady–state response to the pulsed DC waveform excitations. The compensation of the earth magnetic field distortion is also necessary to be done for the pulsed DC EMTS. Compared to AC EMTS, the disadvantages of pulsed DC EMTS for use in ISG are obvious: much slower refresh rate. The pulsed DC EMTS is not applicable for the real–time guidance. The sensor with much large size cannot be mounted into catheters or needles for surgical applications. It likewise has a higher production cost.

3.3.5 Ultra–low Frequency Input Signals

The AC input signals for EMTS are usually at Kilohertz range [OCM15]. A method using ultra–low frequency signals as system excitations was invented by Anderson *et al.* [And10]. The AC density drops on the metal

surface are related to the thickness of the metal and the skin depth which is given as [WB10]:

$$J = J_S e^{-(1+j)\frac{d}{\delta}}. \tag{3.2}$$

where δ is the skin depth, J_S is the AC current density at the surface of the conductor and d is the actual depth from the surface. The imaginary part illustrates the phase decay of current density. As is seen in equation 3.2, with larger skin depth, the AC current density in the conductor decreases exponentially. The formula of calculating skin depth is given by [Joh63]:

$$\delta = \sqrt{\frac{2\rho}{\omega\mu}}. \tag{3.3}$$

Here, ρ is the conductor's resistivity, ω is the signal's angular frequency of the input AC signal. μ is the permeability of the conductor and calculated as follows:

$$\mu = \mu_r \mu_0 \tag{3.4}$$

In equation 3.4, μ_r is the relative magnetic permeability of the conductive material and μ_0 is the vacuum's magnetic permeability. As shown in equations 3.2 –3.4, the skin depth of the conductor depends on the material and the frequency of the current flow within the conductor, which is equal to the frequency of the external AC magnetic field generated by transmitter coils. The skin depth of the conductive material becomes larger when the frequency is lower. Grounded on this theory, Anderson proposed the method of using ultra–low frequency, such as $25Hz$ excitation signals, to generate a magnetic field in order to decrease the AC current density on the surface of the proximate conductor.

This method looks very promising in reducing the tracking errors dynamically. However, there are two main drawbacks. The first is its slow

refresh rate in measuring the voltage induced in the sensor coil. Compared to a $1kHz$ input signal, for measuring one period of the voltages induced in the sensor coil, with a $25Hz$ signal, the measurement is 40 times slower. Using an ultra–low frequency signal as system excitation will significantly reduce the speed in voltage measurement and thus will negatively influence the rate of sensor pose estimation. Secondly, the magnitude of the voltage induced by the generated magnetic field is related the signal frequency. According to equation 2.5, the amplitude of the induced voltage across the sensor coil is proportional to the signal frequency. With an ultra–low frequency input signal, the measured voltage is much smaller compared to applying higher frequency signals, e.g. $1kHz$, as system excitations. Therefore, a much lower SNR could result in the measured voltages, which will add significant jitter errors to the estimated sensor pose.

3.3.6 Quadratic–Rectangular Excitation Based Method

For correcting the errors caused by conductive materials, a potential method was studied and proposed by Bien *et al.* in 2013 [BLSR14, BLR13]. For AC EMTS, the commonly employed excitation signals are sinusoidal waveforms [PSL01]. By measuring the voltages induced in the sensor coil, although there is a tiny difference in detected signal phase with and without nearby conductive distortion, it is not enough to distinguish between distorted and undisturbed voltage signals. Instead of using a standard sine wave as excitation signal [LBR13, PSL01, SE01, And07, KNTO11], a method using quadratic–rectangular excitation was developed by the group previously [BLSR14]. The principle of this approach is to supply the transmitter coils with a quadratic–rectangular waveform signal.

The measured system response to a quadratic excitation consists of the voltage induced by the transmitter coil and the conductive distorter

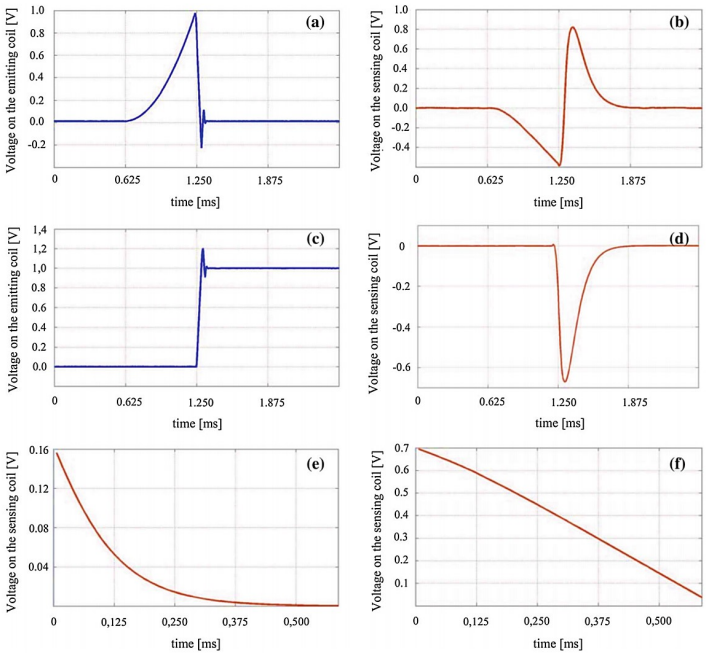

Figure 3.4: System steady–state response to the quadratic and rectangular excitations measured by the ADC of the DAQ board *NI USB-6281* (National Instrument, USA): (a) quadratic excitation measured by ADC, (b) system response on the sensor coil measured by ADC, (c) rectangular excitation measured by ADC, (d) system response on the sensor coil measured by ADC, (e) second integration of the system response to the rectangular excitation, (f) the value of the system response to the quadratic excitation minus the second integration of the system response to the unit rectangular excitation (Image source: [BLSR14])

.

in the presence of a ramp part and an exponential component. On the other hand, the system response to a rectangular excitation consists of only the exponential component. The principle of this method is shown in Figure 3.4.

The voltage in Figure 3.4(f) consists only the information of the voltage induced by the generated magnetic field. It leads the mutual inductance estimation between the transmitter and the sensor coil in order to optimize non–distorted sensor's pose from the source of conductive

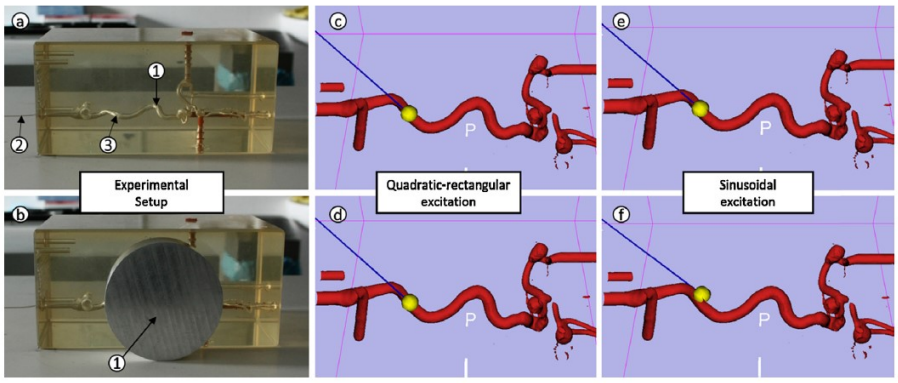

Figure 3.5: The experiment of the tracking visualization without and with nearby aluminum disk: subfigures (a) and (b) indicate the system environments –without and with a neighboring conductive distorter. In (a), (1) is the artificial vessel, (2) is the catheter inserted into the phantom, (3) indicates the position of the catheter's tip. In (b), (1) illustrates the aluminum disk placed closed to the sensing coil. (c) and (d) show the tracked poses (described by the yellow point and blue line) by using QR excitation. (e) and (f) show the results using sinusoidal excitation (image source: [LBR14])

distortions. The first evaluation of this method was performed offline [BLSR14]. Afterward, this approach was implemented into the *PXI System* to speed up the refresh rate for estimation of sensors poses. The dynamic evaluation was performed to assess the tracking performance of quadratic-rectangular excitation method [LBR14].

The results demonstrate that the method reduces the tracking errors caused by a mobile aluminum disk located in proximity to the sensor coil, to an acceptable low level. However, the system response to the rectangular excitation needs to be measured at its steady state, as a result, the system still has a low refresh rate in estimating the sensor pose. More specifically, each complete measurement of the steady-state system response to the quadratic–rectangular excitations for eight channels, takes $(0.625 + 30)ms \times 8 = 245ms$. Due to the noisy signals in the voltage measurement, a moving averaging of at least a 5 peri-

ods are needed. Therefore, considering the computational processes also consumes time, the experimental setup with this method being implemented has a system latency greater than $245ms \times 5 = 1225ms$. Due to the slow measurement speed, this method is not suitalbe for real–time applications.

3.4 The Ramp Excitation

3.4.1 Equivalent Circuit

As is suggested in the literature [Sch01, NK08], a conductive distorter positioned in proximity to the EM sensor can be modeled as an additional resistance–inductance (RL) circuit. For general AC EMTS, the frequency of the system excitation signals is commonly in kilohertz range [OCM15], which is much lower than the self–resonant frequencies of the wires and coils. Therefore, the capacitive effects in analyzing the inductive coupling among the transmitter, sensor and conductive distorters are insignificant. Based on the equivalent circuits built by Bien *et al.* [BLSR14], a more specific circuit scheme has been redrawn for a better understanding of the implementations. Figure 3.6 shows the equivalent circuit model of inductive couplings among the transmitter and sensor coil with a proximate conductor.

In Figure 3.6, the voltage signal U_g is the voltage generated by the waveform generator. This signal is then increased by a current–feedback amplifier with a gain of A_T. After that, the voltage across the transmitter coils has been increased to $U_T = A_T U_g$. The resistance of the transmitter coil's circuit is R_T and the inductance of the transmitter coil is L_T. The resistances R_S,R_D and inductance L_S,L_D represent the parameters of the circuit of the sensor coil and an external conductor respectively. Because of the inductive coupling effect, there is a voltage drop U_S across the sensor coil circuit. This voltage is increased

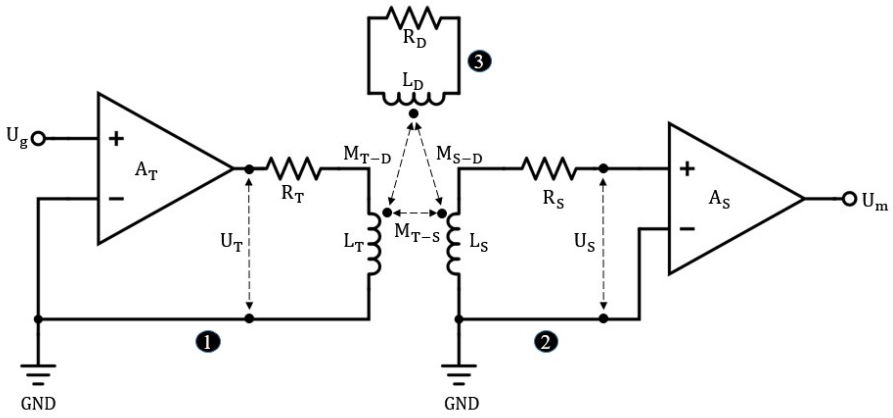

Figure 3.6: The RL circuit model of (1) one transmitter coil circuit, (2) the sensor coil circuit and (3) the equivalent circuit model of a conductive distorter (Image Source: [LHR17]).

by an operational amplifier with a defined gain of A_S. After that, the voltage signal $U_m = A_S U_S$ is measured by the *PXI* system. The mutual inductances of the transmitter/sensor coil, transmitter/distorter and sensor/distorter are represented by M_{T-S}, M_{T-D} and M_{S-D}.

3.4.2 System Analysis with Ramp Excitation

The voltage U_m measured by the ADC of the DAQ device comprises voltages induced by the magnetic fields produced by the transmitter coil and the conductive distorter. This work aims to separate the voltages induced by the transmitter coil from voltage induced by the proximate conductive objects.

The time constant is important in analyzing the circuit characteristics of the transmitter coil and conductive distorter circuit. The calculation is given by the equations [Haj10]:

$$\tau_T = \frac{L_T}{R_T}, \tag{3.5}$$

$$\tau_D = \frac{L_D}{R_D}. \tag{3.6}$$

The system was analyzed in the Laplace domain to simplify the calculation processes [Lei12]. The transfer function of the inductive coupling between the sensor and transmitter coil is given by [Doe74]:

$$G_{T-S} = \frac{U_S}{U_T} = \frac{sM_{T-S}}{L_T(\frac{1}{\tau_T} + s)}. \tag{3.7}$$

The generated ramp signal $U_g = K \cdot t$ was utilized as the system input excitation signal. The calculation of the voltage induced in the sensor coil in Laplace domain is given by:

$$U_{S-T}(s) = \frac{KM_{T-S}}{L_T \cdot s(s + \frac{1}{\tau_T})}, \tag{3.8}$$

and in the time domain as:

$$U_{S-T}(t) = \frac{KM_{T-S}\tau_1(1 - e^{-\frac{t}{\tau_T}})}{L_T}. \tag{3.9}$$

Herein, the system response to a ramp excitation consists of two components: a DC component and an exponential curve –due to the switch–on cycle. The Laplace transfer functions of the inductive couplings between L_T and L_D, L_D and L_S are given as:

$$G_{T-D} = \frac{sM_{T-D}}{L_T(s + \frac{1}{\tau_T})}, \tag{3.10}$$

$$G_{D-S} = \frac{sM_{S-D}}{L_D(s + \frac{1}{\tau_D})}. \tag{3.11}$$

The calculation of the voltage induced in sensor coil in the Laplace domain is given by:

$$U_{S-D}(s) = \frac{KM_{T-D}M_{S-D}}{L_T L_D \cdot (s + \frac{1}{\tau_T})(s + \frac{1}{\tau_D})}, \tag{3.12}$$

and in the time domain as:

$$U_{S-D}(t) = \frac{KM_{T-D}M_{S-D}\tau_T\tau_D(-e^{-\frac{t}{\tau_D}} + e^{-\frac{t}{\tau_T}})}{L_T L_D(\tau_T - \tau_D)}. \tag{3.13}$$

When there are conductive distorters in the proximity of the magnetic sensor coil, the measured signal contains both the non–distorted and distorted voltage. Equations 3.12 and 3.13 show the voltage across the sensor coil due to a neighboring conductive distorter. As seen in the equation, the measured signal comprises a DC component and three exponential components. This voltage comprises distorted and non–distorted information is explained as:

$$U_s(t) = \frac{KM_{T-S}\tau_1(1 - e^{-\frac{t}{\tau_T}})}{L_T} + \frac{KM_{T-D}M_{S-D}\tau_T\tau_D(-e^{-\frac{t}{\tau_D}} + e^{-\frac{t}{\tau_T}})}{L_T L_D(\tau_T - \tau_D)}. \tag{3.14}$$

The aim is to separate the voltage induced by the transmitter coil $U_{S-T}(t)$ from the interfering signals of $U_{S-D}(t)$ induced by the metallic conductor in the time domain. Based on the ramp waveform excitation, this separation can be achieved. As seen in equation 3.14, the clean voltage, i.e. not considering the conductive distortions which are in proximity to the sensor, comprises a DC component $\frac{KM_{T-S}\tau_1}{L_T}$ and an exponential component $-\frac{KM_{T-S}\tau_1(e^{-\frac{1}{\tau_T}})}{L_T}$, while the induced voltage caused by the conductive distorter only containing two exponential paths without a linear curve. The larger the time variable t is, the more the exponential components of $e^{-\frac{t}{\tau_T}}$ and $-e^{-\frac{t}{\tau_D}}$ are decaying to 0. If the time variable t equals to positive infinity, the measured voltage as is given by equation 3.9 becomes a constant signal comprising only the information of the non–distorted voltage signal. However, in reality, t must not be any too large value because of two reasons: first, the measurement speed would be too slow; second, with a lower signal frequency, the induced voltage would be smaller causing a lower SNR in voltage measurement. To en-

sure the high quality of measured signals and an adequate measurement speed, choosing a suitable signal period t with the fixed maximum supply voltage is important for the ramp excitation method.

3.4.3 Simulation

In the established experimental setup, the following parameters were measured and approximated to be: $L_T = 1.2mH$, $R_T = 15\Omega$, $\tau_T = \frac{L_T}{R_T} = 0.08ms$. The frequently applied metal materials for use in medical applications are aluminum, austenitic stainless steel, titanium and brass [YR10, Nar09, Nii03]. Among them, aluminum was selected for this simulation process because of its much higher conductivity which results in larger current flow within the metal. At the room temperature of $20C^o$ the resistivity of aluminum is $2.65 \cdot 10^{-8}\Omega \cdot m$. The resistance of the metallic cylinder –ρ,l,A representing the resistivity, length and cross-sectional area is computed as:

$$R_D = \rho\frac{l}{A}. \tag{3.15}$$

Here, the conductive distorter is assumed as a regular shape cylinder with a length of 100 mm and a diameter of $10mm$ for simple approximation. The resistance of such a modeled distorter was calculated to be $3.4 \times 10^{-5}\Omega$. With the same shape, materials with lower resistivity have a smaller time constant according to equation 3.6 and 3.15.

The calculation of the self–inductance of a cylinder–shape conductor is given as [Ros08]:

$$L_D = [ln(\frac{2l}{r} - \frac{3}{4})]nH. \tag{3.16}$$

In equation 3.16, the parameter r is the radius of the cylindrical conductor. The time constant of the conductor in this example was calculated to be $1.8ms$. The self-inductance of the defined aluminum distorter

is calculated to be $5.8 \times 10^{-8} H$. The self-inductance of the sensor coil L_S can be calculated is given by [Nav05]:

$$L_S = \frac{\mu N^2 A}{l}. \tag{3.17}$$

In the experimental setup, the *NDI 5-DOF Catheter* (Northern Digital, Canada) was utilized as the sensor coil. The turns of windings N is not given by the manufacturer; it is assumed to be 1500 for this simulation. According to the manufacture's specifications, the length and the diameter of the sensor coils are $11mm$ and $0.8mm$ respectively. The self-inductance of the sensor coil is calculated to be $4.1 \times 10^{-5} H$.

The mutual inductance between the transmitter, sensor, and conductive distorter are calculated using equations 3.18 –3.20.

$$M_{T-S} = k_{T-S} \cdot \sqrt{L_T L_S}, \tag{3.18}$$

$$M_{T-D} = k_{T-D} \cdot \sqrt{L_T L_D}, \tag{3.19}$$

$$M_{S-D} = k_{S-D} \cdot \sqrt{L_S L_D}. \tag{3.20}$$

where, k_{T-S}, k_{T-D} and k_{S-D} are the coupling coefficients between air coils which are typically smaller than 0.35 [Mea02]. When the distance between the coils increases, the coupling coefficient decreases. The change in the coupling coefficient solely changes the amplitude of the voltage signals. It has no influence on the time constant of the distorter. It is assumed that the air coil coupling is equal to 0.1 for this simulation. The eddy–current distortion could be either additive or subtractive due to the positive/negative current flow directions within the conductor, relative to the current flow directions within the sensor coil.

As Figure 3.7 shows, the red curves represent the voltage induced in the sensor coil which contains the information of the reference voltage signal induced by the transmitter coil (blue dash line) and the distorted

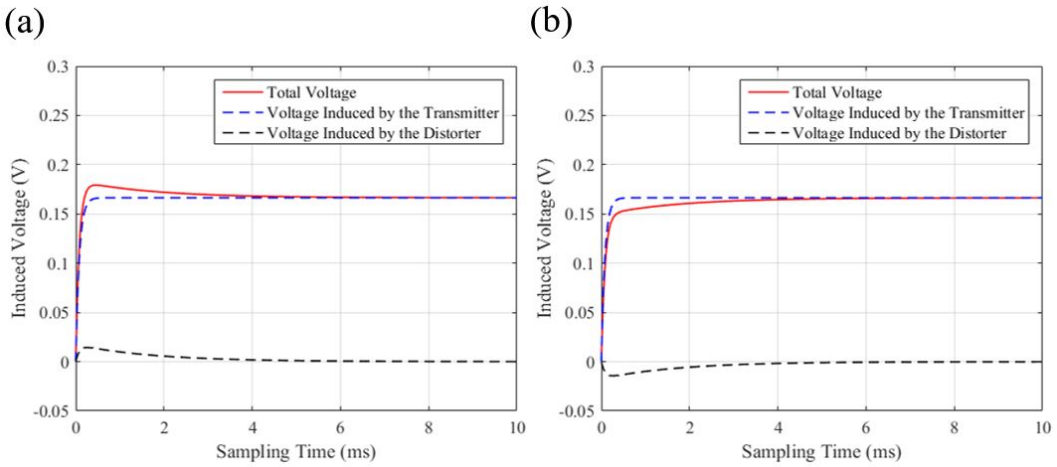

Figure 3.7: An example of voltage measurement simulation. (a) Additive distortion, (b) subtractive distortion.

signal caused by a conductive object (black dash line). In the real world, only the total voltage can be measured. Due to the switch–on cycle effect, a $5 \times \tau_T = 0.4$ ms delay was added for the system response reaching its steady state. The "Total voltage" between $9.5ms$ and $10ms$ is approximately equal to the non–interfered voltage. The percentage differences between the "corrected" voltage and the voltage induced by the transmitter coil is calculated to be 0.04% given below:

$$\%\triangle U = |\frac{U_{T-S} - U_{Corrected}}{U_{T-S}}| \times 100. \tag{3.21}$$

The most important parameter in the ramp excitation method is the time constant of the distortion materials. Additional simulations by changing other parameters have also been performed. It is assumed that the conductive distorter is placed extremely in proximity to the sensor coil by adjusting the coupling coefficient k_{S-D} to 0.35. Figure 3.8 shows the simulated result.

From the result presented in Figure 3.8 it can be seen that, the distortions can be reduced to a very low level for the given scenario. The

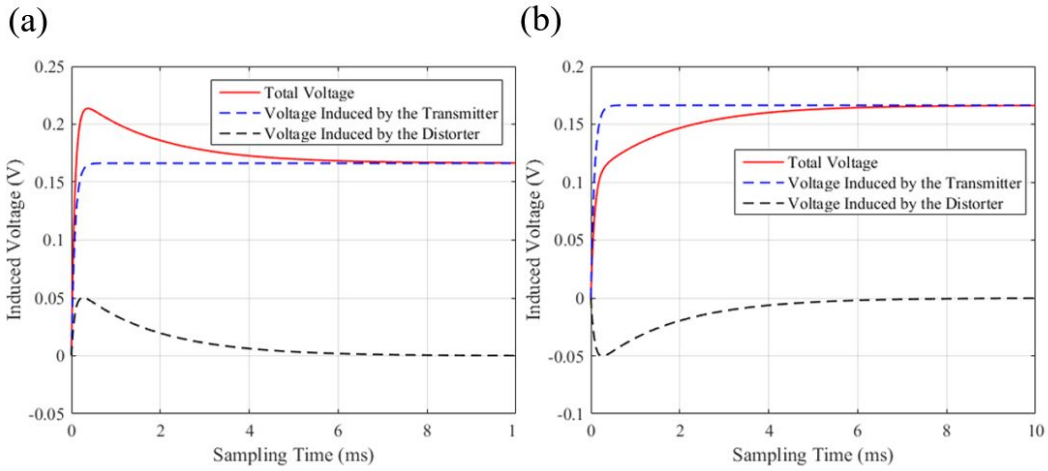

Figure 3.8: Voltage measurement simulation – increasing the coupling coefficient $k_{S-D} = 0.35$. (a) Additive distortion, (b) subtractive distortion.

difference between the "corrected" voltage and the voltage induced by the transmitter is calculated to be 0.14% in this scenario.

3.4.4 Time Constant Measurement

Besides the mutual inductance between the conductive distorter and the sensor coil, another important parameter which influences the result is the time constant of the transmitter coils and distorter see equation 3.14. The time constant τ_T is a fixed value while τ_D is a variable due to the distorters' material, size and, shapes. A measurement to get the actual value of the time constant of distinct metallic objects is performed is shown in Figure 3.9.

In this experiment, the sensor coil was located on a LEGO tower on top of the field generator box. The metallic objects were placed approximately $0.5cm$ in proximity to the sensor coil. A unit step function was generated and supplied to the first of the eight transmitter coils. The system response to its steady state to the unit step excitation was measured and is utilized to calculate the time constant of the three metallic

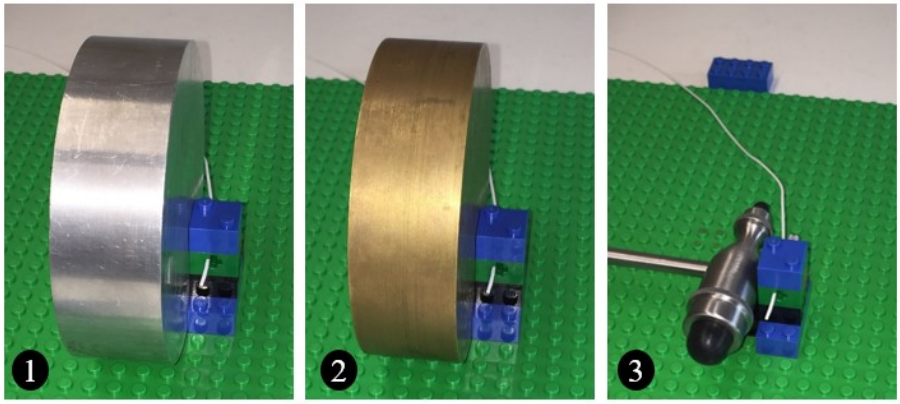

Figure 3.9: The measurement of the time constant: (1) an aluminum disk with a diameter of 10 and thickness of 3cm and (2) a brass disk with a diameter of 10cm and thickness of 3cm, and (3) a neurological reflex hammer.

distorters. The measurement result is presented in Figure 3.10.

The voltage induced in the magnetic sensor was measured and shown in Figure 3.10. The measured voltages in the time domain between 2.58ms and 3.2ms mainly consist of the information about the system switch–on cycle, the time constant of the transmitter coils and the conductive distorters. The measured voltages in the time interval between 3 ms and 15 ms solely shows the voltage decaying in the conductive distorters. The time constant is able to be estimated by the time interval between the maximum and 63.2% of the maximum value in the measured voltage signals [RA11]. The time constant of the aluminum and brass disk, and the reflex hammer, were estimated to be 1.72, 0.98 and 0.75ms separately. As Figure 3.10 shows, the time constant varies due to different materials. Herein, the aluminum disk had the biggest time constant. Therefore, the system needed at least approximately $1.72ms \times 5 + 0.62ms = 9.22ms$ to reach its steady state. For the nearby brass disk and reflex hammer, the system needs 5.52ms and 4.37ms to reach its steady state respectively.

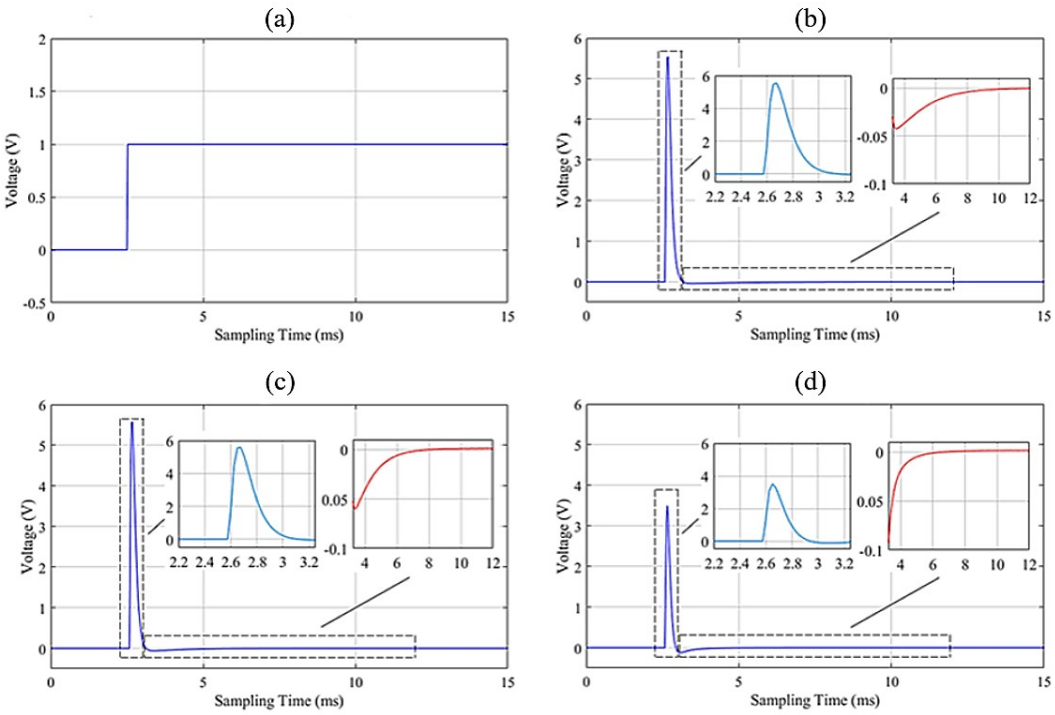

Figure 3.10: The measured voltage to a unit step excitation for distinct conductive distortions: (a) the unit step excitation, (b) the system response to an aluminum disk, (c) the system response to a brass disk, and (d) the system response to a neurological reflex hammer.

3.5 System Implementation

The developed method was implemented in the *NI PXI System* (National Instrument, USA). As is mentioned in the literature, EMTS commonly applies the time division multiplexing (TDM) and frequency division multiplexing (FDM) technology to separate the voltage measurement in each channel [Gov02, RBSJ79, WB06b]. FDM method bases on separating the 8–channel signals using band-pass filters. However, the measured voltages are analyzed in the time domain where the steady-state system response is not filtered out. Therefore, the FDM does not support the ramp-excitation method. The TDM technology separates the 8–channel

signals in the time domain which supports the proposed method. However, for low-frequency input signals, the tracking refresh rate is very low. In this section, a moving-average-like data acquisition method is introduced aiming to increase the tracking refresh rate for the TDM-based method. The detailed implementation steps of these methods and signal generation and data acquisition loop will be introduced in Chapter 4.

3.6 Experiment and Evaluations

3.6.1 Measurement of Refresh Rate

Although the system has a maximum refresh rate of $20Hz$ in voltage measurement – see Section 3.4.3, the computational processes consume additional time. Therefore, a dynamic test of the system refresh rate in updating sensor pose signals was performed here. In this evaluation, the refresh rate of using the ramp, QR, and sinusoidal excitation was evaluated individually. For dynamically assessing the tracking refresh rate, a measurement setup is illustrated in Figure 3.11 was used.

As illustrated, the catheter was previously inserted in the vascular phantom at position (2). A pullback device was applied to pull out the catheter with a speed of $0.5mm/s$ over 100 seconds. The complete updates of the sensor's pose were counted to calculate the system update in each second.

3.6.2 Measurement of Tracking Latency

The tracking latency is another concept apart from the refresh rate. In electromagnetic tracking, the tracking latency indicates an actual delay of measuring one complete update of a sensor pose. Figure 3.12 shows the setup to measure the tracking latency.

In this evaluation, the sensor coil was fixed at nine different positions based on using LEGO frames. The LEGO board was fixed on top of the

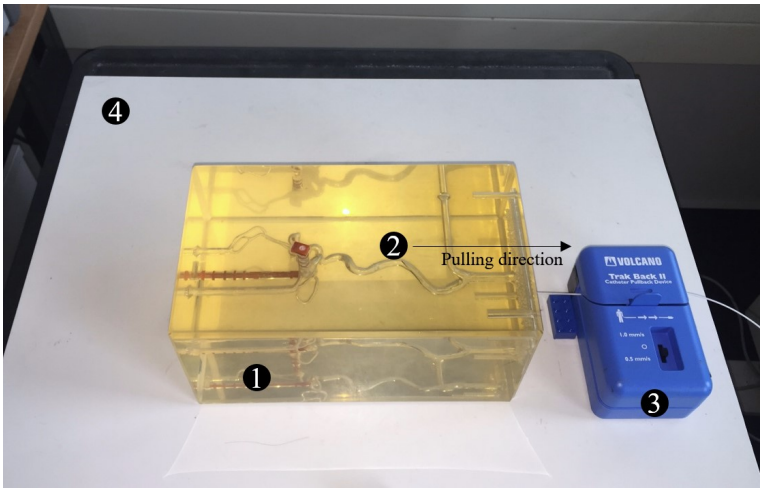

Figure 3.11: The measurement of the system refresh rate: (1) the vascular phantom, (2) the location of the catheter's tip, (3) catheter pullback device Trak Back II (Volcano, Japan) and (4) field generator box.

field generator box. For each position, the actual latency between starting voltage measurement and estimating the sensor's pose was measured by clearing the signals stored in the buffer after each measurement. In dynamic tracking processes, the initial guess in the LM algorithm is updated based on the values of last sensor pose estimation. For the latency measurement, the initial guess of the 5-DOF sensor's pose was fixed to remain unchanged.

3.6.3 Measurement of Tracking Precision

The static accuracy assessment of the static tracker was performed by means of an optical tracking system –*Polaris Spectra* (Northern Digital, Canada). The optical tracking system was utilized to provide the sensor reference positions.

In this measurement, the sensor was automatically moved by the robot in the test volume along X, Y, Z directions automatically. Together, 512 poses were measured by the EMTS and OTS respectively. The positions

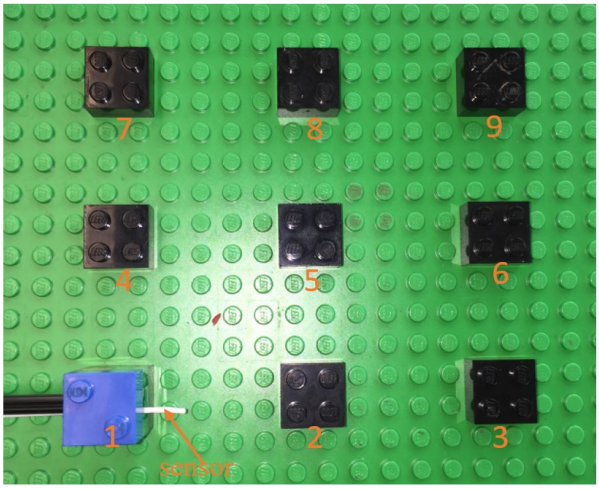

Figure 3.12: The setup of the system latency measurement.

measured by the optical tracking system was utilized as a reference to calculate the EMTS sensor error as is given by equation 3.22 and 3.23 [HSW+12].

$$E_{p,i} = \sqrt{(X_{m,i} - X_{r,i})^2 + (Y_{m,i} - Y_{r,i})^2 + (Z_{m,i} - Z_{r,i})^2}, \tag{3.22}$$

$$E_{o,i} = |\Phi_{m,i} - \Phi_{r,i}| + |\Theta_{m,i} - \Theta_{r,i}|. \tag{3.23}$$

where, j represents the $i-th$ poses and E presents the pose error of the EM sensor at individual locations. X_m, Y_m, Z_m, Φ_m and Θ_m are the marker pose measured by OTS used as the reference positions. X_r, Y_r, Z_r, Φ_r and Θ_r are the measured sensor pose by EMTS. The mean error (ME) and root-mean-square error (RMSE) were calculated as:

$$ME = \frac{1}{n}\sum_{j=1}^{n} E(i), \tag{3.24}$$

$$RMSE = \sqrt{\frac{\sum_{j=1}^{n} E(i)^2}{n}}. \tag{3.25}$$

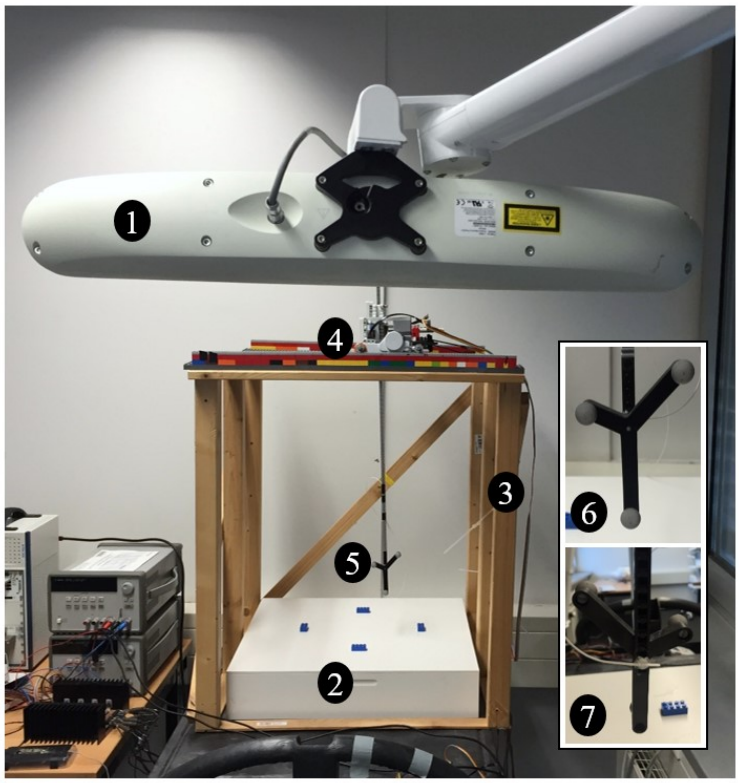

Figure 3.13: The tracking accuracy evaluation protocol using OTS: (1) the optical tracking system, (2) the field generator plane, (3) the test volume, (4) LEGO robot being used to move the tracker, (5) optical marker and EM sensor with fixed locations: (6) front view for optical markers, (7) back view for the rigidly fixed sensor coil.

Because of the mechanical limitation of established LEGO frame, the sensor coil was faced towards one direction for all the measurements. Therefore, the precision of the sensor's orientation was not comprehensively evaluated with this setup.

3.6.4 Test of Free–hand Mobile Distortion

The tracking errors due to the mobile distorter is the primary problem for EMTS in surgical applications which needs to be solved. In this test,

Figure 3.14: The measurement of dynamic distortions to electromagnetic tracking systems, based on an empirical free-hand movement of the metallic disk: (1) sensor coil on top of the field generator of the commercial EMTS, (2) sensor coil on top of the experimental setup field generator, (3) and (4) the aluminum disk with the diameter of 5 cm and the height of 3 cm, was utilized as the distorter being moved towards and away from the sensor coil based on a free-hand movement with an approximately constant speed.

a simple comparison between a commercially available system – *NDI Aurora* (Northern Digital, Canada) and the ramp waveform excitation method was performed. In this measurement, the same sensor coil –*NDI 5 DOF catheter* was fixed on top of the field generator surfaces of the Aurora system and the experimental setup. The test setup is presented in Figure 3.14.

It was an empirical measurement, which relied on a free hand motion of the conductive distorter. The metal disk was moved towards and backward to the sensor coil with the distances periodically changing from approximately $10cm$ to $1cm$. The experiments aimed to compare the developed ramp waveform excitation method with a commercial system to evaluate the ability of the method to reduce the distortions caused by conductive objects. The position of the sensor coil was measured 1800 times for each scenario. The sensor positions measurement by both of

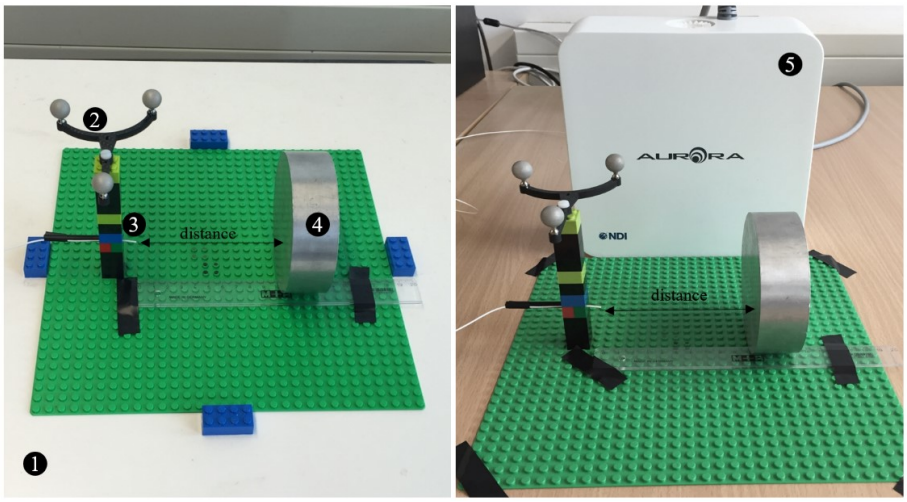

Figure 3.15: The measurement of sensor pose error caused by a proximate conductor at different distance between 10 cm and 1 cm away from the sensor coil: (1) the field generator of the prototype, (2) the optical marker with fixed pose to the sensor coil, (3) the sensor coil, (4) the conductive distorter, and (5) the field generator of NDI Aurora (Northern Digital, Canada).

the systems were compared.

3.6.5 Test of Distance-dependant Distortions

To estimate the sensor pose error related to the changes in the distance between the sensor coils and the conductive distorters, the measurement as illustrated in Figure 3.15 was performed.

In this measurement, aluminum/ brass disks, and a reflex hammer were tested as the conductive distortions. The metallic objects were moved from $10cm$ away and towards the sensor coil, till a distance of $1cm$. In this measurement, an additional optical tracking system was used as the reference to provide the ground truth of the sensor's positions. The changes in sensor's poses caused by the conductive distorters were measured by EMTS, caused by the sources of distortions placed at various distances to the surface of the field generator, have been mea-

sured. The results were compared with the prototype system applying sinusoidal and ramp excitations, and also on a commercial ETMS – *NDI Aurora*. To minimize the noise effects on the tracked sensor's poses, each measurement had been repeated 1000 times for averaging.

3.6.6 Measurement of Distortions from Different Sources

The system performance against the distortions coming from a brass disk of different size, multiple clinical instruments was tested in this experiment. Figure 3.16 indicates the sources of metallic distortions for EMTS. In this experiment, the distorters were all fixed $1cm$ away from the sensor coil on the experimental setup and also the commercial EMTS.

Figure 3.16: Sources of distortions: (1) a $5 \times 1cm$ brass disk, (2)a dental drill body, (3)a Langenbeck hook, (4)a bone curettes (5) a scalpel, (6) needle holder and (7)an ultrasound probe. In this measurement, the different sources of distortions were put between the sensor and field generator for both the commercial system and the experimental setup. A test phantom was utilized to fix the catheter location. The distance between the sensor coil and the distorter was fixed to $1cm$.

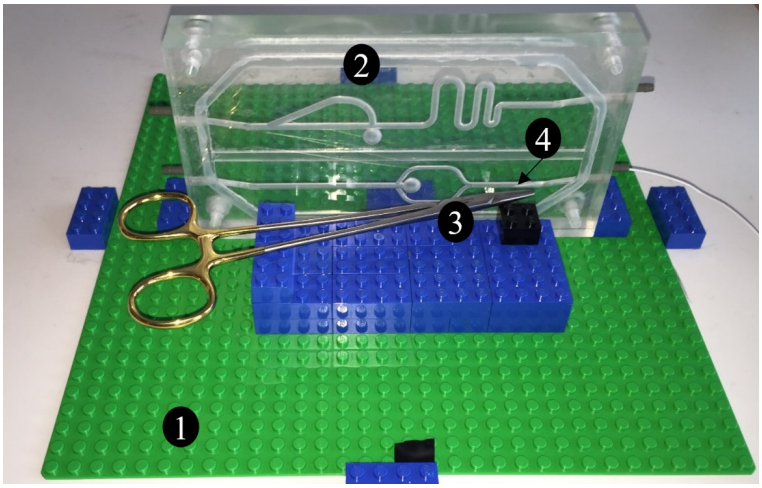

Figure 3.17: Measurement of distortions caused by surgical instrument: (1) non-metallic LEGO board, (2) the test phantom, (3) surgical instrument (a needle holder) and (4) fixed sensor coil position inside of the phantom.

The tracking errors due to the distorters were measured by the standard commercial system and the EMTS prototype using ramp excitation method. Figure 3.17 shows the fixed positions between the sensor coil and the sources of distortions using a phantom made of Plexiglas.

3.7 Results

Refresh rate

The system's refresh rate was measured to be $12.7Hz$. Table 3.1 presents the compared results among the different methods running on the experimental setup.

Table 3.1: The measured tracking refresh rate of the different method in the experimental setup.

Method	Sine–TDM	Sine–FDM	QR–TDM	Ramp–Fast TDM
Refresh rate(Hz)	6.3	34.4	1.5	12.7

Table 3.2: EM tracker position error in the test volume with the distance between sensor and center of transmitter coils up to 200mm with 20 up to 1000 times averaging in voltage measurement.

Distance	200mm				100mm			
Averaging Times	20	200	500	1000	20	200	500	1000
Mean (mm)	5.7	5.1	4.0	3.4	2.0	1.4	1.0	0.8
RMS (mm)	8.0	7.4	5.8	5.0	2.2	1.6	1.2	1.0
Max (mm)	38.8	34.2	24.3	23.4	5.7	4.2	4.0	3.9
95th Percentile (mm)	16.4	17.1	13.1	11.0	3.6	2.8	2.6	1.8

Latency

The latency of these sensor's 9 locations as shown in Figure 3.12 were measured to be 426, 435, 422, 425, 426, 433, 434, 442 and 436ms. The averaged latency is calculated to be $431 \pm 6.5ms$.

Tracking Accuracy

For the ramp excitation method, the measured voltages induced in the sensor coil consist of high–level noise signals. In the measured total 512 sensor poses, the maximum distance between the sensor and the center of the transmitter coils was 200 mm. Table 3.2 shows the results of the sensor positional error due to distinct averaging times in voltage measurement with distinct distances between sensor and transmitter coils.

Due to the higher noise level in the voltage measurement, the sensor positioning accuracy of the ramp excitation method was lower than using sinus excitation with the same experimental setup. The sensor positioning accuracy is influenced by two parameters: the averaging times and the distance between the sensor and the transmitters. With the current setup, when the distance between the sensor and the center of the transmitter coils is less than 100 mm with the 1000 averaging times, the sensor RMS positioning error was 1.0mm which was comparable to commercial EMTS [BHWC08].

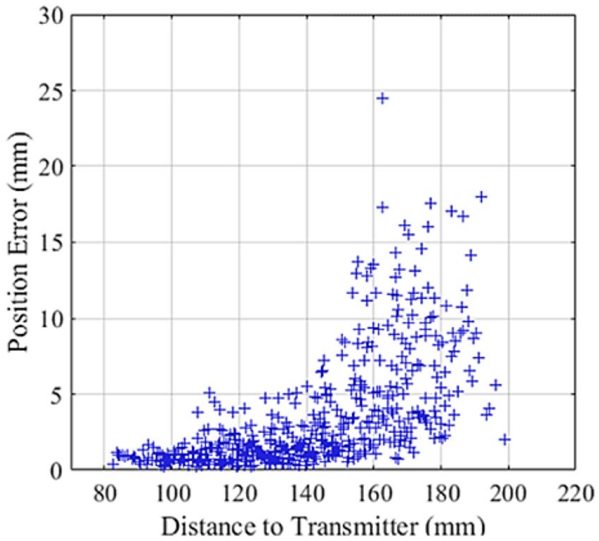

Figure 3.18: Sensor positional error in the measurement volume with the distance between the sensor coil and the center of the transmitter coils up to $200mm$ – 1000 times averaging.

The error distributions are corresponding to the distinct distances between the sensor and the transmitter coils, with 1000 times averaging, is presented in Figure 3.18.

Mobile Distortion

The reduction of the distortions caused by a mobile aluminum disk of the ramp waveform excitation method is compared with a commercial EMTS, based on a free–hand movement. The results are presented in Figure 3.19.

The commercial EMTS had a better performance with a low std. Error if there was no aluminum disk in proximity to the sensor coil. However, when there was a mobile aluminum disk close to the sensor coil, the prototype with ramp excitation method has better result in this scenario. The root mean square error of the sensor positions for the 1800 samples

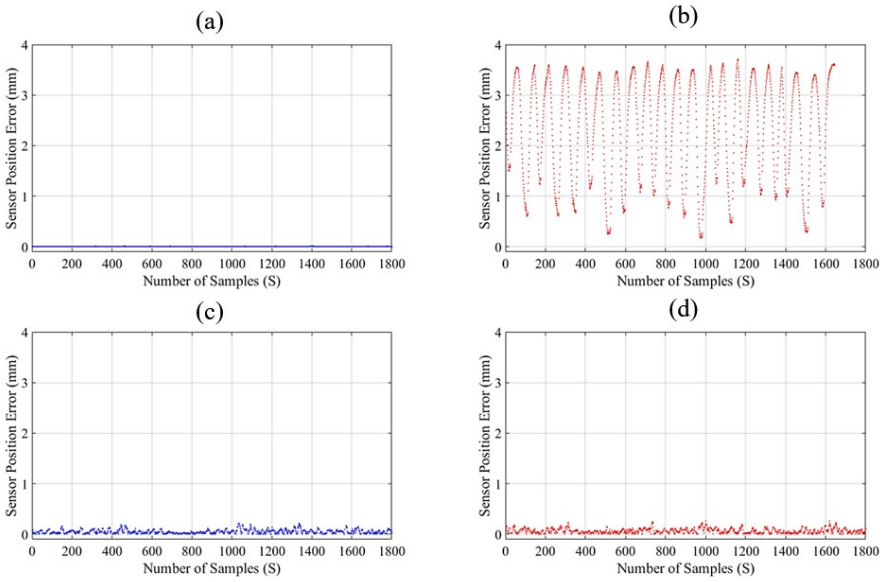

Figure 3.19: The dynamic distortion comparison between Aurora and the ramp excitation method running on the experimental setup: (a) sensor position error of the Aurora system without distortion; (b) the sensor position error of the Aurora system having 154 missing measurements with dynamic distortion; (c) the sensor position of the ramp waveform excitation method without distortion; (d) the sensor position error of the ramp waveform excitation method having no missing measurement with dynamic distortion.

was $5 \times 10^{-3} mm$. The RMS and the max error of the ramp waveform excitation method in sensor position were calculated to be $0.07mm$ and $0.24mm$ without nearby dynamic conductive distortions. However, when there was a portable conductive distorter moving around the sensor coil, the measured sensor's position was disturbed for the Aurora system. In 1800 samples there were 156 missing measurements (system errors) when the aluminum disk was too close, i.e. approximately $1cm$ away, to the sensor coil. The RMSE of the rest of the measured sensor position is $2.54mm$, and the max error is $3.71mm$. The ramp waveform excitation method works better in this scenario with the RMSE and the max error of the measured sensor position of $0.08mm$ and $0.26mm$ respectively,

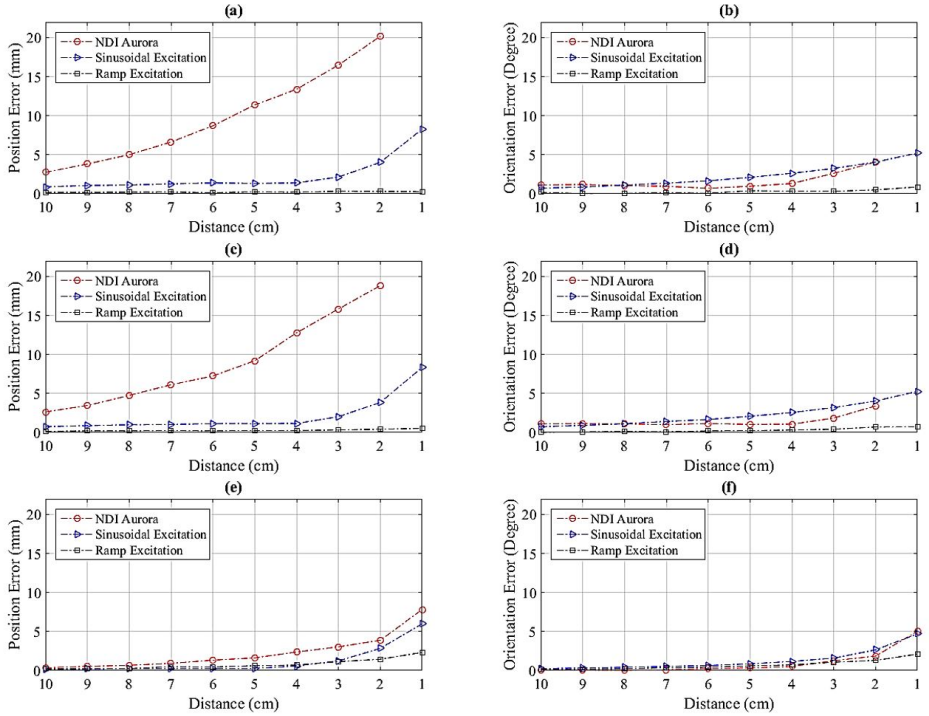

Figure 3.20: Tracking error caused by sources of distortions:(a) position and (b) orientation error due to an aluminum disk and (b), (c) position and (d) orientation error caused by a brass disk, (e) position and (f) orientation error due to a reflex hammer.

with no missing measurement.

Distance-dependent Distortion

The measurement, as shown in Figure 3.20, was aimed to analyze the level of errors in estimated sensor's pose caused by the distinct distances between the sensor and transmitter.

The errors increased when the distances between the sensor and the distorter decreased, for the commercial system and the experimental setup applying sine–wave excitation. Missing measurements occurred by using the NDI Aurora system when the aluminum disk and the brass disk were placed $1cm$ away from the sensor coil. The proposed method

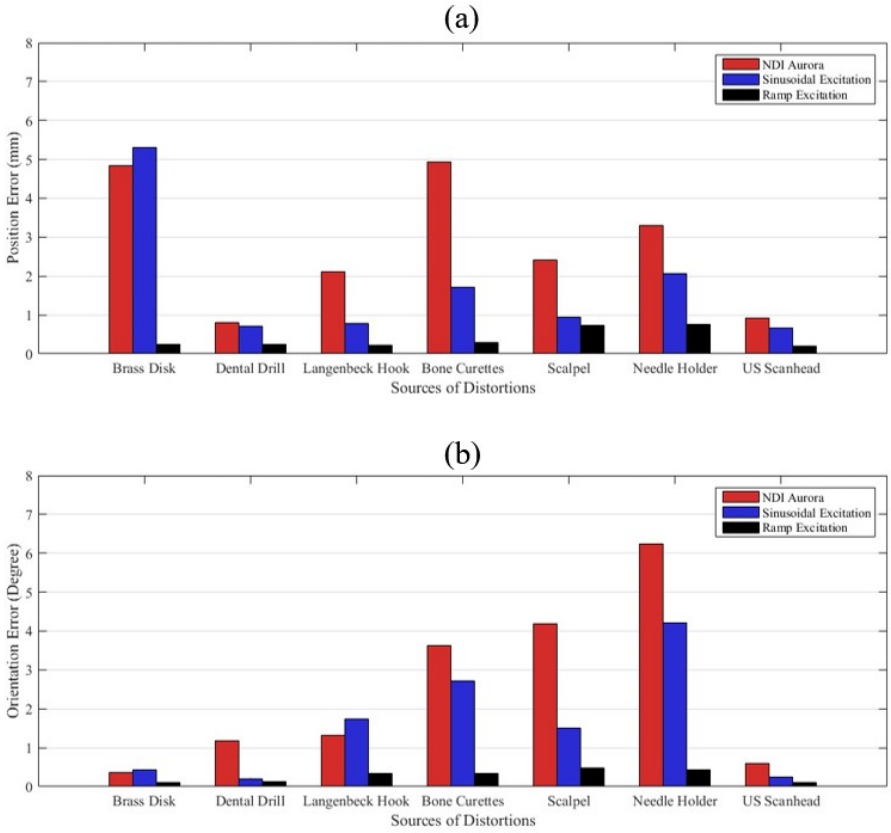

Figure 3.21: Sensor pose's error resulting from different sources of distortion for the experimental setup applying ramp/ sinusoidal excitations, and the NDI Aurora EMTS (a) position error, (b) orientation error.

reduces the errors due to aluminum and brass disks at distances to be smaller than $0.5mm$ and 0.8^o. However, the errors caused by the reflex hammer cannot be reduced to such a low level.

Distortions from Different Sources

As is illustrated in Figure 3.21, the sensor pose error for both the commercial system and the EMTS prototype was presented using sinusoidal and ramp excitation caused by distinct instruments.

The commercial ETMS and the experimental setup using sinusoidal excitation have similar performances due to a distorter being placed $1cm$ away from the sensor coil. The biggest sensor pose errors for the commercial ETMS and sinusoidal excitation are $4.93mm$ and $5.30mm$ from the estimated position and 6.23^o and 4.22^o in orientation. The experimental setup applying ramp excitation reduces sensor pose error caused by the different distorters with the maximum pose error of $0.75mm$ and 0.48^o.

3.8 Chapter Discussion

Given the fast TDM method, and its implementation based on an FPGA, the system features a refresh rate of $12.7Hz$. FDM using sine–wave excitation is much more rapidly than the proposed ramp excitation method. However, the proposed method cannot apply FDM because the system response is not able to be filtered out in the time domain. In the work introduced in this chapter, five periods of the measured voltage signals were averaged to increase the signal quality. For a complete process of the sensor's pose estimation, the system needs $50ms \times 8 = 400ms$ to measure the voltages induced in all of the eight channels. The computational processes also consume time. Therefore, the current approach has a delay of approximately $431ms$ to estimate the sensor's pose completely.

Regarding the tracking accuracy, the expected error was less than $2mm$. The current approach meets this requirement when the distance between the sensor and the center of the transmitter coils is smaller than $150mm$. The pose error is greater when the distance increases, because of a poorer SNR of the measured system response to the ramp excitation. In the current established EMTS prototype, the spatial arrangement of the transmitter coils' position and orientation were randomly predefined in a single plane. Optimization of the spatial arrangement of the transmitter coils can be performed to let higher magnetic flux through the

cross–sectional area of the magnetic sensor so as to measure larger voltage drops. It will lead to a better SNR in the measured voltage induced in the sensor coil, allowing the system to obtain a higher precision in the sensor's pose estimation. The hardware of the system can be optimized to further increase the SNR. Applications of using sophisticated filters such as the Kalman filter, which have the potential to improve the robustness as well as speeding up the frame rate, can be investigated. These improvements may enhance the accuracy and robustness of the ramp excitation method for EMTS in a much larger working volume.

A comparison with a commercial system with the sensor coils placed in the presence of proximate conductive distorters was performed. The commercial EMTS and the prototype applying sinusoidal excitation demonstrated significant errors due to a proximate conductive distorter. The system applying ramp excitations reduced such errors to a very low level. The proposed method reduces the pose errors caused by pure non-ferromagnetic materials, such as aluminum and brass disks, to a significantly low level. However, there was still a clear error when certain medical instruments made of stainless steel, such as a reflex hammer and a needle holder, were located close to the sensor coil. Although austenitic stainless steel is non–ferromagnetic, other types of stainless steels such as ferritic, martensitic and duplex are ferromagnetic. The proposed ramp excitation method reduced the errors caused by conductive but non–ferromagnetic materials.

The current approach on the EMTS prototype is slower in updating sensor's pose signals compared to the commercial EMTS, which generally has refresh rates between 40 – $250Hz$ [NJBA06b]. The latency of the Ascension Flock of Birds and the Polhemus Fastrack system was measured to be approximately up to $50ms$ [BE96], which is much lower than the approach in removing conductive distortions. Wrt. spatial position accuracy, NDI's Aurora system was reported to have a position RMS error of $1.2mm$, having the distance between the sensor and field trans-

mitter up to $600mm$. The evaluation was performed by using an optical tracking based accuracy assessment protocol [FWLK03]. The accuracy of the current approach is $1.6mm$ RMS error within a distance of up to $150mm$. The main advantage is the improved robustness against proximate conductive distorters. In fact, as illustrated in Figure 3.20 and Figure 3.21, the ramp excitation based method provides a significantly better robustness against distorters than the commercial system.

3.9 Future Work

This chapter introduces a software–based solution to reduce tracking errors caused by electrically conductive objects in operating rooms. Before letting it be put forward into the use of real clinical applications, the system needs to be further improved and comprehensively evaluated. In this thesis, the tracking accuracy was assessed utilizing an optical tracking system as the reference positioning system. As documented by the manufacturer, the *NDI Polaris Spectra* has a $0.25mm$ RMS error. Based on the error distributions of this system as was reported in [WTF04], the testing volume was carefully selected. However, the positions measured by such optical tracking system still do not provide the ground truth with sufficient precision. The results being shown in Figure 3.13 and Table 3.2 indicate the error distributions and the potential for use in clinical applications. In the future, more accurate optical tracking systems such as the *Atracsys fusionTrack 500* or laser–based tracking systems such as the *FARO* Laser Tracking System, which has a much higher accuracy, have to be applied as reference positioning systems. With respect to statistically assessing the orientation accuracy, test phantoms having tiny error tolerances and setups permitting the changing of the sensor's orientations have to be applied [HFB+06]. The current approach of this method being implemented in the EMTS prototye has a mean delay of $431ms$ in updating the sensor's pose. To further reduce the system la-

tency in the future, one solution is an adaptive truncation of the ramp signal periods. The measurement time of $10ms$ for each excitation was chosen. It allows the distortions caused by conductive materials, whose conductivity are smaller than aluminum, to be removed. As the future work, an adaptive process for choosing the optimal time with respect to different levels of distortions will be investigated. From low to high level of conductive distortions, the system should automatically choose the most suitable periods of the ramp input signals. A weak point of the basic prototype is the hardware, which has not been optimized with regarding the electronic noise, the amplifier of the test coil, or the transmitter coils' arrangement. These aspects have to be further improved in the future, to let the system be more precise. Furthermore, sophisticated filters such as Kalman filter will be applied in order to shorten the averaging periods and increase the tracking accuracy. It should also be noticed that all the calculations are done with *MATLAB*, causing avoidable delays. Last but not least, this ramp–waveform based implementation focus on reducing metallic distortions. However, when there is no metal object which is located in proximity to the sensor coil, the standard method using sine–wave excitation allows the system to operate more accurately in a larger volume of interest and with much faster measurement speed. Therefore, a more intelligent solution could be the adaptive switching between sinusoidal and ramp excitation methods for EMTS, after detecting if there is a proximate conductive distorter.

3.10 Chapter Conclusion

This chapter represents a proof of the concepts for a method based on ramp waveform excitation, which diminishes the tracking errors caused by the proximate metallic conductors to a significantly low level. This purely software–based procedure currently provides a low refresh rate of $12.7Hz$ and a relatively small VOI for precise tracking. Nevertheless,

since the reasons for these issues are well understood, the implementation can be straightforwardly improved.

Chapter 4

System Implementation

4.1 Chapter Overview

As briefly introduced in Chapter 2, in this dissertation the FPGA within the *PXIe-7854R* (National Instrument, USA) device was utilized to generate waveform signals and acquire data. In this chapter, the hardware implementation in and the communications between the FPGA and host PC are introduced.

4.2 Signal Generation and Data Acquisition

As mentioned in Chapter 3, there are three DAQ methods applied in this thesis: TDM, FDM are the standard methods; The more advanced moving-average-like TDM method was developed in this thesis to increase the tracking speed for the ramp–excitation-based method. In this section, the system flows and implementations in the NI PXI system are introduced.

4.2.1 Time Division Multiplexing

The TDM method is also known as the process of sequential signal generation and data acquisition. Figure 4.1 shows the workflow of the TDM

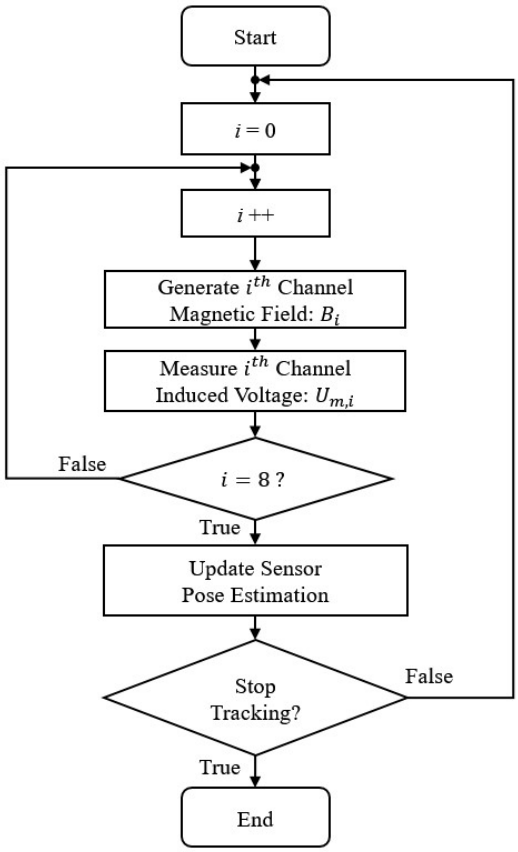

Figure 4.1: The flow chart of the TDM method in EM tracking adapting the developed prototype.

method adapting for the 8–channel EMTS prototype. For the TDM method, after starting the program, the system sequentially activates each of the eight transmitter coils to generate the magnetic field. Once the eight–channel signals have been acquired, the system begins to estimate the sensor's pose.

As a standard DAQ method in EM tracking, TDM clearly separates the sensor pose estimation from each update of 8–channel voltage measurement. Considering the synchronization of the signal generation process, eight sequential digital triggers were utilized. At the rising edge of

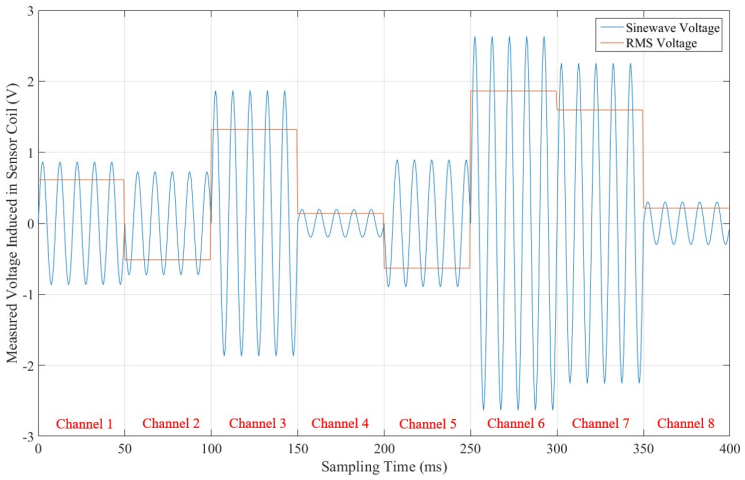

Figure 4.2: An example of voltage measurement using TDM method with the excitation signal frequency at 100 Hz for eight channels.

the each digital triggers, the corresponding channel is started to generate analog output signals while the data acquisition process is activated. As shown in Figure 4.1, the generated signals are sequentially sent to the transmitter coils to generate magnetic fields.

The sequential structure of the system flow isolates the eight–channel magnetic fields in the time domain. When one channel is activated, the other channels are paused. For this reason, the tracking speed is highly dependent on the update rate of the voltage measurement.

Figure 4.2 shows a case in voltage measurement in the magnetic fields generated by positive sine–wave current signals. The root–mean–square (RMS) value in the voltage measurement is employed here for smoothing the measurement result and defining the positive or negative voltage drop across the sensor coil. In this example, the excitation signal is selected to be $100Hz$, for each channel, five periods are repeated. For a complete measurement of eight channels, $\frac{1}{100Hz} \times 5 \times 8 \times 1000 = 400ms$ is needed.

The advantages of the TDM method are simple implementation and clear isolation of signals in distinct channels in the time domain. It al-

lows sine–wave excitation as well as ramp excitation based method to be applied. For sine–wave based excitations, the input signal frequencies are usually higher than $1kHz$ [OCM15] which leads the system to have an acceptable tracking speed. However, for ultra-low-frequency input signals [And10], quadratic–rectangular excitation based [BLSR14] and the proposed ramp excitation method as was introduced in Chapter 3, traditional TDM method does not support them for real-time applications.

Typically, the system needs to measure and average several periods of voltages induced by the AC magnetic fields to achieve better signal to noise ratio (SNR) , thus improves the tracking accuracy. As discussed in Section 3.4, the period for each generated ramp waveform is selected to be $10ms$. By repeating the measurement of each channel five times for averaging, a complete measurement of eight channels requires at least $400ms$. Considering the time consumed by the computational processes, the system cannot reach a refresh rate which is faster than $2.5Hz$ applying the basic TDM method. Shortening the signal periods being recorded may increase the system refresh rate, whereas it could reduce the tracking accuracy. Therefore, in order to speed up the proposed ramp–excitation based approach, new method in system flow needs to be developed.

4.2.2 Frequency Division Multiplexing

The principle of the FDM method is to generate the multi–channel signals in parallel. In the meantime, the voltage signals induced in the sensor coil consisting of multi–channel information are measured. It can significantly increase the system refresh rate based on its parallel executions.

As Figure 4.3 illustrates, for the FDM method being adjusted for the prototype, the generated signals with distinct frequencies were passed through the current–feedbackamplifiers into eight transmitter coils to

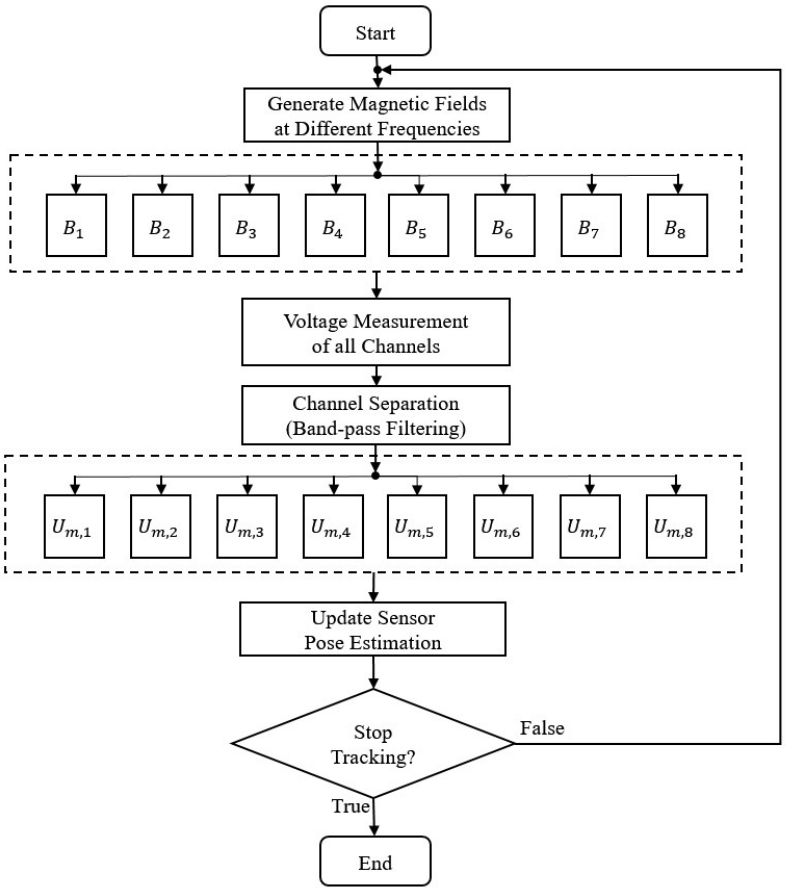

Figure 4.3: Flow chart of the FDM method in EM tracking adapting the prototype.

generate eight channels of magnetic fields in parallel. Eight infinite impulse response (IIR) third order band–pass filters (BPF) were implemented in the FPGA for fully parallel separations of signals at different frequencies. Within this approach, the FDM method increases the speed of DAQ processes to increase the refresh rate in sensor pose estimation. In this approach, eight parallel BPFs were implemented into the FPGA to separate the multi–frequency signals [LBR13]. Alternatively, fast Fourier transform (FFT) based method [OEG+14] can be employed to separate the voltages in different channels with distinct frequencies. Figure 4.4

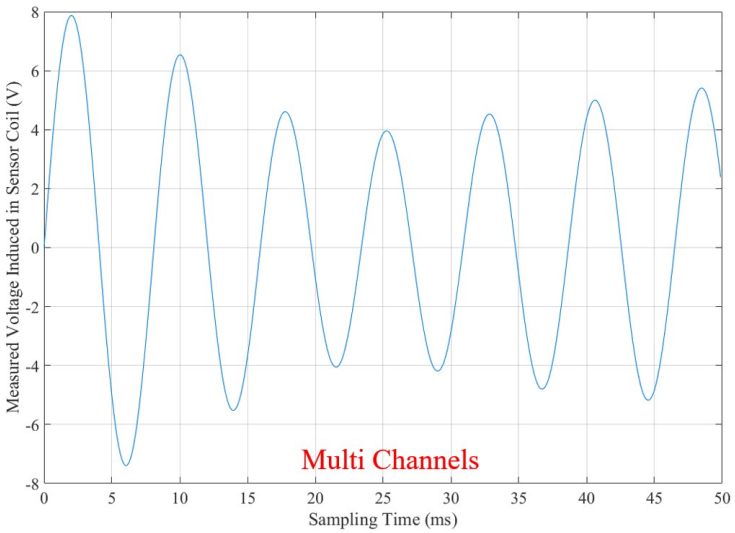

Figure 4.4: An example of voltage measurement using FDM method with the excitation signals at distinct frequencies between $100Hz$ and $135Hz$ with each increasing step of $5Hz$ for eight channels.

shows an example of the voltage measurement with the eight–channel EMTS using FDM.

As discussed above, the measured voltages consist of the sum of the eight channel's voltage signals at distinct frequencies. The separated signals using band–pass filtering are presented in Figure 4.5.

Here, the lowest frequency of the eight–channel signals is $100Hz$. Herein, the FDM method reduces the measurement time from $400ms$ down to $50ms$ and therefore, ideally it increases the maximum refresh rate in sensor pose estimation from $2.5Hz$ up to $20Hz$.

In order to adapt the established experimental setup, the generated signals in eight channels were sent through the amplifiers to the eight transmitter coils to create magnetic fields. Each transmitter coil was supplied with sine–wave voltage signals at distinct frequencies between $1650Hz$ and $2000Hz$, with a step width of $50Hz$. Eight third–order fixed–point band–pass filters with $20Hz$ band width, were designed us-

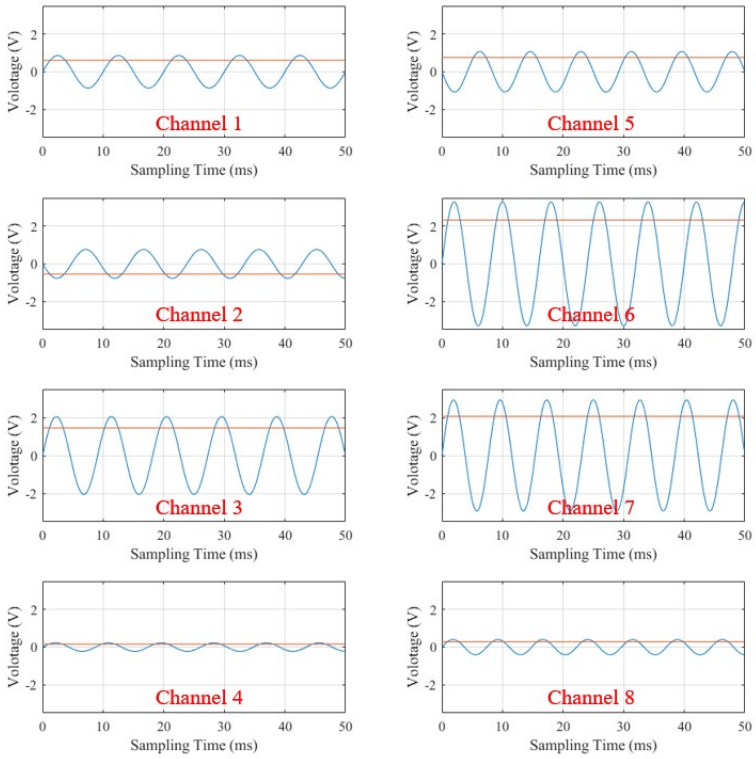

Figure 4.5: Separated eight–channel voltage signals for FDM ranging from 100 Hz to 135 Hz.

ing *LabVIEW Filter Design Toolkit* (National Instrument, USA) and implemented in the FPGA to realize parallel filtering processes. The system setup applying the FDM method was evaluated to have a positional accuracy of $1.6mm$ in a $25.6 \times 25.6 \times 18cm^3$ working volume, which is similar by applying TDM method –$1.5mm$ RMSE, and a refresh rate up to $35Hz$ which is approximately 5.8 times faster than TDM [LHR15]. The increased tracking referesh rate is sufficient for real-time applications.

For sine–wave-excitation based EM tracking, the FDM method increases the tracking speed dramatically when compared to the traditional TDM method. However, the FDM method is not applicable to all sig-

nals types. The seperation process of the signals at different frequencies applies either band–pass filtering or FFT which processes the signals in the frequency domain. The QR excitation [BLSR14]and ramp excitation methods developed to reduce eddy–currentrent distortions in sensor pose estimation, introduced in Chapter 3, which needs to measure the system response to the particular system excitations in the time domain, are not supported by the FDM method. Within the ramp–excitation method, the system's steady–state response needs to be measured and analyzed in the time domain, which cannot be filtered out in the frequency domain.

4.2.3 The Improved TDM

Supporting the methods based on measuring the system steady state responses in the time domain, while making the real-time application possible, the traditional TDM method was improved to a moving–average–like TDM method. In this approach, the data acquisition and sensor pose estimation processes are separated into two parallel loops which are treated separately.

As shown in Figure 4.6, although the system still generates and sends signals to the transmitter coils to produce magnetic fields sequentially similar to the standard TDM method, the sensor pose estimation loop is running in parallel. Compared to the conventional TDM, this proposed method increases the system refresh rate in sensor pose estimation by the factor of 8. Apart from the traditional the TDM method, which only utilizes one FPGA FIFO to acquire 8–channel signals for one update in voltage measurement, the moving–average like TDM method is supported by implementing eight FPGA FIFOs. Each FIFO starts to acquire data at the rising edge of the eight digital triggers of all the channels and send data through DMA to the memory of the host PC. Because eight channels of signals are isolated by using different trigger signals, eight FIFOs were needed here. Instead of updating one complete voltage

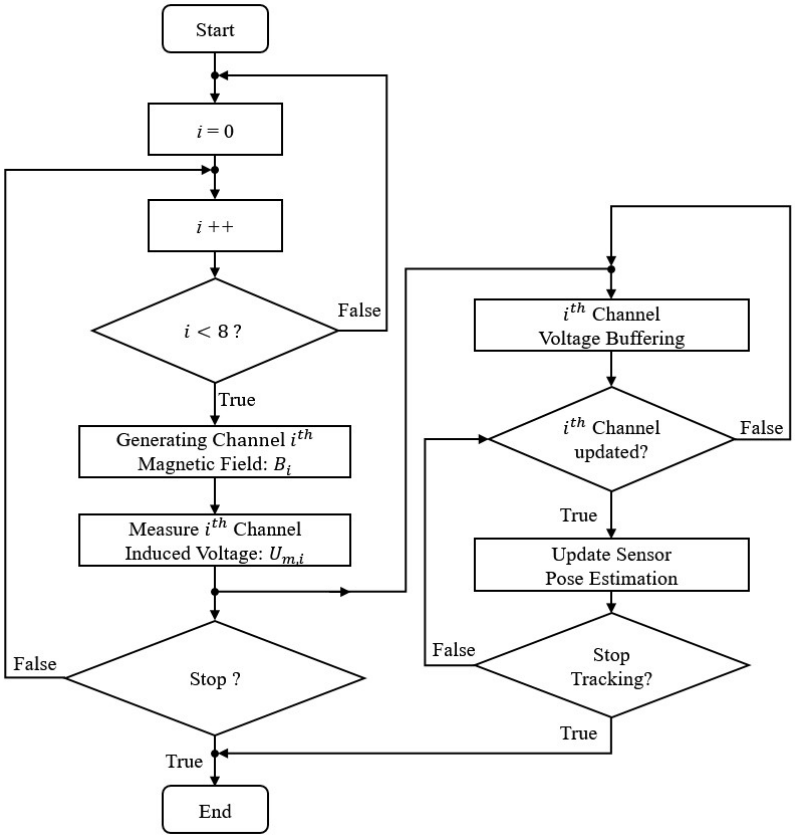

Figure 4.6: Flow chart of the moving–average–like method adapting the established prototype.

measurement after 8–channel voltages having been measured, the buffer voltages in the host PC is updated when one channel measurement is completed.

Compared to the FDM method, this moving–average–like TDM does not actually shorten the period for one complete voltage measurement in eight channels. Therefore, the actual tracking latency remains unchanged.

This approach smoothens the update in the estimated sensor poses and increases the refresh rate of the voltage measurement eight times

faster than the standard TDM method. There are no band–pass filtering required within this approach. Therefore it is compatible with the ramp–excitation method. As is evaluated in chapter 3, by applying this method, the experimental setup EMTS based on the ramp–wave excitation has achieved a $12.7Hz$ refresh rate in dynamic tracking.

4.3 DDS Waveform Generation in FPGA

The FPGA of the PXI system customizes the parameters of the generated signals, for example, the shape, amplitude, and frequency of the waveforms, etc. The direct digital synthesis (DDS) technology, which can be used to generated arbitrary waveform signals, were utilized for the analog output signal generation in the new measuring system. The analog waveform signals were synthesized from the values being stored in the lookup table (LUT). The signals can be arbitrarily shaped due to distinct applications. With DDS, signals are straightforwardly synthesized without the requirements of phase–locked loops, which reduces the complexity of implementation. DDS waveform generation technology allows to generate arbitrary waveforms for various testing purposes. For example, in the work being conducted in this thesis, sine–wave, quadratic–rectangular–wave and ramp–wave signals were utilized for different research purposes.

4.3.1 DDS Principle

The principle of DDS waveform generation is shown in the Figure 4.7. The phase accumulator uses the tuning word, which is defined by the sample clock, to set the precise frequency of the generated signals. The adder sums up the tuning word, and the $k - n$ bit remainder from the phase accumulator is used to ensure the precision of the signal frequency. The required arbitrary waveform is stored in the *nbit* LUT at different addresses. After being addressed in the phase accumulator, the syn-

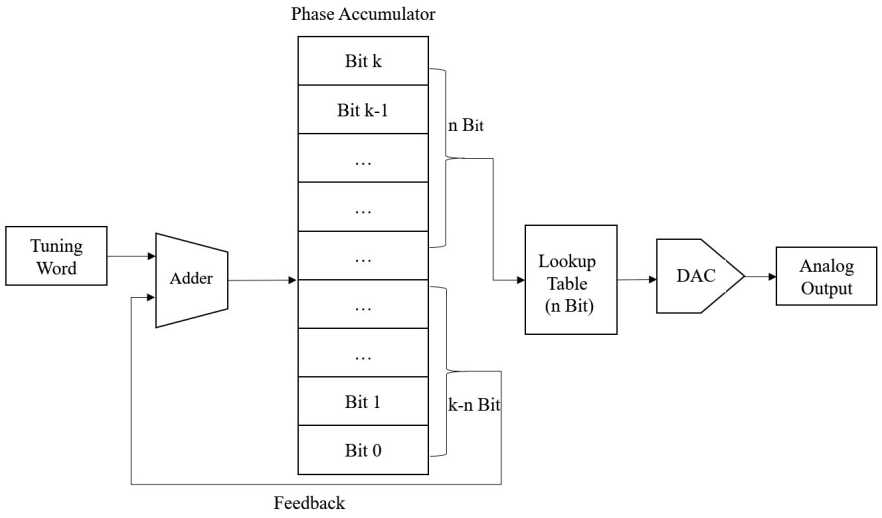

Figure 4.7: Simplified hardware block diagram of the DDS waveform generation (Image modified due to [Bra07])

thesized digital signal is then sent to the analog output terminal of the device through a DAC. Multiple DDS waveform generators can be implemented in the FPGA in sequential or parallel to create multi–channel EM fields.

In the developed EMTS prototype, the PXIe–7854R has a $40MHz$ on-board system clock, which is utilized to create the sample clock CLK_S for the frequency tuning word to update the accumulator value. It also determines the timing of the DAC process but does not directly control the frequency of the generated waveform signals. Figure 4.8 indicates the principles of defining the generated signals' frequency.

As is shown in Figure 4.8, at the each rising edge of the sample clock, the signal stored in the LUT of the FPGA is addressed for waveform generation. In this example, the sample clock is $40MHz \div 3 = 13.3MHz$.Therefore, the generated signal frequency is $13.3MHz \div 4 = 3.3MHz$.

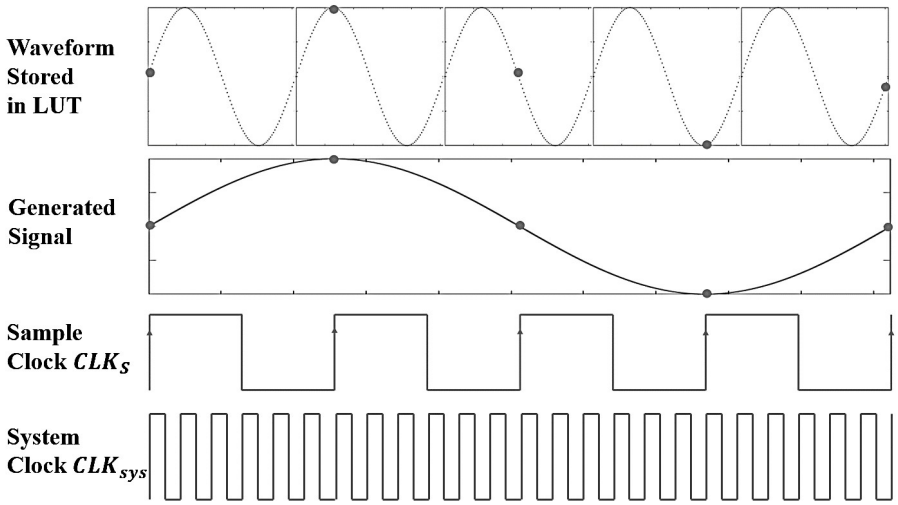

Figure 4.8: The principles of the lookup process in DDS waveform generation. (Image modified due to: [Uti13])

4.3.2 Frequency, Phase, and Amplitude Adjustment

The value of the phase accumulator determines the frequency of the generated waveform signals. Here, a 32–bit accumulator was chosen. The maximum accumulator value in decimal system is 4264967295 ($2^{32} - 1$). The value of accumulator increment was selected to define the intervals of addressing the data stored in the LUT. During one complete DDS process, once the maximum value of the accumulator is reached, a next look–up process starts immediately. By adjusting the value of accumulator increment, the frequency of the generated signals can be changed. The principle of the defining the signal frequency by accumulator increment is presented in Figure 4.9.

As is seen in the figure, when the value of the phase accumulator in increases from the angle θ_1 to θ_2 with the increment of $\triangle\theta$, the corresponding signals a and b stored in the LUT are addressed. The calculation of angular velocity from the phase increment is given by:

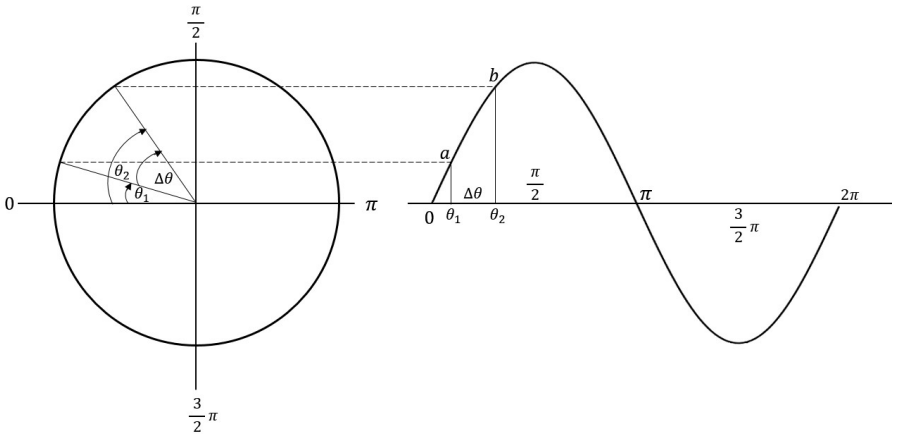

Figure 4.9: The principle of phase accumulator increment in the DDS waveform generation for sinusoidal signals.

$$\omega = \frac{\triangle\theta}{\triangle t}. \tag{4.1}$$

Here, $\triangle t$ is the time interval for each phase increment. In the FPGA's signal generation loop, the sample clock CLK_S is defined by clock ticks. For a $40MHz$ system, the clock tick is $1 \div 40MHz = 25ns$. The time interval can only be selected to be equal or greater than this value. As the example in Figure 4.8 shows, the sampling period is $25ns \times 3 = 75ns$. After knowing the angular frequency of the phase increment, the generated signal frequency can be calculated as:

$$f = \frac{\omega}{2\pi} = \frac{\triangle\theta}{2\pi \times \triangle t}. \tag{4.2}$$

As equation 4.2 illustrates, the frequency of the generated signal is proportional to the ratio of the phase increment and the time interval, i.e. the sample clock. To implement the frequency control in the FPGA, a simple solution is to fix the sample clock and only change the phase increment. The FPGA does not directly support the implementation of a phase accumulator in radians. A numerical conversion between the real

accumulator value and the phase accumulator value has been performed and is given as:

$$\triangle\theta = \frac{2\pi\triangle x}{2^{32}}. \tag{4.3}$$

Where $\triangle x$ is the numerical increment value which should be integer power of 2. From equation 4.2 and 4.3, the frequency of the signal can be calculated as:

$$f = \frac{\triangle x}{\triangle t \cdot 2^{32}}. \tag{4.4}$$

The frequency resolution can be increased by using larger accumulator value with more bits (as shown in Figure 4.7) of the phase accumulator.

In order to adjust the phase shift of the generated signal, one way is to directly add the phase-shift to the waveform stored in the LUT. However, for this, the FPGA needs to be re-compiled at each time. Alternatively, the phase shift adjustment is performed based on changing the shift in the decimal value of the entire accumulator range, as a ratio of a full cycle. For example, a $\frac{\pi}{2}$ phase shift is calculated to be $\frac{1}{4}$ of one cycle i.e. $\frac{\pi}{2} \div 2\pi$, which converts to $\frac{1}{4} \times 2^{32} = 1.074 \times 10^9$. This value was added to the phase accumulator in changing the phase shift of the waveform signal.

According to the manufacturer specifications, the analog output terminal of the *PXI-7854R* has a 16-bit resolution DAC with the analog output voltage range of $\pm 10V$. The amplitude of the waveform signals stored in the FPGA LUT is a digital value in the unit of bit. To fit the DAC resolution, a range of $16 - -bit$ integer, ± 32768 was selected. The conversion of the binary value of the signal amplitude in the LUT to a decimal value of the analog output is given as:

$$U = \frac{A}{2^{16}} \times 10(V). \tag{4.5}$$

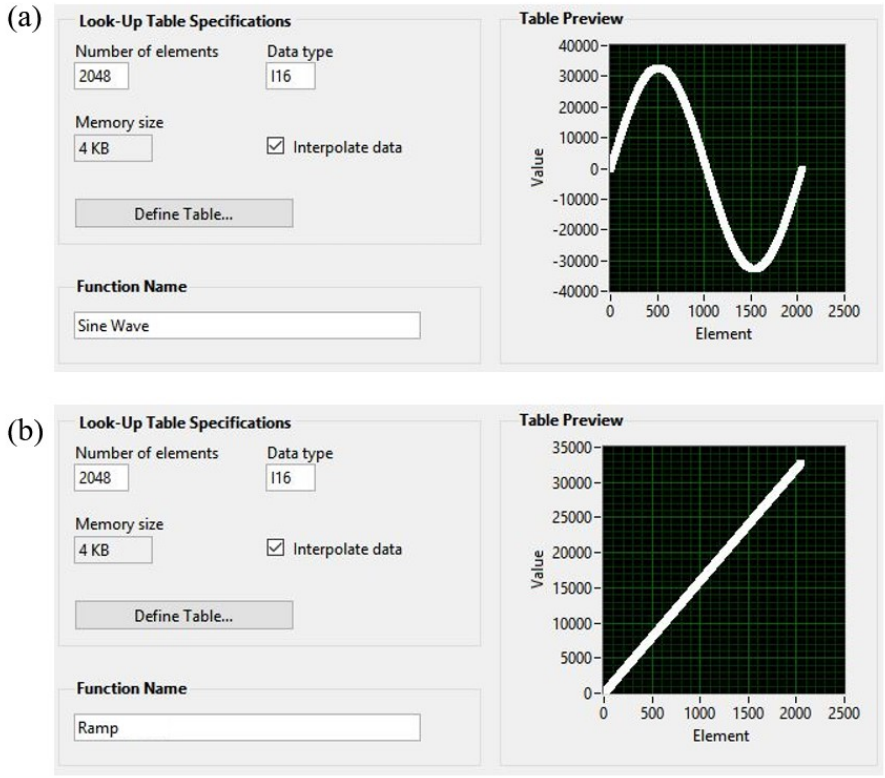

Figure 4.10: The signals stored in the FPGA LUT for the DDS waveform generation: (a) stored sine wave signal and (b) stored ramp signal.

Where, U and A represent the analog and the digital value of generated voltage signals. In this dissertation, sine–wave and ramp voltage signals have been generated for different applications. Figure 4.10 show the defined LUT in FPGA by using LabVIEW.

Similar to the explanations of Figure 4.9, the principle of DDS for the generation of the ramp signal is illustrated in Figure 4.11. It should be noted that, the ramp signal does have oscillatory components such as sinusoidal waveform. Therefore, instead of the angular frequency ω, only the fundamental frequency f is considered.

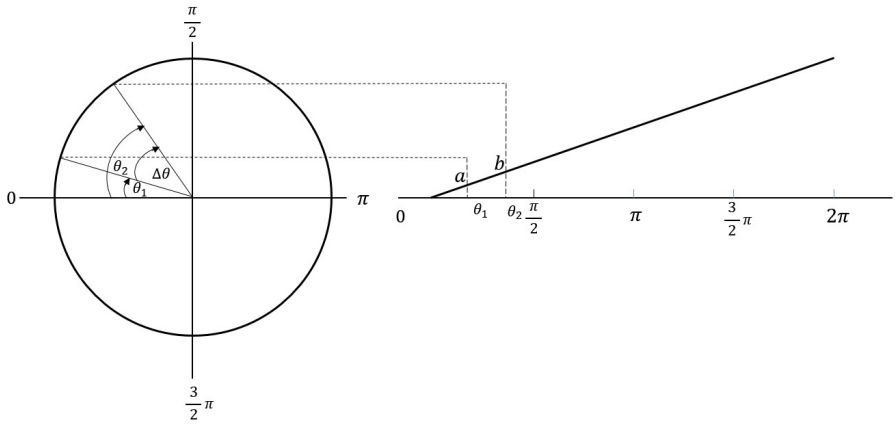

Figure 4.11: The principle of phase accumulator increment in the DDS waveform generation for ramp signals.

4.4 Data Acquisition in FPGA

The chosen DAQ device *PXI 7854R* was utilized to measure the voltage induced in the sensor coil. The DAQ process was implemented into the device using the LabVIEW FPGA module. The *PXI 7854R boards* utilize the integrated FPGA I/O nodes to directly read and write the values of the analog and digital channels. The best benefit of using FPGA is the ability to customize all the parameters in timing and triggering. multi–channel signal generation and data acquisition, simple algorithms, such as numerical calculation and signal processing can be parallelized in the hardware.

Timing is the most important parameter in advanced data acquisition. In LabVIEW FPGA, the sampling frequency can be simply defined by a timer T_S in a while loop. Multiple loops can be used to realize multi DAQ processes in parallel. Based on the experimental setup of the EMTS, there are multi–channel signals being generated but only one channel being acquired. The sampling frequency can be defined as $F_S = \frac{1}{T_S}$. The number of samples N_S for each sampling period can be de-

termined by the maximum iteration of a "for" loop. The execution time of the loop determines the sampling frequency, which could be adjusted by an additional timing controller. Additionally, digital trigger signals can be applied to synchronize the signal generation and data acquisition processes.

For transferring the measured data from the FPGA to the host PC, the direct memory access (DMA) communication was utilized. The DMA is a FIFO based method which transfers data between an FPGA target and the host PC. The DMA process runs only in the FPGA; there is no host process necessary. Thus, it is fast and efficient to use DMA to transfer the data between the FPGA and host. Figure 4.12 presents the DAQ process being implemented in the system setup.

The created DMA channel is unidirectional, i.e. the communications is only possible towards fixed direction. When the data transfers from the host PC to the FPGA target or multiple DAQ channels are necessary for certain applications, additional FIFO elements and DMA channels need to be created.

4.5 Analysis of the Generated and Measured Signals

In this section, the generated and measured voltage signals using the implementation methods introduced above is discussed. The generated voltage signals are monitored by an additional DAQ device *NI PXI-6281* (National Instrument, USA) which has an 18–bit input ADC which is higher than the 16-bit output DAC of the *NI PXI–7854R* utilized for signal generation.

As an example, for monitoring the voltage measurement, the sensor coil was fixed at a random location on the top of the field generator box. The voltage induced in the sensor coil by the magnetic filed of the first channel, was selected for visualization. The generated sinusoidal voltage and the measured voltage across the sensor coil applying the

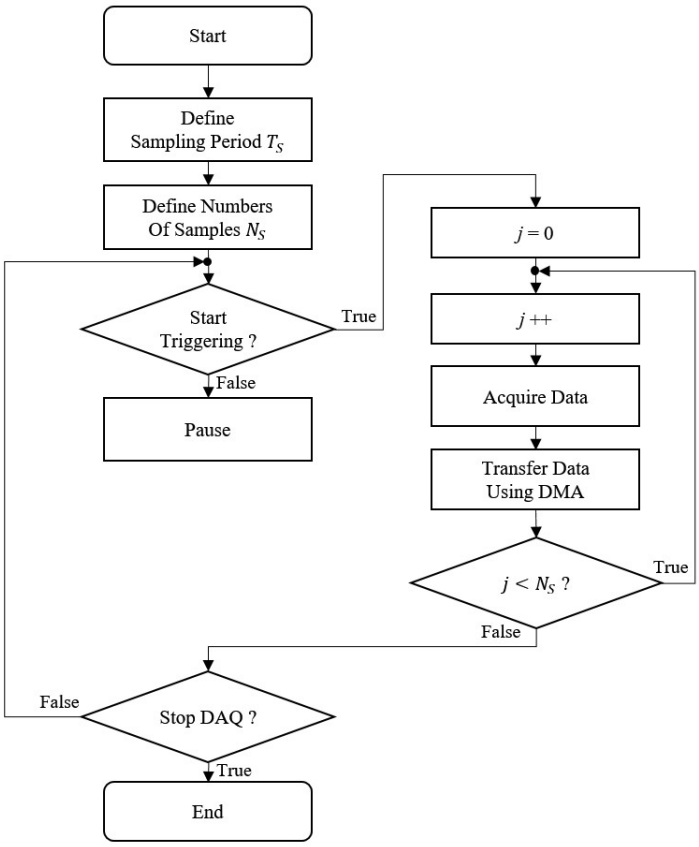

Figure 4.12: The DAQ process of the voltage measurement.

TDM method, are illustrated in Figure 4.14.

As is seen in Figure 4.14 (a), the frequency of the generated voltage applied to the transmitter coil of channel 1 is $1000Hz$ and the amplitude is $1V$ measured by the sensor coil. 4.14 (b) shows the multiple periods of the measured voltage signals. Due to the switch-on effect which could result in tracking errors, the first period was not taken into consideration for the sensor position estimation. As was implemented in the experimental setup, the number of periods were chosen to be 5 or 20 considering a faster measurement speed or a higher accuracy.

Figure 4.15 shows the measured signals of the first channel utilizing

Figure 4.13: The NI PXI–6281 device.

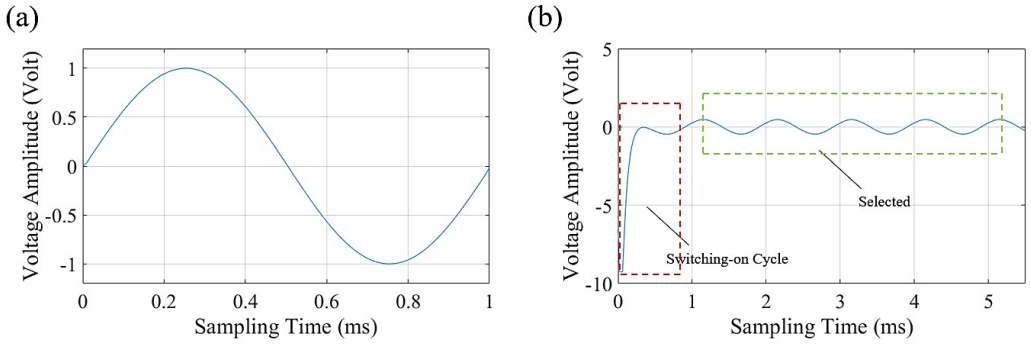

Figure 4.14: The generated sinusoidal voltage (a) and the measured voltage induced by the sensor coil in the first channels (b) using TDM.

the FDM method of the DAQ process. The frequency of the generated signal in the first channel is a 1650 Hz sine–wave signal.

As is illustrated in Figure 4.15, the ovserved switch–on effect of the measured signals using FDM is much longer than observed applying the TDM method. The reason is that the implemented FPGA band–pass filters required in the FDM method consume extra time to reach the steady state due to their impulse response. The filtered signals become stable after approximately $150ms$. Therefore, by applying the FDM method, the filtered signals in the first $150ms$ are still influenced by

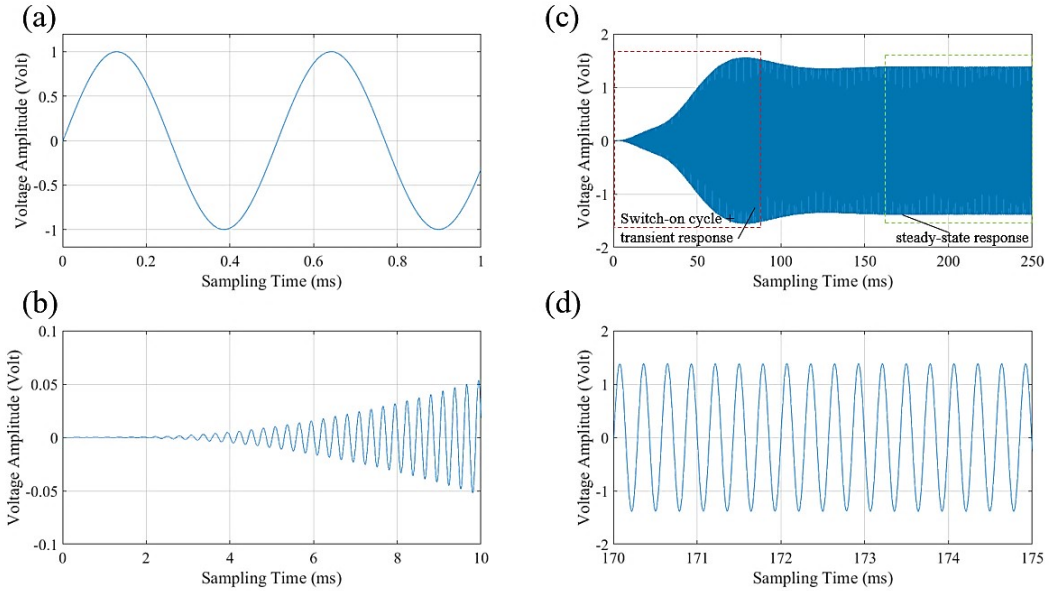

Figure 4.15: The measured voltage induced in the first of the eight channels using FDM (a) the generated one–channel $1800Hz$ sine–wave signal for the FDM method, (b) the measured voltages in the first $10ms$, (c) the measured voltages in the first 250 ms (d) selected periods of signals in the steady state for sensor pose estimation.

the impulse response. After that, 5 periods or 20 periods of signals (as discussed before) in the stable state were selected for estimation of sensor's position and orientation. In contrast to the TDM method, the signal generation and DAQ process run continuously once the program is started. Therefore, after the influence from the impulse response of the FPGA filter disappears, the system tracks the actual sensor locations continuously. Therefore, the influence of the impulse response can be neglected.

As discussed in Chapter 3, in this thesis a ramp signal with the period of $10ms$ was selected for the proposed method to reduce conductive distortions. Because the ramp signal does not consist of angular frequency and has a much lower fundamental frequency than the chosen sine–wave, the voltage induced in the sensor coil is much smaller than the sine–wave

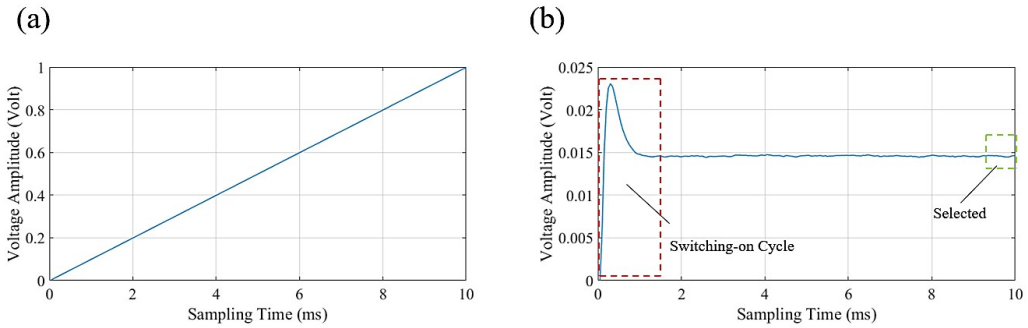

Figure 4.16: The generated ramp voltage signal including the turn–off state (a) and the measured voltage induced in the first of the eight channels (b) and the measured system response to the ramp excitation.

based methods. The generated ramp signal for the transmitter coil of the first channel and measured voltage induced in the sensor coil by first channel is shown in Figure 4.16.

4.6 Chapter Conclusion

In this chapter, the hardware implementations for building the prototype of an electromagnetic tracking system was introduced. An FPGA was utilized as the core component for DDS waveform generation and data acquisition. Apart from the traditional TDM and FDM methods in the DAQ processes, a more advanced moving–average–like TDM method was proposed to speed up the ramp excitation based method for reduction of conductive distortions.

Chapter 5

Advanced Error Analysis using an EMTS Simulator

5.1 Chapter Overview

For the real EMTS, the tracking errors are caused by various of sources, such as noise, metallic surroundings and inaccurate measurements of the transmitter's arrangement, etc. The errors are not easy to be distinguished from each other. Therefore, the analysis of individual system parameters is difficult. Based on the self–developed simulator, all the sources of errors can be separated to allow more advanced system analysis. An optimization algorithm of the transmitter coils' arrangement was developed based on the simulator. Another advantage of the simulator is, the ground truth of the sensor's pose can be well defined without introducing additional errors from the reference positioning systems and the registration process. In this chapter, the development of the simulation tool and the corresponding experiments were introduced.

5.2 Sources of Errors

As discussed in chapter 2, the estimation of the sensor pose is based on minimizing the differences between the measured and estimated voltages. There are three parts which can result in sensor pose errors: the inaccuracy of the voltage measurements, the errors of the estimated voltages and the convergence error of the optimization algorithm. Besides that, when the sensor coil is moved with a very fast speed, EMTS has a low resolution in estimation sensor's each movement. For the EMTS in use for image–guided interventions, registration errors exist between the tracking and imaging space, and also between imaging and target spaces. These sources of errors in EM tracking are introduced in the following subsections.

5.2.1 Errors in Voltage Measurement

As is given by equation 2.6, the precision of the measured voltages induced in the sensor coil $U_{mea,i}$ is an important factor that influences the accuracy of the estimated sensor's pose. The measured voltage signals consist of a higher level of noises when the distance between the sensor and transmitter coils becomes larger. In other words, with greater distances, the EMTS has larger sensor positional jitter errors which limits the working volume [HFB+06]. In clinical applications such as IGS, the field generator of the EMTS should be located close enough to the SROI to ensure the high tracking accuracy [RGN13]. Most commercial EMTS have much smaller working volumes compared to OTS [FHB+14, WTF04]. It is also a restriction which prevent EMTS being more widely accepted in clinical applications. Unknown or unavoidable metallic objects in the OR such as surgical instruments and electronic devices, which are nearby to the sensor coil, also cause significant errors in estimated sensor pose.

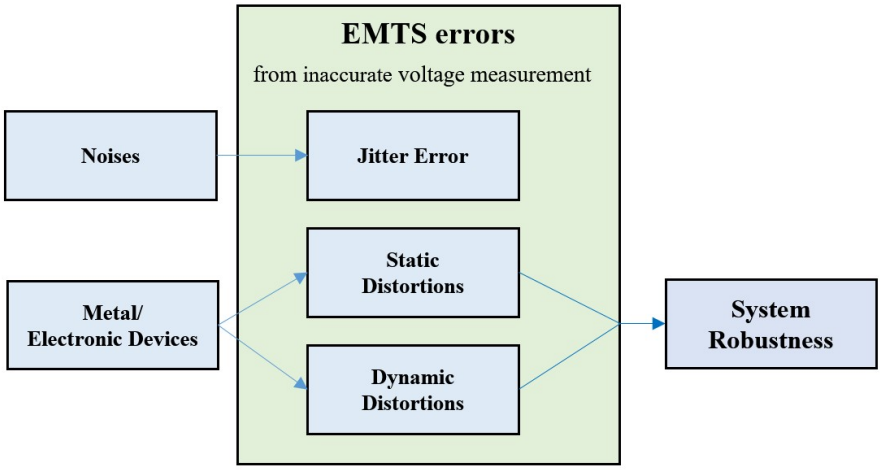

Figure 5.1: The errors of EMTS caused by inaccurate voltage measurement.

Figure 5.1 shows the errors in sensor pose estimation caused by an inaccurate voltage measurement. Besides the jitter error caused by the noises in voltage measurement, the distortions caused by metal and electronic devices were separately discussed thoroughly in Chapter 3.

5.2.2 Errors in Voltage Estimation

The estimated voltage $U_{est,i}$ is calculated from the known parameters of the system. It is potentially also a reason to cause inaccuracies in estimated sensor pose. In equation 2.5, most parameters for calculation of the voltage induced in the sensor coil are fixed values, e.g. the length, area and windings of the transmitter coils, AC signal frequencies and current flow across the coils. These parameters can easily be pre–calibrated. Therefore, they are not discussed in this chapter in particular. Errors could also exist in the mechanically predefined poses of the transmitter coils, which are measured using rulers and protractors. In reality, human eye based measurements are not always reliable. Therefore, Bien *et al.* developed a calibration algorithm to compensate pose errors of the trans-

mitter coils using a global pattern search algorithm [BR12]. Assuming the deviations of the transmitter coils' poses are $\triangle X_{t,i}$,$\triangle Y_{t,i}$,$\triangle Z_{t,i}$,$\triangle \Phi_{t,i}$, and $\triangle \Theta_{t,i}$, the real locations and the orientations of the transmitter coils were computed as:

$$\overrightarrow{r_{t,i}} = \begin{pmatrix} X_{t,i} + \triangle X_{t,i} \\ Y_{t,i} + \triangle Y_{t,i} \\ Z_{t,i} + \triangle Z_{t,i} \end{pmatrix}, \tag{5.1}$$

$$\overrightarrow{n_i} = \begin{pmatrix} \sin(\Theta_{t,i} + \triangle \Theta_{t,i}) \cos(\Phi t, i + \triangle \Phi t, i) \\ \sin(\Theta_{t,i} + \triangle \Theta_{t,i}) \sin(\Phi t, i + \triangle \Phi t, i) \\ \cos(\Theta_{t,i} + \triangle \Theta_{t,i}) \end{pmatrix}. \tag{5.2}$$

To find the global optima of n ($n \geq 5$) transmitter coils' poses, the real locations of the sensor coil should be known. As a reference positioning system, an optical tracking system *NDI Polaris Spectra* (Northern Digital, Canada) was used to measure more than $5 \times n$ locations of the sensor coil, because for there are 5 optima for each of the transmitter coils requires to be searched. The calibration algorithm minimizes the errors in sensor's pose estimation caused by the inaccurate location and orientation of the transmitter coil arrays. It also compensates other uncertainties, such as the offset of the amplifiers, for the whole EMTS setup.

5.2.3 Errors in Algorithm Convergence

Besides the errors from measured and estimated voltages, the process of minimizing the differences between the two voltages also creates errors in sensor pose estimation. The optimization method such as Levenberg–Marquardt algorithm used to optimize the non–linear parameters can result in errors when the gradient descent is too steep [Row96]. However, such errors are usually small and cannot be noticed during the intervention procedures.

5.2.4 Errors in Over–speed Sensor Movement

The three classifications above present the error sources which directly cause errors in sensor pose estimation. There is another type of errors caused by the rapid sensor velocity [Muc08], which is not directly expressed in equation 2.6. This error is corresponding to the system refresh rate as mentioned in Chapter 2. Assuming the EMTS has a refresh rate of m Hz, it means the system measures m samples each second. When the sensor coil stays stationary during the measurement, the sensor velocity error does not exist; when the sensor coil is moved during measurement in continuous time, no matter how slowly it is moved, in principle the errors exists because of the desecrate samples being recorded. For typical IGS such as endovascular surgery, the speed of inserting of the catheter is commonly distinguished in different ranges from less than $1mm/s$ up to greater than $6mm/s$ [TIU+07]. Getting hold of a commercial EMTS–NDI Aurora system into consideration as an example, the refresh rate was claimed by the manufacturer to be $40Hz$. Therefore, the system latency is calculated to be $25ms$ by:

$$\triangle t = \frac{1}{f_s}. \tag{5.3}$$

equation 5.4 presents how to compute the resolution in sensor movement, i.e. the minimum perceptible change in distance per samples.

$$\triangle d = v \times \triangle t \tag{5.4}$$

For the *NDI Aurora* system, who has a $40Hz$ refresh rate, assuming the catheter is moved at a velocity of $v = 6mm/s$ the resolution in sensor's movement can be calculated to be $0.15mm$. It means that the system cannot detect any sensor position changes which are below $0.15mm$ if the sensor speed is equal to or greater than $6mm/s$. Here, the $0.15mm$ resolution is an acceptable value for clinical utilization. However, for scenarios such as the EMTS having a lower refresh rate or the

catheter being moved faster, the system will have a much worse resolution which might become unacceptable.

The actual sensor pose is updated after the voltage measurement of all the channels is completed. For the TDM method (as discussed in Chapter 4), the system needs to wait until 8–channel voltage measurement to be complemented before updating the sensor pose once. It is the most inefficient way and causes the worst tracking resolutions. The FDM method is a much better solution. The parallel execution increases the update rate in voltage measurement for all the eight channels. Once the voltage measurement of the channel with the lowest excitation signal is updated, the actual sensor pose will be estimated. However, it does not support the ramp–excitation method. The improved TDM method does not increase the tracking speed to be eight times faster than the normal TDM method but smooth the measured sensor's movement.

5.2.5 Errors in the Registration Processes

For supporting instrument tracking in IGS, the coordinate system of the EMTS should be registered with the pre–scanned patient anatomy [FHB+14]. Before registration processes, the fiducial errors already exist in both tracking space from inaccurate measurements, and also in image space by identifying the exact markers' centroids. These errors are called fiducial localization error (FLE), which will negatively influence the tracking accuracy in IGS. Then, a so–called fiducial registration is performed [SMH+08]. It is a point–to–point based registration between physical–3D EM field and image space. The existing FLE and the point fitting cause the fiducial registration errors (FRE) . After fiducial registration, the target registration should be performed to overlay the real objectives – typically tumors or lesions, with the medical images. Both the FRE and the target registration errors (TRE) exist in medical applications [FWM98]. The classification of the registration errors is

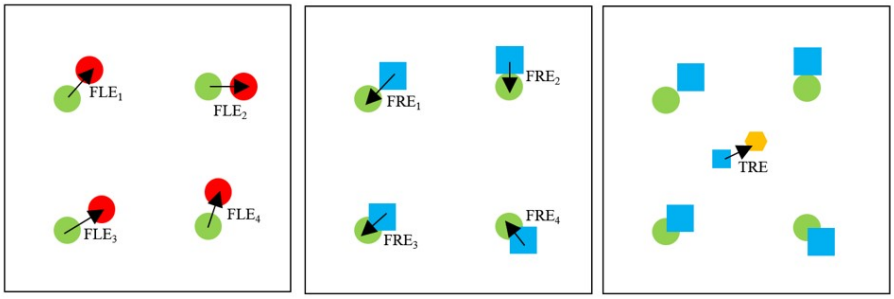

Figure 5.2: The types of registration errors. (a) FLE. The green circles show the real fiducials while the red circles stand for the measured fiducials. (b) FRE. The squares and the circles present the fiducials in the anatomical image and tracking spaces. (c) TRE. The hexagon shows the anatomical point in the area of the real surgical targets, e.g. tumors. Image modified due to: [FWM98].

presented in Figure 5.2.

Although the registration errors also refer to critical safety issues in interventional procedures, they are not directly related to the technical tracker accuracy of EMTS. In this thesis, the registration errors will not be further discussed.

5.3 Methods in Accuracy Evaluation

In evaluating the tracking accuracy of EMTS, research groups proposed different assessment protocols. The common point of these methods is that multiple locations of the sensor coil are measured by both EMTS and the reference positioning system. The reference positioning system should be precise enough, i.e. a much smaller tracking tracking errors than EMTS, such as *NDI Polaris Spectra* (Northern Digital, Canada) with a $0.35mm$ RMSE. Otherwise, the assessed tracking accuracy is not reliable. Research groups developed or employed different systems to measure the tracker's reference positions and orientations.

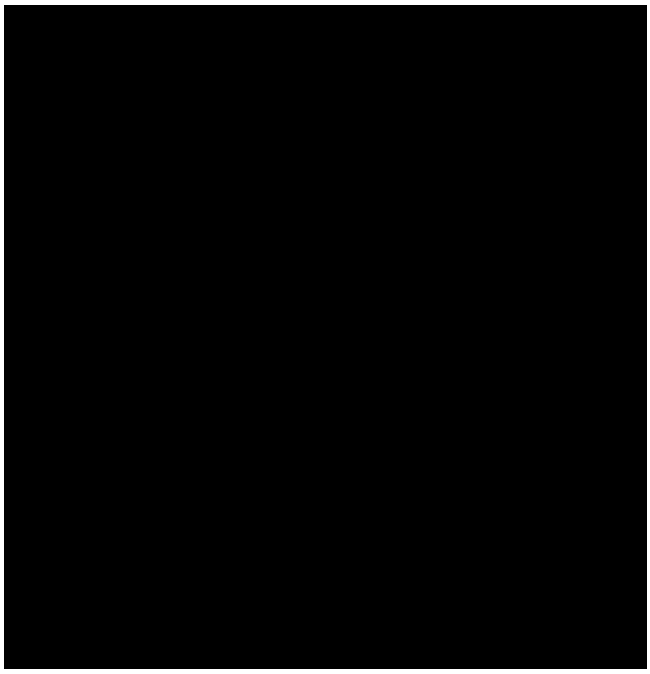

Figure 5.3: Accuracy evaluation phantoms for EMTS designed and developed by multiple groups. (a) Scheme of a poly–carbonate measurement plate labeled with X and Y axis. (Image source: [HFB+06]). (b) A Plexiglas cube phantom along X, Y and Z axis with one inserting direction. (Image source: [WYZ+07]). (c) The design of the accuracy assessment phantom with multiple trackers inserting orientations. (Image source: [KKK13]). (d) Hemispherical calibration device with 50 holes on the surface with different directions [FWLK03]

5.3.1 Phantom Based Assessment

Fixed–structure–based assessment in evaluating EMTS tracking accuracy is frequently suggested in the literature. The most popular method is to build an assessment phantom with holes at different directions and depths, wherein the magnetic sensor coil can be inserted. The locations and focal points of the hollows in the phantom were exactly pre–bored. They are employed as a reference positioning framework to evaluate the tracking accuracy of EMTS or other tracking systems such as OTS. Figure 5.3 shows the phantoms proposed by different groups.

As Figure 5.3 presents, the poly–carbonate reference plate in 5.3 (a) does not support accuracy evaluation in three dimensions. Based on this structure, only 2D– movements toward X and Y axes are permitted. The Plexiglas cube phantom in (b) allows a 3D measurement along X, Y and Z axis. Nevertheless, the orientation of the sensor coil can only be defined towards Z direction. Multi–orientation measurement can be realized by using the phantom design shown in (c). These assessment phantom–based measurements can be very precise due to the small construction tolerance. However, only limited directions of the sensor coil are able to be measured due to the fixed phantom structure. In these test phantom–based measurements, EM sensors are moved manually for quantitative measurements which are inefficient. It is possible to measure the sensor orientation accuracy using the hemispherical phantom shown in (d). However, just 50 holes limit the system to be evaluated in a more statistical way.

5.3.2 Modular Bricks Based Assessment

Besides using specially designed test phantoms, alternatively, another straightforward and low–cost way is to use modular bricks from *LEGO* (The LEGO Group, Denmark). Referable to the plastic construction and high precision in structure, using modular *LEGO* bricks to evaluate the tracking accuracy of EMTS was also suggested by other groups. The *LEGO* tower can be freely built for specific testing purposes.

It is simple to use LEGO bricks to define the volumetric test frames. The manufacturer claimed that the construction tolerances of each brick are not greater than $10\mu m$ [G+07]. However, significant errors could exist in the manually built *LEGO* towers towards Z direction. These errors are not easy to be distinguished from other sources of errors which add uncertainties in evaluating the accuracy of estimated sensor pose.

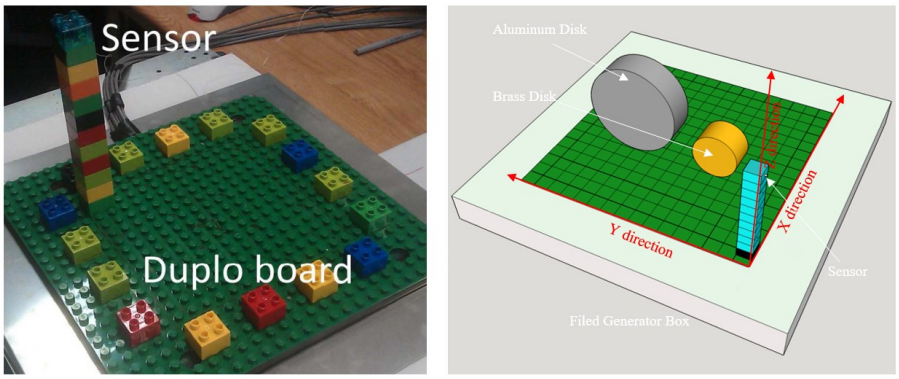

(a) (b)

Figure 5.4: Tracking accuracy evaluation setup using modular LEGO bricks. (a) The measurement setup in university Cork. Image source: [OCM15]. (b) The scheme of measurement setup to measure the tracking errors caused by metallic distorters [LHR15].

5.3.3 Robotic Based Assessment

3D robotic coordinate measuring machine (CMM) [WTF04] and similarly three–axis robot have commonly very high volumetric accuracy. They are often utilized as the reference positioning system to assess the accuracy of other 3D tracking systems such as EMTS and OTS. In evaluating the tracking accuracy of other systems, the tracker was fixed on the robot arm and moved in the measurement volume at multiple locations. Figure 5.5 shows a three–axis robot used by another group to assess the accuracy of the EMTS. The high accuracy and programmable movement of the robotic arms are the advantages of such robot systems. These robot–based tracking systems typically serve in a large measurement volume. When being used to evaluate the tracking error of EMTS, the metallic structure could also be a vital issue which should be carefully noted because it potentially influences on the tracker accuracy negatively.

Figure 5.5: The 3–axis robot utilized for evaluating the tracking accuracy of EMTS. Image source: [NJvJ08]

5.3.4 Optical–tracking Based Assessment

Compared to EMTS which usually have requirements in obtaining a less than $2mm$ positioning errors in sensor pose estimation, OTS have a much higher accuracy, for example, the *NDI Polaris Spectra* (Northern Digital, Canada) have a $0.35mm$ RMS error in a pyramid measurement volume of $1.63m^3$ which can be utilized to assess the tracking accuracy of EMTS. In the literature, the tracking systems were already proposed for measuring the tracking errors of EMTS and performing calibration [FWLK03]. The setup of the optical tracking–based method for accuracy evaluation proposed by Bien [BR12] was illustrated in Chapter 3.

5.3.5 Section Discussion

In this section, methods and apparatus proposed by other groups to evaluate tracking accuracy of EMTS are introduced. The prototype was

evaluated by using both *LEGO* tower and an optical tracking system as reference positioning systems. Due to the potential uncertainties in the precision of *LEGO* towers, OTS is preferred as the reference positioning system. However, errors exist in all the reference positioning systems presented above. The construction tolerance of the test phantoms, errors caused by building *LEGO* towers, besides the existing relatively small mistakes of the robotic and optical tracking systems prevent the ground truth to be recognized. In order to separately analyze the error level caused by different sources, an EMTS simulator was developed to provide the ground truth of the sensor locations while separately analyzing the error source. The EMTS simulator will be presented in the following section.

5.4 The Simulator Development

In this work, an EMTS simulator was developed to simulate the entire system flow based on the general EM tracking concept [PSPK10, OEG+14, BR12]. A typical EMTS has eight transmitter coils to generate sequential magnetic fields and one sensor coil to measure the voltage induced by the AC magnetic field. Because different systems use distinct analog circuit components, in the simulator, only the theoretical performance of EM tracking is simulated without considering the influences caused by errors in analog circuits, such as errors in analog–to–digital convertion and gain errors of the amplifiers. In reality, to evaluate the tracking accuracy, the reference poses of the sensor coil are provided by the reference positioning system. However, the actual sensor positions cannot be acquired by such measurement since the measurement error of the reference position systems always exist. This issue can be solved using the simulator in which the ground truth of sensor pose can be pre–defined. Based on the real sensor pose, inversely, the voltages induced in the sensor coil can be calculated as the "measured" voltages, as presented

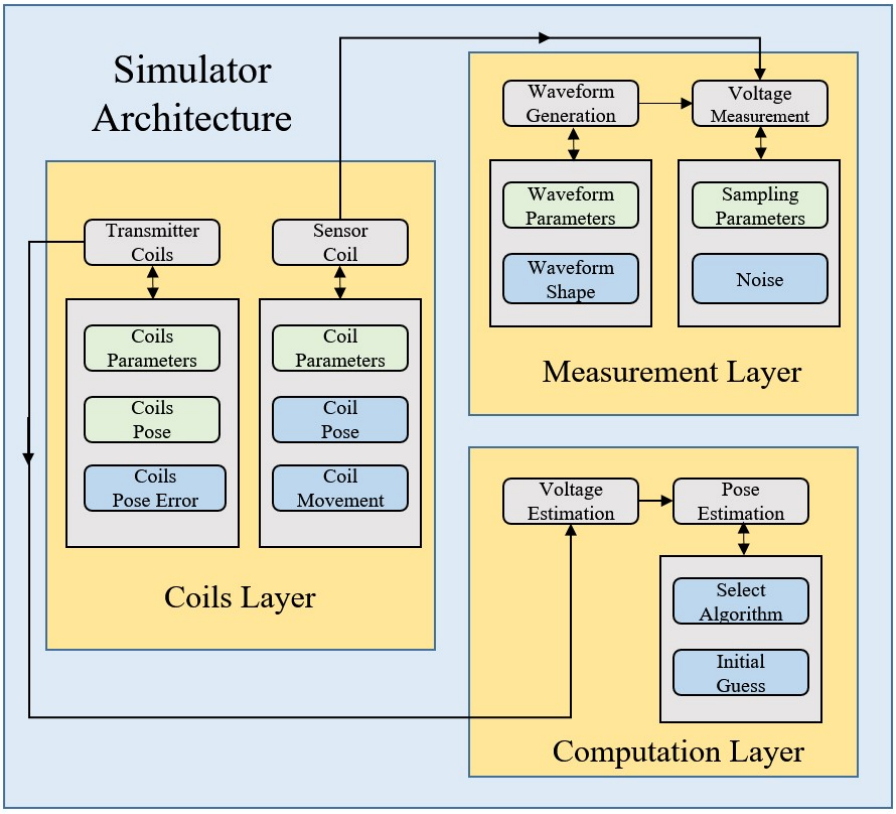

Figure 5.6: The architecture of the proposed EMTS simulator.

in equation 2.5. Noise signals can be added, causing differences in the measured and estimated voltages which lead to errors in the sensor pose estimation. in reality, noises in voltage measurement and errors in the reference positioning systems always exist while in the simulator, artificial noise signals can be selected between being wholly removed and being remained. Figure 5.6 shows the structure of the EMTS simulator.

In the coil layer, the parameters of the transmitter coils and sensor coil, such as length, the radius of the solenoid coils, the cross–sectional area of the coils and turns of windings, etc. can be individually defined. The parameters are assigned with the values of the EMTS prototype. In order to separately analyze the sources of errors as discussed in Section

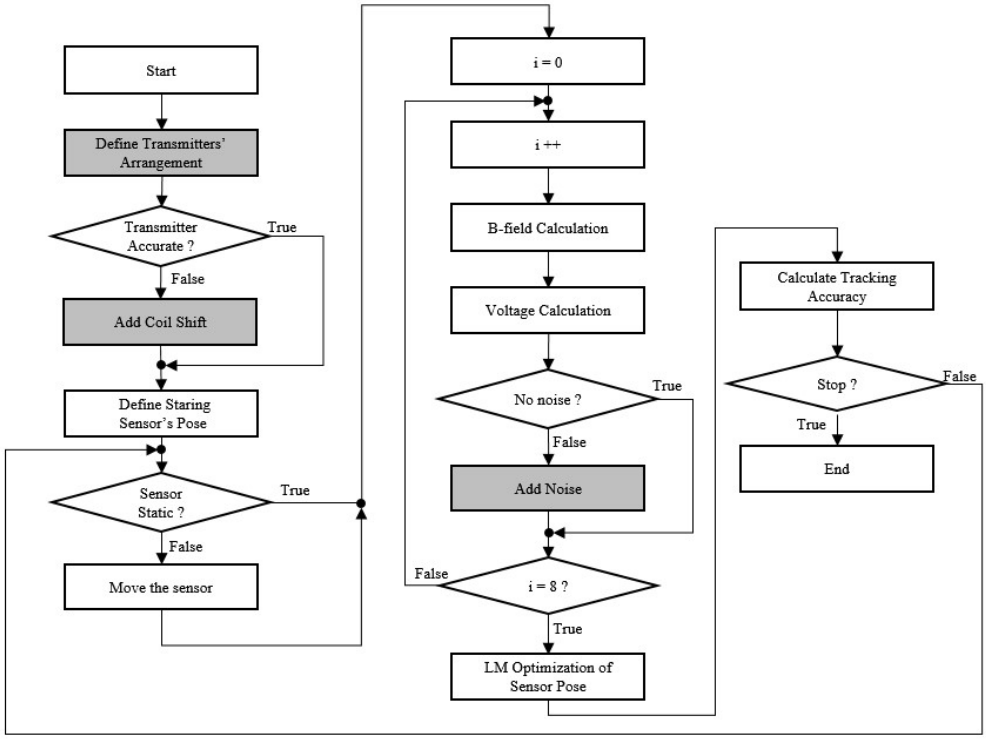

Figure 5.7: The flow chart of the developed EMTS simulator.

5.2 and test the performances of Kalman Filter and other system parameters, a particular workflow of the simulator is designed as is shown in Figure 5.7.

After starting the program, the positions of the transmitter coils and the starting pose of the sensor coil were firstly defined. After that, the errors of the transmitter coils' pose can be added. The sensor can be fixed at one location or moved following the implemented movement models for statistical analysis. Each transmitter coil is activated sequentially to generate magnetic fields. The voltages induced in each transmitter coil are estimated. Noise signals can be added into the voltages of each channel individually. After acquiring the voltages induced by eight

transmitter coils, the sensor's pose was estimated by utilizing *MATLAB* (Mathworks, USA) 'fsolve' function. The tracking accuracy influenced by the transmitter coils' arrangement with standard noises in measured voltages, was evaluated. As is illustrated in Figure 5.6, the gray blocks present the individual errors which can be added into the EMTS simulator. A user–friendly GUI has been designed to allow the end user to perform simulations without specific programming skills. The designed GUI is presented in Appendix A.

5.5 Accuracy Evaluation Using the Developed EMTS Simulator

In this work, the testing volume was chosen to be $500 \times 500 \times 500mm^3$ because this is reported to be a typical volume of interest (VOI) for accuracy evaluation [PC08b]. The starting position of the coil was $\begin{pmatrix} -250mm \\ -250mm \\ 50mm \end{pmatrix}$ in X, Y and Z axis. Considering the height of the transmitter coils, the sensor coil was initially moved 50 mm away from the origin in the Z direction. After the measurement had begun, the sensor coil was moved in the XY plane with a step length of $50mm$ in each X and Y direction for $11 \times 11 = 121$ locations. Then it was stepped $100mm$ in the Z direction before repeating the movement in XY plane. There were 726 poses of the sensor coil measured 121 points in 6 layers. The starting orientation of the sensor was selected to be $\begin{pmatrix} -180^\circ \\ -180^\circ \end{pmatrix}$, with the increasing step for each location being $360^\circ \div 726 = 0.4959^\circ$. After one complete measurement, the position and orientation of the sensor were increased to $\begin{pmatrix} 250mm \\ 250mm \\ 50mm \end{pmatrix}$ and $\begin{pmatrix} 180^\circ \\ 180^\circ \end{pmatrix}$. The defined ref-

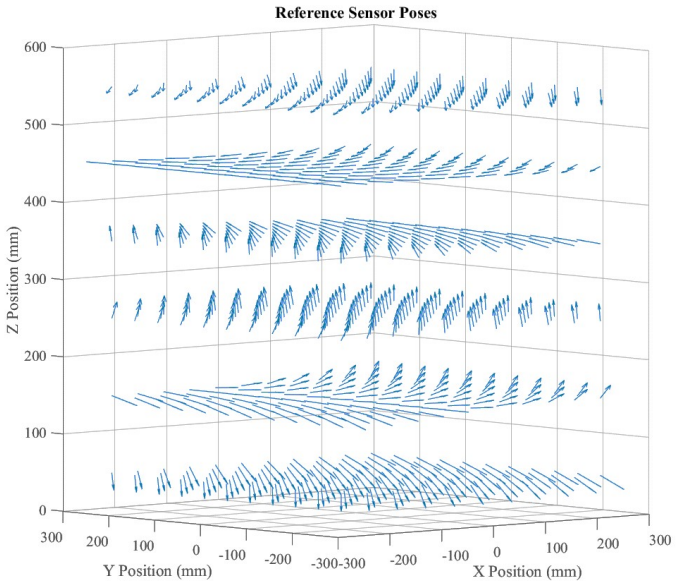

Figure 5.8: The reference positions and orientations of the sensor coil defined within the EMTS simulator.

erence positions and orientations of the sensor coil within the simulator are presented by Figure 5.8.

5.6 Advanced System Analysis Using the Simulator

5.6.1 Accuracy Variations with the Changes in the Spatial Arrangement of the Transmitter Coils

The predefined positions and orientations of the transmitter coils as is shown in Table 5.1 were randomly predefined. In this evaluation, different orientations and the positions of the transmitter coils were chosen to analyze the influence on the tracking accuracy due to the different transmitter coils arrangement. Figure 5.9 presents the arrangement of the transmitter coils in the real experimental setup and examples in the EMTS simulator.

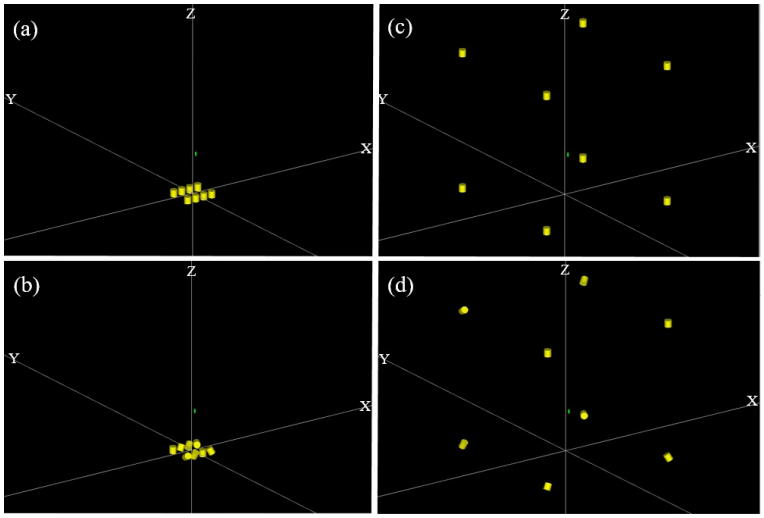

Figure 5.9: The stochastically defined position and orientation of the eight transmitter coils: (a) single–plane–single–orientation, the standard transmitter coil arrangement, in one XY plane with one orientation for all the coils, (b) single–plane–multi–orientation, the transmitter coils with multiple orientations in one XY plane, (c) single–orientation and (d) multi–orientation around the testing VOI.

The field generators (FG) of commercial EMTS generally have a small size, e.g. NDI Aurora Planar FG (Northern Digital, Canada) is $200 \times 200 \times 70mm^3$ in length, width and height respectively. According to this, the different poses of the transmitter coils are defined in the simulator in order to analyze the influences on the tracking accuracy caused by coil arrangement. Figure 5.9 (a) and (b) show the poses of the transmitter coils and Table 5.1 shows the detailed spatial arrangement of the coils.

In Figure 5.9, the yellow and green cylinders represent the transmitter and sensor coils respectively. The transmitter coils were firstly placed within such 3D space with a standard arrangement with all the coil faced towards one orientation, as is presented in Figure 5.9 (a). After that, in 5.9(b), each coil was added with multiple 20^o and 30^o in yaw (Φ) and pitch (Θ) angle shift. Figure 5.9 (c) and (d) are the stochastic coils' arrangement around the testing VOI. The detailed arrangement is

Table 5.1: The transmitter coils' stohastic arrangement according to Figure 5.9.

Coil Arrangement	Coil No.	1	2	3	4	5	6	7	8
Single-Plane	$X(mm)$	-60	-20	20	60	-60	-20	20	60
	$Y(mm)$	50	50	50	50	-50	-50	-50	-50
	$Z(mm)$	0	0	0	0	0	0	0	0
around VOI	$X(mm)$	-300	-300	300	300	-300	-300	300	300
	$Y(mm)$	-300	-300	300	300	300	300	-300	-300
	$Z(mm)$	600	0	600	0	600	0	600	0
Single-Orientation	$\Phi(^o)$	0	0	0	0	0	0	0	0
	$\Theta(^o)$	0	0	0	0	0	0	0	0
Multi-Orientation	$\Phi(^o)$	0	20	40	60	80	100	120	140
	$\Theta(^o)$	0	30	60	90	120	150	180	210

shown in Table 5.1.

Using the accuracy evaluation method as is introduced in Section 5.5, the accuracy assessment was performed. Figure 5.9 shows the result of the tracking accuracy of EMTS applying transmitter coils' arrangement as shown in Figure 5.10.

As demonstrated by Figure 5.10 (a) when the coils are facing to only one direction, even at lower layers, large orientation errors exist. Compared to the results for other scenarios, both position and orientation error are much greater. The tracking accuracy is increased by placing the planar transmitter coils with multiple orientations as (b) illustrate. The tracking accuracy is significantly improved by placing the transmitter coils around the testing VOI. Multiple orientations of the transmitter coils also benefit from the improvement of tracking accuracy. The detailed description of the tracking accuracy is indicated by Table 5.2.

5.6.2 Optimization of the Spatial Arrangement of the Transmitter Coils

The signal quality, represented by the signal to noise ratio (SNR) of the measured voltages, influences the tracking accuracy [LSH+10]. As seen in equations 2.1 – 2.4, the poses of the transmitter coils and the sensor coil

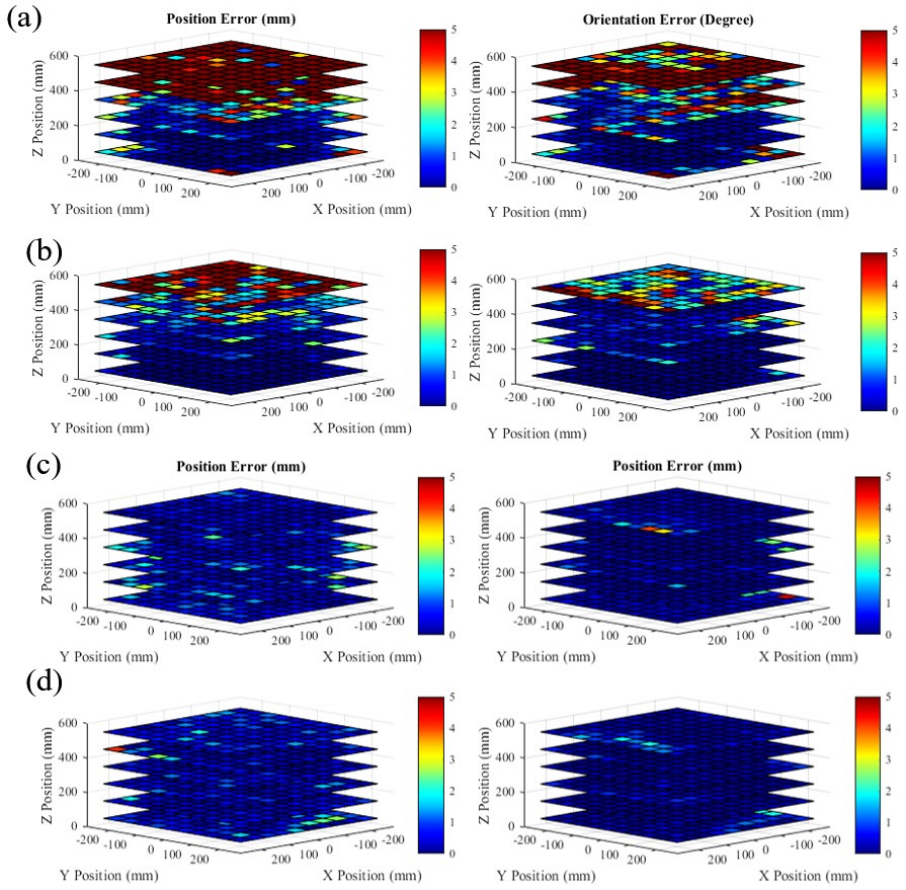

Figure 5.10: The plot of sensor position error according to stochastic coil arrangement as indicated in Figure 5.9.

affect the amplitude of the voltages induced by the transmitter coils. The aim is to find the maximum of the measured mean voltage U_{mean} for all the testing points by changing the spatial arrangement of the transmitter coils. *MATLAB* "patternsearch" function was selected to realize this optimization process. In this application, the objective function to be optimized is chosen to be the absolute value of the reciprocal of the mean voltage given by:

$$F_1 = |\frac{1}{U_{mean}}|. \tag{5.5}$$

In this optimization process, 726 positions of the sensor coil were chosen, and at each position, the sensor coil was vertically faced to the XY, XZ and YZ planes individually. Therefore $726 \times 3 = 2178$ sensor poses were used. The vector coils' arrangement to be optimized are defined as an 8×5 matrix:

$$\triangle x = \begin{bmatrix} \triangle X_1 & \triangle Y_1 & \triangle Z_1 & \triangle \Phi_1 & \triangle \Theta_1 \\ \triangle X_2 & \triangle Y_2 & \triangle Z_2 & \triangle \Phi_2 & \triangle \Theta_2 \\ . & . & . & . & . \\ . & . & . & . & . \\ \triangle X_8 & \triangle Y_8 & \triangle Z_8 & \triangle \Phi_8 & \triangle \Theta_8 \end{bmatrix}. \tag{5.6}$$

Selecting the initial poses of the transmitter coils is important for the "patternsearch" algorithm because according to the manufacturer's instructions [1], "patternsearch" can find the local minimum. Firstly the optimization by choosing initial poses of the transmitter coils within a standard box volume, which are similar to the planar field generators of commercial products, was performed. (see Figure 5.11 (a)) For this approach, there are three other preconditions for the optimization. First, the transmitter coils should be placed out of the testing volume of sensor coil movements. Second, the coils should be positioned at different locations, with a minimum spacing to allow them to be mechanically separated. The calculation of the minimum distance is given by:

$$L_{min} = \sqrt{R_t^2 + (\frac{D_t}{2})^2}, \tag{5.7}$$

where R_t is the radius and D_t is the height of the transmitter coils. The third precondition is that the boundaries of the searching vector for the pattern search algorithm should be set within a box-volume, i.e. the upper boundary of Z distance is selected to be smaller than $70mm$ which

[1] https://de.mathworks.com/help/gads/patternsearch.html

is similar to the commercial products. After that, another optimization by removing the boundary limitation into consideration was performed. Therefore, the optimization was performed in a pure 3D volume. After performing the optimization by searching the maximum of the voltages across the magnetic sensor, the minimum RMSE of the positional accuracy was chosen as the optimization target. For this approach, the function to be optimized is given by equation 5.8:

$$F_2 = \sqrt{\frac{\sum_{i=1}^{n} E_{p,i}^2}{n}}, \tag{5.8}$$

here, $E_{p,i}$ is the sensor position error at each point in the test volume. The optimizations were performed twice similar to searching the maximum voltage. The results have been compared as shown in Table 5.2.

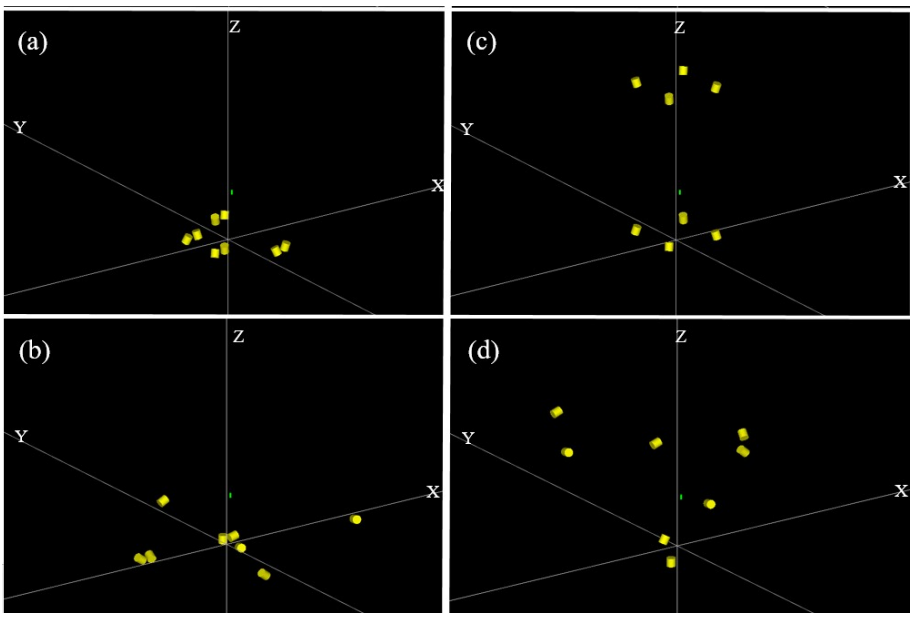

Figure 5.11: The optimized position and orientation of the eight transmitter coils: in a box area using (a) maximum voltage and (b) minimum position error as the object for the optimization; in a 3D VOI using (c) maximum voltage and (d) minimum position error as the subject matter for the optimization.

Table 5.2: The optimized spatial arrangement of the transmitter coils.

Coil Arrangement	Coil No.	1	2	3	4	5	6	7	8
Optimization -	$X(mm)$	74	112.90	-114	-72.90	74	112.90	-114	-72.90
Maximum Voltage	$Y(mm)$	184	182.90	-84	-82.90	-184	-182.90	84	82.90
(Box Shape)	$Z(mm)$	0	8.80	0	8.80	0	8.80	0	8.80
	$\Phi(^o)$	45	225	45	45	135	315	315	135
	$\Theta(^o)$	153.65	162.47	206.35	342.47	206.35	17.53	206.35	197.53
Optimization –	$X(mm)$	-310	270	20	60	–60	480	20	60
Minimum RMS Error	$Y(mm)$	50	50	50	50	-300	-50	-50	450
(Box Shape)	$Z(mm)$	0	0	0	0	0	0	0	0
	$\Phi(^o)$	1	257	31	0	6	256.50	251	0
	$\Theta(^o)$	125.50	110	0	256	128	255.50	78.25	63.50
Optimization -	$X(mm)$	97.20	97.20	-97.20	-97.20	97.20	97.20	-97.20	-97.20
Maximum Voltage	$Y(mm)$	97.20	97.20	-97.20	-97.20	-97.20	-97.20	97.20	97.20
(Around VOI)	$Z(mm)$	571.20	28.80	571.20	28.80	571.20	28.80	571.20	28.80
	$\Phi(^o)$	45	225	45	45	135	315	315	135
	$\Theta(^o)$	197.75	197.75	162.25	17.75	162.25	134.25	162.25	162.25
Optimization -	$X(mm)$	-280	-280	280	280	-280	-30	-220	280
Minimum RMS Error	$Y(mm)$	220	-280	30	30	280	30	-280	220
(Around VOI))	$Z(mm)$	330	520	330	270	455	20	80	20
	$\Phi(^o)$	258	0	255	0.25	0	1	273	257.50
	$\Theta(^o)$	256	251.50	129	132	71	30	0	257.50

For each scenario, the tracking accuracy was evaluated. This experiment aims to analyze the influence of the different transmitter coil arrangements on the tracking accuracy. The result is shown in Figure 5.12.

Comparing the Figure 5.10 and Figure 5.12, the optimization improves the tracking accuracy in a box area and in a 3D volume. The detailed comparison among all the different scenarios is given in Table 5.3.

In Table 5.3, (1) to (4) indicate the tracking error due to the non-optimized coils' arrangement as is shown in Figure 5.9 and (5) to (8) shows the optimized spatial arrangement of the transmitter coils as Figure 5.11 shows. The results illustrate that choosing the sensor position RMSE as the objective function let the system have an even better accuracy. In the box–area, the both of the optimized coil arrangement can be easily applied in reality. However, as shown in Figure 5.11 (d), the

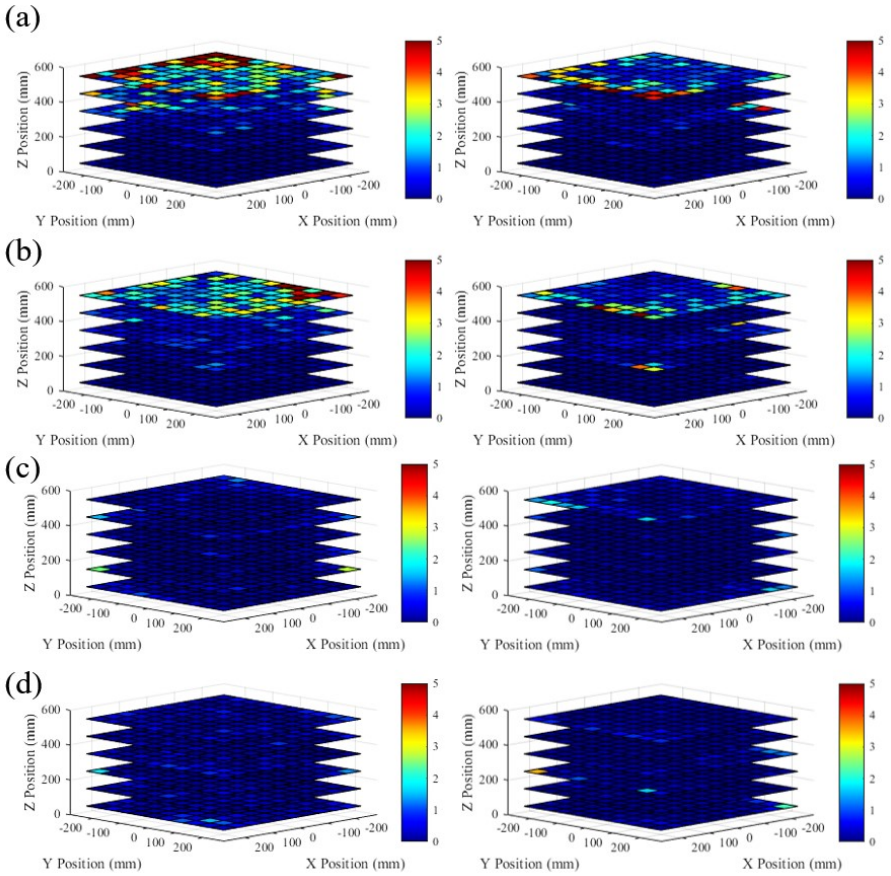

Figure 5.12: The plot of sensor position error according to optimized coil arrangement as indicated in Figure 5.11.

optimized transmitter coils are not symmetric to each other in a 3D VOI, which may add complexities in the construction process.

As is illustrated by the analyzed result using the simulator, the proposed algorithm of optimization of the transmitter coils' arrangement largely improves the tracking accuracy. The optimization result using different optimization objects were compared. The result using equation 5.5 as the object is even better than using equation 5.8 as the subject matter for optimization. However, the optimized transmitter coils' poses using equation 5.8 is more symmetric to each other which may reduce

Table 5.3: The tracking errors due to the different spatial arrangement of the transmitter coils.

Coil Arrangement	1	2	3	4	5	6	7	8
Position Error (mm)								
Mean	7.98	1.67	0.84	0.61	0.57	0.52	0.24	0.22
RMS	17.02	3.41	1.60	1.15	0.80	0.72	0.48	0.31
Max	128.91	31.11	10.16	11.21	6.45	6.73	3.86	1.72
95th Percentile	36.19	6.75	3.50	2.59	1.58	1.43	0.97	0.65
Orientation Error (^{o})								
Mean	6.49	1.60	0.84	0.50	0.46	0.38	0.32	0.26
RMS	19.07	6.29	5.19	1.84	1.61	1.27	1.16	1.03
Max	265.42	78.89	118.68	32.3	28.69	16.61	20.32	17.56
95th Percentile	28.18	4.62	2.82	1.78	1.52	1.16	0.97	0.80

the complexity of the construction.

5.6.3 Testing the Performance of the Calibration algorithm

Human-eye-based measurement errors exist in the mechanically predefined pose of the transmitter coils, which negatively influence the tracking accuracy of EMTS. Bien *et al.* developed a calibration method to compensate pose errors of the transmitter coils using a global pattern search algorithm [BR12].

In this experiment, a standard spatial arrangement of the transmitter coils – single-plane-multi-orientation was used, as Figure. 5.9 (b) illustrates, because it is a most conventional planar field generator without optimization. in reality, errors could exist in measuring the poses of the transmitter coils. Here, a random shift in position, between $-0.5mm$ and $0.5mm$, and in orientation, between -0.5^o and 0.5^o, are added to each transmitter coil. Table 5.4 shows the shifts being added to eight transmitter coils. *MATLAB* 'rand' function is used for random number generation.

To evaluate the performance of the calibration technology more statically, the random shifts as illustrated by Table 5.4 illustrate are increased by a factor of 10 and 100. Therefore, the calibration was performed 3

Table 5.4: The added shift to each of the transmitter coils in 0.5 in mm and ^{o} range.

Coil No.	1	2	3	4	5	6	7	8
$\triangle X(mm)$	0.1011	0.0369	-0.0492	-0.3852	-0.1208	-0.4132	-0.0382	-0.2443
$\triangle Y(mm)$	0.2956	-0.1565	-0.4444	0.3971	0.4929	0.3175	0.1244	0.1419
$\triangle Z(mm)$	-0.2684	0.4684	0.3638	0.3123	-0.1747	-0.0577	0.2663	0.1636
$\triangle\Phi(^\circ)$	0.0491	0.3687	-0.3103	0.4939	0.3095	-0.2088	0.2121	-0.2074
$\triangle\Theta(^\circ)$	0.3339	-0.2371	-0.4461	0.0313	-0.3451	-0.3193	-0.1298	-0.0436

times with the error range in $0.5mm$, $5mm$ and $50mm$ in position shift, and 0.5°, 5° and 50° in orientation shift. In this evaluation, no noise signals were added into the measured voltages. Only the influences due to the change in transmitter coils' poses were considered. The testing volume was the same as defined in Section 5.5.

The measurement errors of the transmitter coils' positions and orientations were reduced to approximately to 0 mm or ° for all of the 3 scenarios. Figure 5.13 shows the result of cumulative errors of the transmitter coils' positions and orientations after calibration.

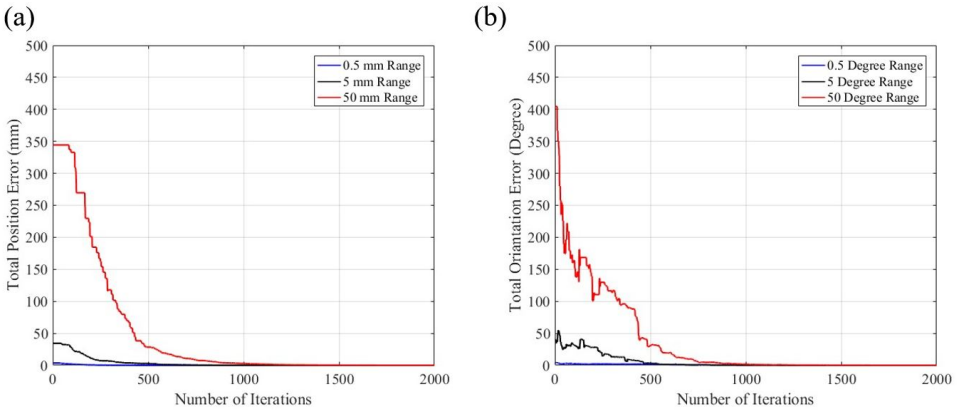

Figure 5.13: The (a) position error and (b) orientation error of the transmitter coils before and after being calibrated.

As Figure 5.13 presents, the calibration algorithm corrects the measurement errors well, when the measurement errors are in the range of $0.5mm$, $5mm$ and $50mm$ or 0.5°, 5° and 50°. The difference is that with

larger errors, the calibration algorithm needs more iterations to proceed. After being calibrated, the total errors of the transmitters have all being reduced to be smaller than 1×10^{-4} in mm and in $^\circ$ in position and orientation. The poses being corrected are precise enough and does not influence the tracking accuracy. The result of tracking accuracy before and after performing the calibration is indicated by Figures 5.14 and 5.15.

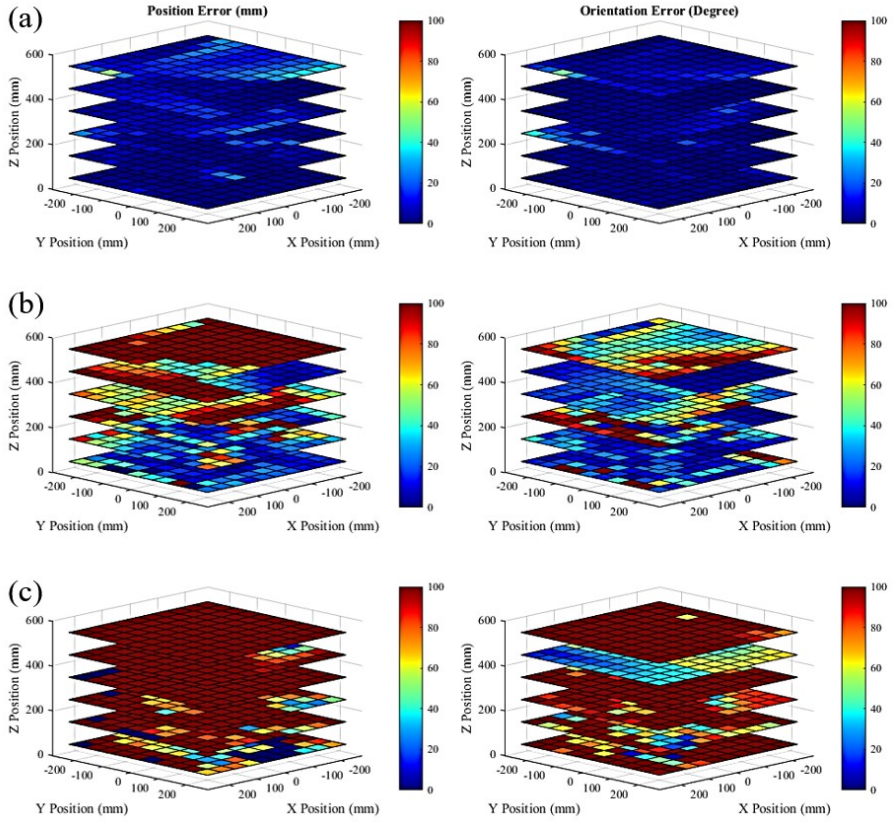

Figure 5.14: The tracking errors due to the measurement errors in the transmitter coils pose – before calibration. The pose errors of the transmitter coils are in range of (a) 0.5 in mm and in $^\circ$, (b) 5 in mm and in $^\circ$ (c) 50 in mm and in $^\circ$.

As illustrated in Figure 5.14 and Table 5.5, before the calibration, the errors increase when the measurement error of the transmitter coils

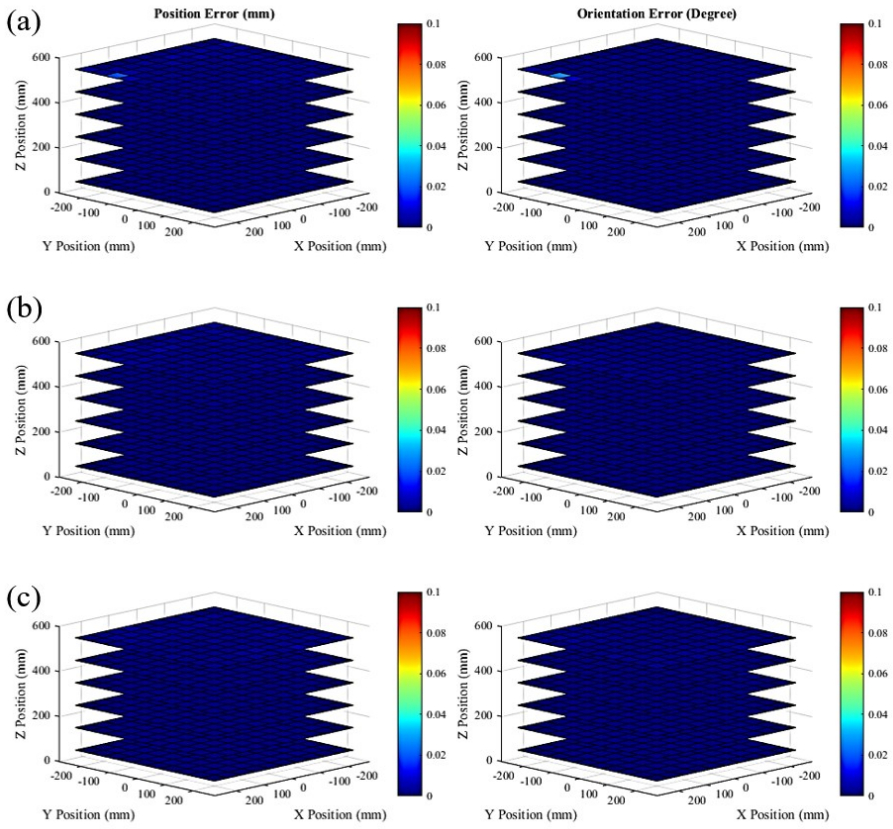

Figure 5.15: The tracking errors due to the measurement errors in the transmitter coils pose – after calibration. The pose errors of the transmitter coils are in range of (a) 0.5 in mm and in °, (b) 5 in mm and in ° (c) 50 in mm and in °.

poses becomes larger. Even within a small range, i.e. the measurement errors are smaller than $0.5mm|^o$, the system has a $10.7mm$ RMSE at the estimated sensor position. It is already not acceptable for the clinical requirement. As shown in Figure 5.15 and Table 5.5, after performing the calibration, the tracking errors were reduced to an ignorable level. Although for larger shift the calibration algorithm needs more iterations to find the global optimum, it works properly even when the shift range is at 50 mm and in ^{o}. After performing the calibration, the RMSE of sensor

Table 5.5: The tracking errors due to the measurement errors in the transmitter coils' poses: (1-3) before calibration and (4-6) after calibration.

Position Error (mm)	1	2	3	4	5	6
Mean	7.33	67.99	236.52	0.0005	0.0005	0.0004
RMS	10.71	94.26	287.36	0.001	0.001	0.001
Max	72.94	364.25	1004.72	0.02	0.02	0.01
95th Percentile	22.45	202.75	563.20	0.002	0.002	0.002
Orientation Error (^{o})						
Mean	6.30	41.08	126.90	0.0005	0.0005	0.0003
RMS	17.15	63.97	149.85	0.002	0.002	0.001
Max	161.05	314.38	444.30	0.05	0.04	0.002
95th Percentile	18.89	131.29	278.91	0.002	0.002	0.001

position and orientation errors have been reduced to below $0.001mm$ and 0.002^o.

After testing the performance of the calibration algorithm in a noise-free scenario, the noise effect was introduced, $-100dBW$ and $-80dBW$ additive–Gaussian–white noises (AGWN) were introduced in the measured voltages to simulate the real-world scenario. The testing volume was the same as defined in the evaluation without considering the noise effect.

As Figure 5.16 (a) presents, where there are no noise signals in the measured voltages, the calibration algorithm corrects the measurement errors. As Figure 5.16 (b) and (c) illustrate, when the noises exist in the measured voltages, the calibration cannot totally eliminate measurement error. With a higher level of noise, the performance of the calibration becomes worse.

As presented in Figure 5.17, the calibration algorithm of correcting transmitter coils measurement errors requires a certain amount of sensor location data. When less than 100 points were applied, the calibration algorithm cannot rectify the measurement errors. When more than 200 testing points were utilized, the calibration algorithm works properly to reduce the error to a negligible level.

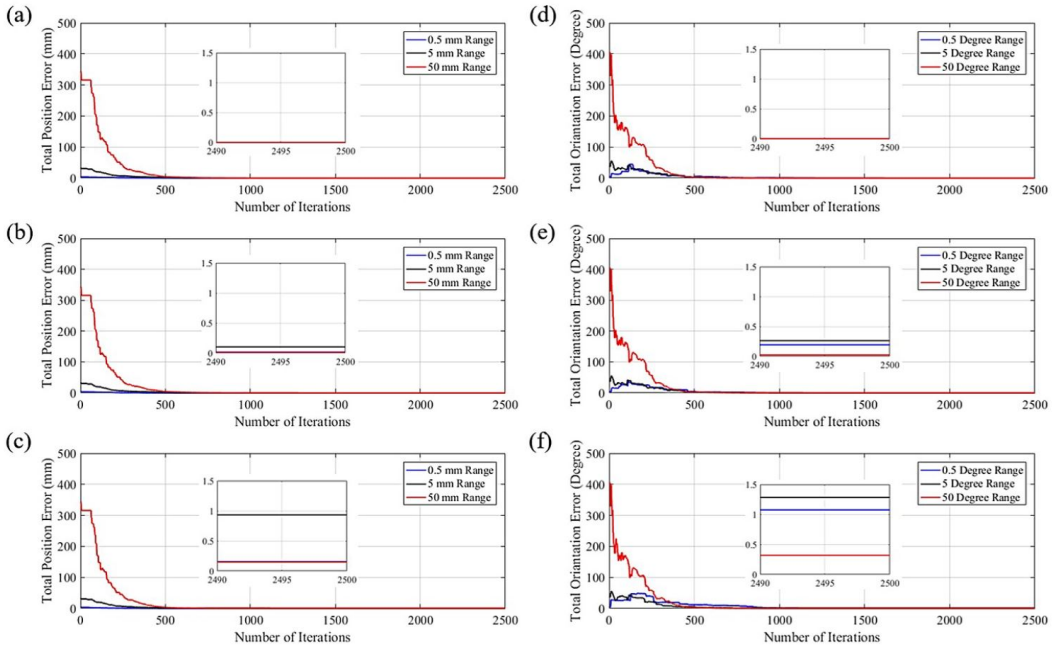

Figure 5.16: The transmitter coils' pose errors change during the calibration process: (a),(d) without noise included, (b),(e) with $-100dBW$ and (c),(f) with $-80dBW$ Gaussian white noise in the measured voltages.

5.6.4 Testing of Kalman Filter Performance

Kalman filter is an optimal estimator for a linear quadratic Gaussian problem caused by system Gaussian noise [Lov11]. It is widely utilized in different tracking systems to increase the tracking accuracy [SMC01, BBF+04, Bla86]. In electromagnetic tracking, when the distance between the sensor and the transmitter coils increase, the jitter errors of sensor positions become larger [HFB+06]. The noises in the estimated sensor pose are typically assumed as Gaussian noise [FHB+14], and therefore Kalman filter can be applied. The equations of Kalman filtering are given by equation 5.9 – 5.13 [WB06a].

$$\widehat{x}_k^- = A\widehat{x}_{k-1}^- + B\mu_k, \tag{5.9}$$

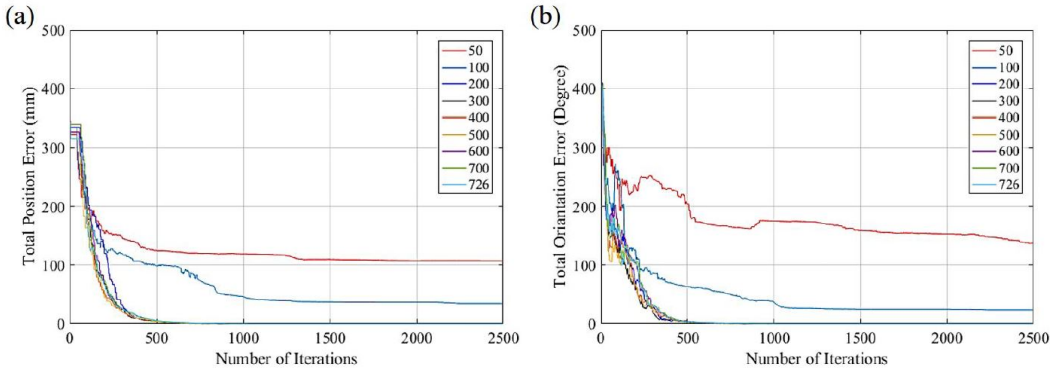

Figure 5.17: The transmitter coils' accumulative (a) position errors and (b) orientation errors change during the calibration process with the number of poses for the calibration algorithm being selected between 50 to 726 with the error range of 50 in mm and ^{o}.

$$P_k^- = AP_{k-1}A^T + Q, \tag{5.10}$$

$$K_k = P_k^- H^T (HP_k^- H^T + R)^{-1}, \tag{5.11}$$

$$\widehat{x}_k = \widehat{x}_k^- + K_k(z_k - H\widehat{x}_k^-), \tag{5.12}$$

$$P_k = (1 - K_k H)P_k^-. \tag{5.13}$$

Equation 5.9 and 5.10 describe the system update state, $\widehat{x}_k^-$ is the project state vector which is presented by (X_{s-p},Y_{s-p},Z_{s-p},Φ_{s-p},Θ_{s-p}) at the step k which can be updated from the last step. A is the state transition matrix which represents changes of the system state. B and μ_k are the control matrix and control vector of the Kalman filter. Herein, for estimated sensor pose, there are no control element and therefore,B and μ_k are considered to be 0. P is the estimated error covariance, and

Q is the process noise covariance. The system measurement update process is shown in equation 5.11 - 5.13. H is the observation matrix and R is the covariance of the measurement error and K is the Kalman gain being used to update the system state vector. z_k is the measurement vector of (X_{s-m},Y_{s-m},Z_{s-m},Φ_{s-m},Θ_{s-m}). For catheter tracking in medical applications, the movement model of constant velocity was proposed [Mar11]. In this case, the system state vector of Kalman filter is defined as $x_k = \begin{pmatrix} X_s, Y_s, Z_s, \Phi_s, \Theta_s \\ \dot{X}_s, \dot{Y}_s, \dot{Z}_s, \dot{\Phi}_s, \dot{\Theta}_s \end{pmatrix}$, including the positional and angular velocity of the moving catheter's tip.

In this experiment, the transmitter coils' arrangement as Figure 5.9 (B) presents was selected. A $-100dBW$ and AGWN was introduced. In order to evaluate the dynamic performance of the Kalman filter, the magnetic sensor was moved in the simulator from $\begin{pmatrix} 0mm \\ 0mm \\ 350mm \end{pmatrix}$ to $\begin{pmatrix} 100mm \\ 200mm \\ 650mm \end{pmatrix}$ at the velocity of $\begin{pmatrix} 1mm/s \\ 2mm/s \\ 3mm/s \end{pmatrix}$, towards X,Y and Z directions. The angular velocity of the sensor coil of $\begin{pmatrix} 1°/s \\ 2°/s \end{pmatrix}$ starting from $\begin{pmatrix} -180° \\ -180° \end{pmatrix}$ to $\begin{pmatrix} -80° \\ 20° \end{pmatrix}$.The sensor movement and the pose estimation is synchronized in the simulator by fixing the sampling rate to be $1Hz$. In total, 100 sensor poses were measured in this experiment. Accordingly, the Kalman filter applying a constant velocity model was selected.

The result of a simple evaluation of the dynamic Kalman filter performance witch is shown in Figure 5.18. The tracking errors increase when the Z distances between sensor and transmitter coils become larger. After applying the Kalman filter, the pose errors were reduced to a much

lower level.

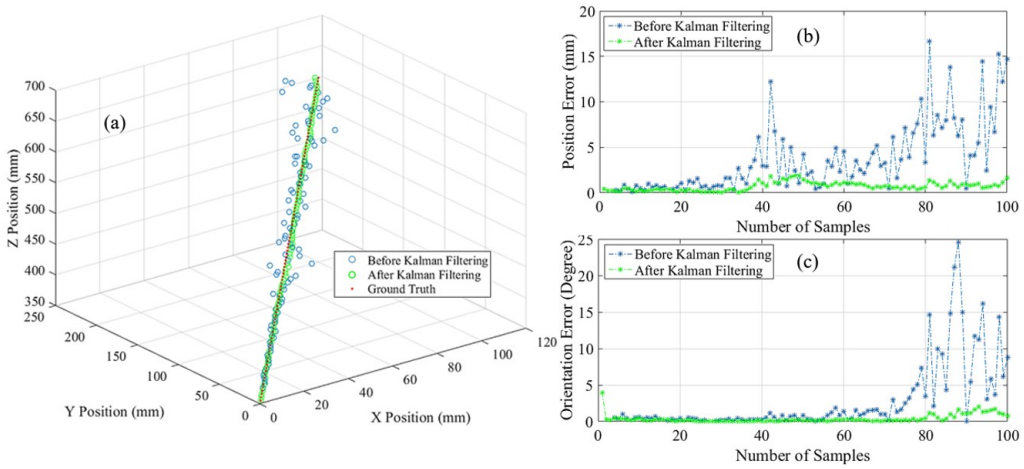

Figure 5.18: The evaluation of the dynamic Kalman Filter performance in EM Tracking. (a) 3D scatter plot of non-filtered, filtered and ground truth of the sensor positions, (b) and (c) present the sensor's position and orientation errors being reduced after applying the Kalman Filter.

As is seen in Figure 5.18 (a), when the sensor coil is moved with a constant linear velocity in position and angular velocity in orientation. The position error increases while the sensor coil is moved towards upper locations. After applying the Kalman filter, the tracking accuracy in both position and orientation increases. Figure 5.18 (b) and 5.18 (c) show the improvement in tracking accuracy by employing Kalman filter. The RMS errors before filtering are $5.28mm$ and 5.51^o, which have been reduced to $0.82mm$ and 0.69^o after being filtered. This test only shows an example of how to test the Kalman filter performance using the developed EMTS simulator. In this scenario, the Kalman filter improved the tracking accuracy. Inorder to see if Kalman filter can increase the tracking accuracy for different scenarios, more tests are needed to be performed.

5.6.5 Testing of Updating Initial Guess of the Pose Estimation Algorithm

The sensor pose estimation algorithm utilizes MATLAB "f–solve" function to searching the optimum of the actual sensor's locations. If the initial guess is far away from the real value, the local minimum which is much different from the global minimum, can be searched. It will negatively influence the tracking accuracy. In the work discussed above, the real values of the sensor pose were utilized as the initial guess for the algorithm in order to minimize the tracking errors caused by the optimization algorithm itself. In this experiment, the accuracy evaluation as is discussed in Section 5.6, using the same constant velocity model, was repeated with the initial guess being selected to be four distinct scenarios: no update, update from the previous measurement value, update the last filtered value applying the Kalman filter and update with the real sensor pose. In this evaluations, firstly no noises signal was added into the measured voltages. This experiment is utilized to examine the influence from changing the initial guess values solely. The result is shown in Figure 5.19.

As is illustrated in Figure 5.19 (a), the initial guess value of the optimization algorithm was fixed to be $\begin{pmatrix} 0mm \\ 0mm \\ 100mm \end{pmatrix}$ and $\begin{pmatrix} 0^\circ \\ 0^\circ \end{pmatrix}$. These values remain unchanged in the whole process of estimating 100 sensor poses. In this scenario, large errors exist. In Figure 5.19 (b), the initial guess value was updated using the estimated sensor pose from the last sample. The tracking accuracy was improved. However, when there is a large error in estimation of the sensor pose, using the wrong value as the initial guess will cause the tracking errors. The following calculations are based on the wrong value from the last calculation. Therefore there are multiple locations where large tracking errors occur. In Figure 5.19

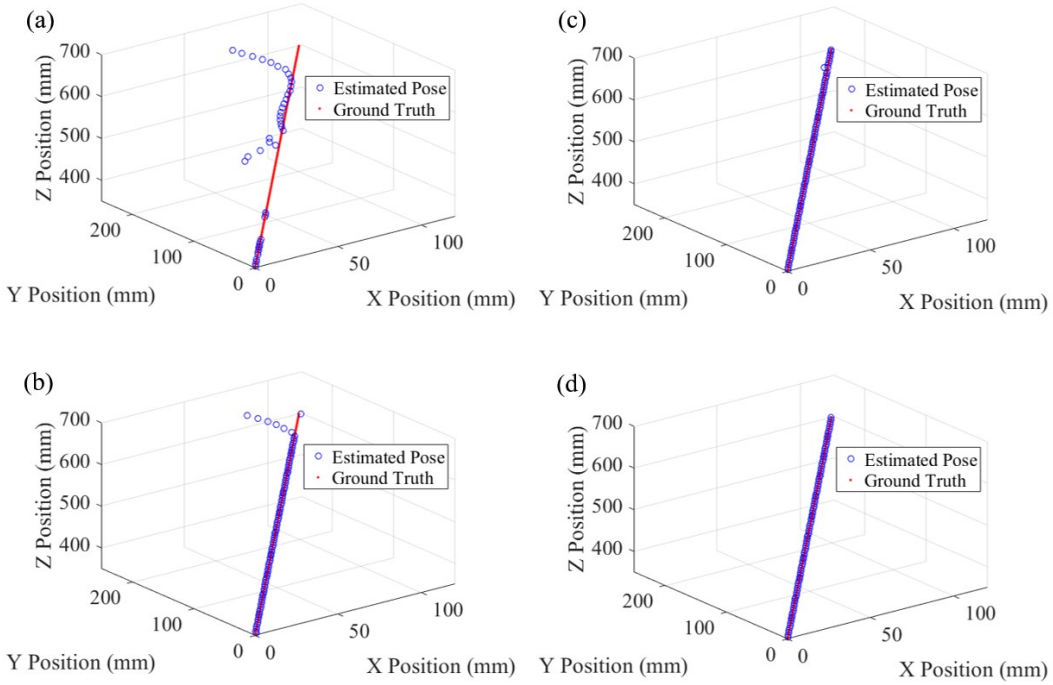

Figure 5.19: The difference between the estimated sensor positions and the ground truth using different values as the initial guess: (a) no update, fixed value, (b) update with the previously estimated sensor pose, (c) update with the filtered sensor pose and (d) update with ground truth.

(c), the value of initial guess was updated with the sensor pose value after being filtered out by Kalman filter. Compared to Figure 5.19 (a) and (b), the tracking accuracy was significantly improved. The reason is that, the Kalman filter estimates the state value based on the previous measurement. When there is one large error in a series of values, based on the previous states, the Kalman filter can reduce the large error to a much lower level. Therefore, the tracking accuracy can be improved by updating the initial guess with the filtered sensor poses. In Figure 5.19 (d), the initial guess values are updated directly with the ground truth of the current sensor pose. It can minimize the tracking errors due to the pose estimation algorithm. Nevertheless, in reality, the ground

truth is never known. Therefore, as is discussed in this chapter, an advanced solution is utilizing the filtered values to update the initial guess values of the pose estimation algorithm, which is promising to increase the tracking accuracy.

5.7 Chapter Discussion

In this chapter, a method of developing a simulator which allows advanced analysis in electromagnetic tracking technology, is presented. In order to simulate the magnetic field generated by the transmitter coils, the magnetic dipole model is selected because it is frequently suggested in the literature for use in electromagnetic tracking technology. The main drawback of the dipole approximation is it cannot be utilized in the regions too close to the dipole [HP06]. Therefore in this work, the VOI for all the experiments were chosen with a minimum Z distance of $50mm$ away from the origin XY plane. It is similar to the realities where generally the field generator is placed in some distance from the VOI for surgical and other applications. The simulator allows the analysis to be conducted in a virtual world where all the unavoidable errors and uncertainties, in reality, can be removed or separately considered.

In the simulator, all the parameters in EM tracking can be adjusted. This work focuses on the analysis of a typical 5-DOF medical EMTS in assisting IGS. Most commercial EMTS utilize a planar field generator [FHB+14], and the arrangement of the transmitter coils are confidential for the manufacturers. In this chapter, the tracking accuracy with all the transmitter coils placed in a planar field generator was compared. The result shows that when the coils are faced in a single orientation, the system has the lowest accuracy. Accuracy is improved by applying multiple coil orientations and further enhanced by the optimized transmitter coil arrangement to get the largest voltages across the sensor coil. Placing the transmitter coils around the VOI improved the tracking accuracy

to a very high level. The optimization of the coil arrangement further improved the tracking accuracy.

The comparison between using the different objective functions for the optimization algorithm is presented in Table 5.3. The results illustrate that choosing the sensor position RMSE as the objective function let the system have an even better accuracy. In the box–area, both of the optimized coil arrangements can be easily applied in reality. However, as was shown in Figure 5.11 (b), the optimized transmitter coils are not symmetric to each other in a 3D VOI, which may add complexities in the construction process. In Figure 5.11 (c), the optimized spatial arrangement of the transmitter coils, by applying the reciprocal of maximum voltage as the objective function for the patterns-search algorithm, can be symmetric to each other with separate upper and lower planes. In practice, the field generators which have the coils fixed with such positions and orientations will not be very complicated to construct. The calibration algorithm to correct the measurement errors of the transmitter coils' poses was evaluated by using the simulator without considering noises, errors of the reference positioning system and other uncertainties from the real world. The results show that the algorithm itself works correctly. In the previous test [BR12], the result was not fully sufficient to prove the method because of errors in the reference positioning systems. The performance of Kalman filtering has also been tested based on the simulator. In this chapter, as an example of introducing how to use the simulator to test the Kalman filter performances in EM tracking, only one movement model was selected. The result shows that applying the Kalman filter is promising to enlarge the actual working volume. However, more systematic evaluations of various movement models need to be performed. The Kalman filter predicts the next state based on the previous measurement. If large errors already exist in the previous state, the Kalman filter cannot improve the tracking accuracy but keeps on predict the wrong sensor's poses. To avoid large tracking errors, here

only Gaussian white noise exists with acceptable amplitude was added into the measured voltages. In the future work, more complex noise models can be selected to perform a systematic analysis to evaluate the performance of Kalman filter in EM tracking. The proposed simulator can also be applied to analyze other system parameters and testing new applications in the scope of electromagnetic tracking, before trying them on a real system setup. It removes all of the uncertainties from the reality and can be applied to speeding up the development of new technologies.

5.8 Chapter Conclusion

Various sources of errors influence the accuracy of electromagnetic tracking systems. A real-world system does not allow the sources of errors to be analyzed individually. Therefore, a software is developed to simulate the entire electromagnetic tracking system. The ground truths of the sensor coils' position and orientation can always be known within the simulator. System parameters such as noise level and transmitter coil poses can also be separately adjusted in the simulator. In this work, the optimization of the transmitter coil arrangement and the comparisons of tracking accuracy according to different transmitter coil poses were performed. The results show that the EMTS is more accurate when the transmitter coils are placed around the VOI in an optimized layout. The results also indicate that the calibration algorithm can perfectly correct the measurement errors of the transmitter coils' poses. Moreover, the Kalman filter is promising to enlarge the working volume of electromagnetic tracking systems. The developed simulator also supports other analysis in general EM tracking.

Chapter 6

Summary and Future Work

As is introduced in Chapter1 1 and Chapter 2, electromagnetic tracking technology has been becoming more widely employed in clinical settings since its invention in 1975 [Kui75]. Although manufacturers have developed several generations of commercially available products, the biggest obstacle preventing the more widespread use of EMTSs their safety in clinical applications still remains due to the unavoidable presence of metallic objects in the OR (including operating tables, surgical instruments, and other devices), which negatively influence the tracking accuracy. Therefore, the motivation of this thesis is to develop a applicable real-time method to reduce the tracking errors caused by the metallic objects. The EMTS prototype for experimental purposes had been developed previously by Bien et al. [BR12]. Different from the previous hardware setup, in this thesis, the FPGA was employed for signal generation and DAQ processes. The FPGA enables parallel execution to be realized.

As discussed in Chapter 3, several methods have been proposed in the literature to reduce the tracking errors caused by metallic distorters. However, these solutions focus primarily on static objects or are too slow for real-time applications. Therefore, a novel method based on using ramp excitation and measuring the system's steady-state response

(as introduced in Section 3.4 – 3.7) was developed in this thesis in order to achieve the real-time requirement. Systematic evaluations have been performed to assess the tracking accuracy, refresh rate, system latency, and the goal of reducing the dynamic distortions caused by the metallic objects located in proximity to the EM sensor. The results in Section 3.7 showed that the system prototype that applied the ramp-excitation method featured a refresh rate of $12.7Hz$. Although the system's mean latency was measured to be $431ms$, the moving-average-like data acquisition smooths the tracking processes. The implementation of the ramp–excitation method in the current prototype is sufficiently accurate in a relatively small working volume, i.e. with the distance between the sensor and the center of the transmitter coils smaller than $120mm$, thereby reducing the tracking errors caused by the metallic distorters to a very low level. Potential solutions that further increase tracking speed and accuracy, which were discussed in Section 3.9, require future studies. The proposed ramp–excitation method only reduce the sources of distortions caused non-ferromagnetic metals, e.g. aluminum and authentic stainless steel etc. Although such materials are frequently applied for clinical applications, ferromagnetic materials could still exist which cannot be ignored. For the real medical applications, the type of metallic materials around the SROI should still be noted.

The system hardware implementation was introduced in Chapter 4. The FPGA was utilized for signal generation and data acquisition. The TDM, FDM and the improved TDM method were discussed. The FDM and the improved TDM method largely increase the tracking speed. Due to the hardware limitations of the prototype, at least a 5-period averaging is needed. By further improving the system hardware, such as the amplifier circuits and the geometry of the transmitter coils, etc. , fewer periods for averaging will be needed. Therefore, the tracking speed, as well as the accuracy are promising to be improved. The current algorithm for sensor pose estimation are implemented in *MATALB*, the execution

time, especially the iterative optimization steps run slowly in the scripting programming language. This thesis focuses on proving the proposed methods based on the constructed EMTS prototype. The prototype is slower and less accurate than the commercial system. However, it has much better performances in minimizing the tracking errors caused by the proximate electrically conductive distortions.

In order to analyze the system's theoretical performance without considering electrical noises or other uncertainties, a simulation software was developed (as discussed in Chapter 5). In Subsection 5.6.2, an algorithm to select the optimized spatial placement of the transmitter coils was introduced. By optimizing the coils' placement, the tracking accuracy was significantly improved over the application of a random distribution of transmitter coils. The performance of the implemented calibration algorithm and the performance of Kalman Filter was also assessed using the developed EMTS simulator. Moreover, different initial guess values for the sensor pose estimation algorithm has been tested. The results documented in Subsection 5.6.5 showed that using the filtered sensor pose as the initial guess further improved tracking accuracy. The developed EMTS allows all the system parameters to be separately analyzed which is not possible for the real system setup. However, the drawbacks of the simulator are, that it is a model-based tool software. The testing results rely on the models being applied. In this thesis, for simulating the noise signals in the measured voltages, only additive Gaussian white noise model was considered. In the future, more sophisticated noise models could be applied. Evaluations of the optimized transmitter coils' arrangement should also be tested by on a real system setup. A simple constant velocity model which simulates the catheter movement was applied to access the implemented Kalman filter. Although the result is very promising, in the future, more complex movement models should be applied to evaluate the Kalman filter's performances systematically.

Appendix A

Documentation of Designed Simulator

A.1 The GUI Design

As is introduced in Chapter 5, in this thesis a software to simulate the entire EMTS for testing its theoretical performance was developed. Accordingly, a graphic-user interface has been designed to let the end user easily understand and control the simulator without solid programming skills.

The designed GUI is presented by Figure A.1. the EMTS simulator allows the user to adjust the parameters and placement of each transmitter coil manually as well as the sensor coil. The parameters of the coils are mechanically prefixed values, consequently, for the simulation work within this thesis, they have remained unaltered. The shift can be added to each transmitter coil to perform systematic analyses the influences in sensor pose estimation due to the inaccurate measurement of the transmitter coils positions and orientations. Figure A.2 presents the shift of the transmitter coils' poses adjusted in the simulator and the real poses of the transmitter coils, which was discussed in Section 5.6.3.

Different level of noise signals can be added to or wholly removed from the measured voltages induced in the sensor coil by pressing the

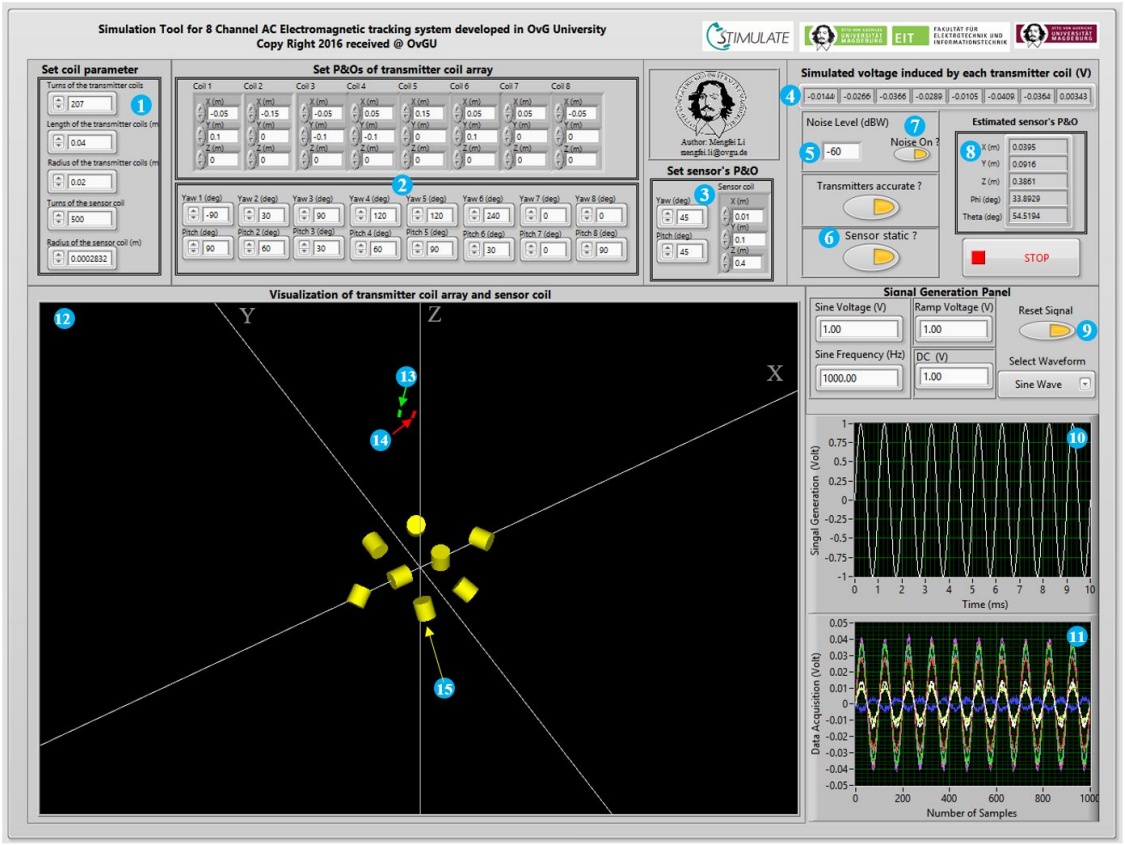

Figure A.1: The GUI of the designed EMTS Simulator. (1) Define parameters of the transmitter coils and the sensor coil. (2) Define position and orientation of the transmitter coils. (3) Define position and orientation of the sensor coil. (4) "Measured" voltage induced by each transmitter coil. (5) Add noise to voltage measurement. (6) Change the sensor coil's state between stationary and mobile. (7) Select if there are pose errors in the transmitter coils. (8) The estimated sensor pose. (9) Signal generation and data acquisition control. (10) Visualization of the generated waveform signal. (11) Visualization of the measured voltage signals. (12) Visualization panel of the sensor and transmitter coils: (13) real sensor's pose, (14) estimated sensor's pose. (15) The poses of eight transmitter coils.

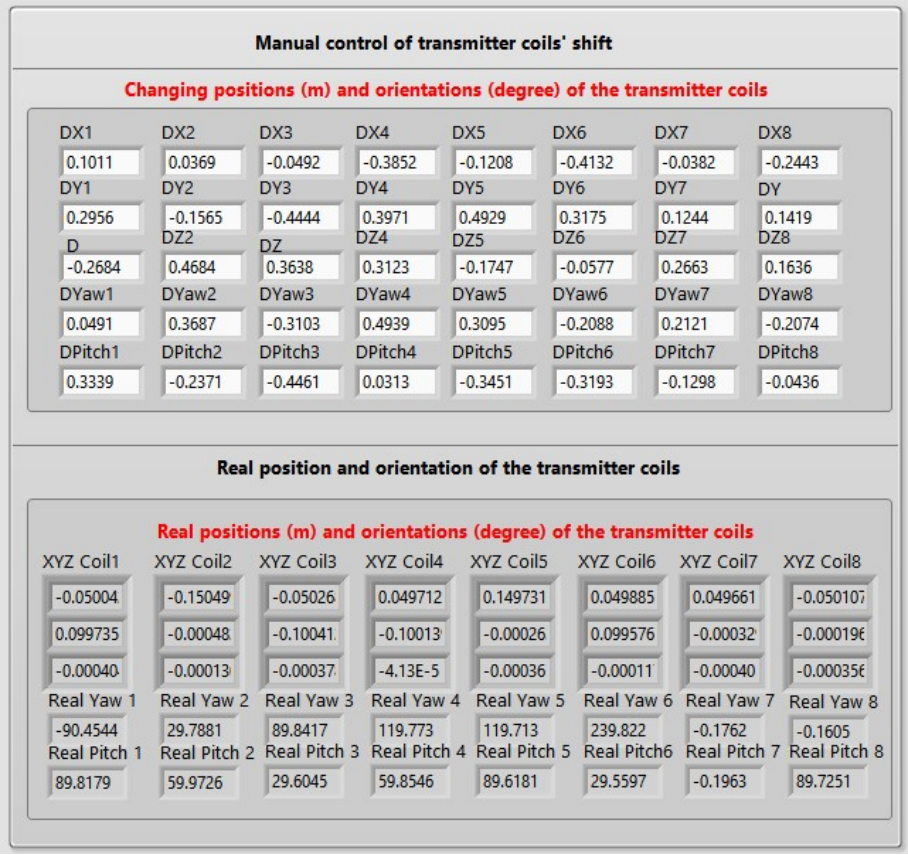

Figure A.2: The adjustment of the transmitter coils' shift.

"Noise On" button. All of the error sources which adds inaccuracy in the estimated sensor pose can be separately taken into consideration.

The sensor coil can either remain stationary or moved with the predefined trajectories, controlled by pressing the "Sensor Static" button. In the simulator, the sensor coil can be moved continuously for evaluation of the tracking velocity errors or discretely moved to multiple locations to perform calibration and tracking accuracy assessment. Parameters for sampling such as sampling frequency and the number of samples to be measured were assigned with standard values as $100kHz$ and 1000 samples per channel, respectively. For the signal generation, waveform

shapes among sine, ramp, quadratic and unit step functions can be chosen. Amplitude and frequency of the generated waveform signals are manually be defined. The visualizations of the waveform signals and the 3D poses of the coils help the users to understand of the whole system setup intuitively.

A.2 Quick Start Guide

The developed simulation tool is a open-source software and available on *GitHub* (Link: https://github.com/RandLive/EMTS_SIMULATOR). In this section, a quick–start manual of the software is introduced.

1. In this simulation software, mostly, LabVIEW is utilized to design the GUI, and MATLAB is used to run computations. Therefore, both of the MATLAB(Version 2014+) and LabVIEW (Version 2014+) should be installed to ensure the software running environment. Moreover, the MATLAB Optimization toolbox is also required for the algorithm of sensor position and orientation estimation.

2. Copy the "MATLAB_Source" folder to the "C:\" root directory of the PC.

3. Open the "LabVIEW_Source" folder, and start "EMTS_Simulator-_Main .lvproj" Project.

4. Start the LabVIEW file "EMTS_Simulator_2017_Main_V1.vi" which is the main program of the simulator.

5. Double click the control element on the GUI or press "CTRL+E" button to edit the background code and make necessary changes according to the specific testing purpose.

6. The simulated data can be visualized in real-time and be saved as the ".txt" file for offline analysis using MATLAB or other relevant software.

A.3 Optimization of the Transmitter Coils Arrangement

As is discussed in Section 5.6.2, the transmitter coils' spatial arrangement is optimized using Equation 5.5 and 5.7 as the objective function for the global patternsearch algorithm using MATLAB. The implementation of the method is located on https://github.com/RandLive/Opti_Trans_PO.

The files "Main_Opti_MaxVoltage_Box.m" and "Main_Opti_MinPoseError- _Box.m" are the programs for optimizing the coils' arrangement in a box-shape volume as presented in Figure 5.11 (a) and 5.11 (b) using Equation 5.5 and 5.7.

The files "Main_Opti_MaxVoltage_VOI.m" and "Main_Opti_MinPoseError_VOI.m" are the programs for optimizing the coils' arrangement in a VOI around the testing volume as presented in Figure 5.11 (c) and 5.11 (d) using Equation 5.5 and 5.7 respectively.

Other relevant software developed for the evaluations using the simulator were also appeared on *Github* under the username- *RandLive*: https://github.com/RandLive.

Acknowledgement

This work was conducted at Institut für Medizintechnik, Otto–von–Guericke Universität Magdeburg. I am grateful to thank the people who have been involved and contributed to the research project. Firstly, I express my deepest admiration for my doctoral supervisor Prof. Dr. Georg Rose for giving me such a great opportunity to work within this impressive field as a Ph.D. student. In this five–year research period, I have gotten a very comprehensive direction and great helpful suggestions from him, without that I cannot fulfill the scopes in this project and go this far. Secondly, I also want to thank Jun.Prof. Dr. Christian Hansen for supporting me in working in the group of Computer Assisted Surgery. Wherein, I have experienced a plenty of novel technologies in the field of clinical navigation and that strengthened my research. I also want to thank Dr. Tomasz Bien who guided me at the beginning when I was firstly entering the world of electromagnetic tracking. As well, also many thanks to all of my kind colleagues with whom I have spent an incredible time with for all of these years. Moreover, I want to thank Dr. Johannes Krug, who kindly shared his experiences in scientific writing with me and gave me a lot of constructive suggestions in formatting this dissertation. I have to thank my wife Shixing, who is always being accompanied with me, sharing with my success and failure, happiness and sorrow. I cannot go through all these without her.

Bibliography

[And07] Peter Traneus Anderson. Electric motor tracking system and method, September 10 2007. US Patent App. 11/852,597.

[And10] Peter Traneus Anderson. Ultra-low frequency electromagnetic tracking system, July 20 2010. US Patent 7,761,100.

[BBF+04] M. Bertozzi, a. Broggi, a. Fascioli, a. Tibaldi, R. Chapuis, and F. Chausse. Pedestrian localization and tracking system with Kalman filtering. *IEEE Intelligent Vehicles Symposium, 2004*, pages 584–589, 2004.

[BE96] B. D. Adelstein, E. R. Johnston, S. R. Ellis and S. R. Ellis. Dynamic response of electromagnetic spatial displacement trackers. *Presence*, 5(3):302–318, 1996.

[BHKS09] Richard W Bohannon, Steven Harrison, and Jeffrey Kinsella-Shaw. Reliability and validity of pendulum test measures of spasticity obtained with the polhemus tracking system from patients with chronic stroke. *Journal of neuroengineering and rehabilitation*, 6(1):30, 2009.

[BHWC08] Wolfgang Birkfellner, Johann Hummel, Emmanuel Wilson, and Kevin Cleary. Tracking devices. In *Image-Guided Interventions*, pages 23–44. Springer, 2008.

[Bla86] Samuel S Blackman. Multiple-target tracking with radar applications. *Dedham, MA, Artech House, Inc., 1986, 463 p.*, 1986.

[BLR13] T. Bien, Mengfei. Li, and Georg. Rose. Distortion-immune electromagnetic tracking system: A new approach using quadratic excitation. *Cars*, 2013.

[BLSR14] Tomasz Bien, Mengfei Li, Zein Salah, and Georg Rose. Electromagnetic tracking system with reduced distortion using quadratic excitation. *International Journal of Computer Assisted Radiology and Surgery*, 9(2):323–332, mar 2014.

[BPN+09] Philipp Bruners, Tobias Penzkofer, Markus Nagel, Robert Elfring, Nina Gronloh, Thomas Schmitz-Rode, Rolf W Günther, and Andreas H Mahnken. Electromagnetic tracking for ct-guided spine interventions: phantom, ex-vivo and in-vivo results. *European radiology*, 19(4):990–994, 2009.

[BR12] Tomasz Bien and Georg Rose. Algorithm for calibration of the electromagnetic tracking system. *Proceedings - IEEE-EMBS International Conference on Biomedical and Health Informatics: Global Grand Challenge of Health Informatics, BHI 2012*, pages 85–88, jan 2012.

[Bra07] Brandon Wicks. DDS WaveForm Generator, 2007.

[BRF+15] Samir Boutaleb, Emmanuel Racine, Olivier Fillion, Antonio Bonillas, Gilion Hautvast, Dirk Binnekamp, and Luc Beaulieu. Performance and suitability assessment of a real-time 3D electromagnetic needle tracking system for interstitial brachytherapy. *Journal of Contemporary Brachytherapy*, 7(4):280–289, aug 2015.

[BWW+98] W Birkfellner, F Watzinger, F Wanschitz, G Enislidis, C Kollmann, D Rafolt, R Nowotny, R Ewers, and H Bergmann. Systematic distortions in magnetic position digitizers. *Medical Physics*, 25(11):2242, nov 1998.

[CP10] Kevin Cleary and Terry M Peters. Image-guided interventions: technology review and clinical applications. *Annual review of biomedical engineering*, 12:119–142, 2010.

[DDSR95] Charles L Dumoulin, Robert D Darrow, John F Schenck, and Peter B Roemer. Tracking system to follow the position and orientation of a device with radiofrequency fields, January 3 1995. US Patent 5,377,678.

[Doe74] Gustav Doetsch. *Introduction to the Theory and Application ofthe of the Laplace Transformation*. Springer Berlin Heidelberg, Berlin, Heidelberg, 1974.

[Dum01] Charles Lucian Dumoulin. Error compensation for device tracking systems employing electromagnetic fields, March 13 2001. US Patent 6,201,987.

[EST+04a] Rolf Ewers, Kurt Schicho, Michael Truppe, Rudolf Seemann, Astrid Reichwein, Michael Figl, and Arne Wagner. Computer-Aided Navigation in Dental Implantology: 7 Years of Clinical Experience. *Journal of Oral and Maxillofacial Surgery*, 62(3):329–334, mar 2004.

[EST+04b] Rolf Ewers, Kurt Schicho, Michael Truppe, Rudolf Seemann, Astrid Reichwein, Michael Figl, and Arne Wagner. Computer-Aided Navigation in Dental Implantology: 7 Years of Clinical Experience. *Journal of Oral and Maxillofacial Surgery*, 62(3):329–334, mar 2004.

[FHB+14] Alfred M Franz, Tamas Haidegger, Wolfgang Birkfellner, Kevin Cleary, Terry M Peters, and Lena Maier-Hein. Electromagnetic tracking in medicine—a review of technology, validation, and applications. *IEEE transactions on medical imaging*, 33(8):1702–1725, 2014.

[FKG+97] M P Fried, J Kleefield, H Gopal, E Reardon, B T Ho, and F a Kuhn. Image-guided endoscopic surgery: results of accuracy and performance in a multicenter clinical study using an electromagnetic tracking system. *The Laryngoscope*, 107(5):594–601, may 1997.

[Fre04] Herbert L Fred. Drawbacks and limitations of computed tomography: views from a medical educator. *Texas Heart Institute journal / from the Texas Heart Institute of St. Luke's Episcopal Hospital, Texas Children's Hospital*, 31(4):345–348, jan 2004.

[FWLK03] D D Frantz, a D Wiles, S E Leis, and S R Kirsch. Accuracy assessment protocols for electromagnetic tracking systems. *Physics in medicine and biology*, 48(14):2241–2251, jul 2003.

[FWM98] J M Fitzpatrick, J B West, and C R Maurer. Predicting error in rigid-body point-based registration. *IEEE transactions on medical imaging*, 17(5):694–702, 1998.

[G+07] LEGO Group et al. Company profile: An introduction to the lego group 2007. *URL (accessed 22 October 2007): http://cache. lego. com/downloads/aboutus/LEGO_ company_ profile_ UK. pdf*, 2007.

[GCJ88] P. Garikepati, T. T. Chang, and D. C. Jiles. Theory of ferromagnetic hysteresis: Evaluation of stress from hysteresis curves. *IEEE Transactions on Magnetics*, 24(6):2922–2924, 1988.

[Glo09] Neil D Glossop. Advantages of optical compared with electromagnetic tracking. *The Journal of Bone and Joint Surgery*, 91(Supplement 1):23–28, 2009.

[Gov02] Assaf Govari. Electromagnetic position single axis system, November 19 2002. US Patent 6,484,118.

[Haj10] Ali Hajimiri. Generalized time-and transfer-constant circuit analysis. *IEEE Transactions on Circuits and Systems I: Regular Papers*, 57(6):1105–1121, jun 2010.

[Han86] Per K Hansen. Magnetic position and orientation measurement system, November 11 1986. US Patent 4,622,644.

[HFB+06] J Hummel, M Figl, W Birkfellner, M R Bax, R Shahidi, C R Maurer, and H Bergmann. Evaluation of a new electromagnetic tracking system using a standardized assessment protocol. *Physics in medicine and biology*, 51(10):N205–N210, may 2006.

[HP06] P. G. Harris and J. M. Pendlebury. Dipole-field contributions to geometric-phase-induced false electric-dipole-moment signals for particles in traps. *Physical Review A - Atomic, Molecular, and Optical Physics*, 73(1):014101, jan 2006.

[HSW+12] Chao Hu, Shuang Song, Xiaojing Wang, Max Q H Meng, and Baopu Li. A novel positioning and orientation system based on three-axis magnetic coils. *IEEE Transactions on Magnetics*, 48(7):2211–2219, jul 2012.

[IBHH01] M. Ikits, J.D. Brederson, C.D. Hansen, and J.M. Hollerbach. An improved calibration framework for electromagnetic tracking devices. *Proceedings IEEE Virtual Reality 2001*, pages 63–70, 2001.

[Joh63] Walter C Johnson. Transmission lines and networks. *McGraw-Hill Electrical and Electronical Engineering Series, Auckland: McGraw-Hill, 1963*, 1:58, 1963.

[JSKS03] Bradley Jascob, David Simon, Paul Kessman, and Aaron Smith. Method and apparatus for electromagnetic navigation of a surgical probe near a metal object, October 21 2003. US Patent 6,636,757.

[KCB+03] P. W. Kuchel, B. E. Chapman, W. A. Bubb, P. E. Hansen, C. J. Durrant, and M. P. Hertzberg. Magnetic susceptibility: Solutions, emulsions, and cells. *Concepts in Magnetic Resonance Part A: Bridging Education and Research*, 18(1):56–71, apr 2003.

[Kin99] V. Kindratenko. Calibration of electromagnetic tracking devices. *Virtual Reality*, 4(2):139–150, jun 1999.

[Kin00] Volodymyr V. Kindratenko. A survey of electromagnetic position tracker calibration techniques. *Virtual Reality*, 5(3):169–182, sep 2000.

[KKK13] Tapani Koivukangas, Jani Pa Katisko, and John P Koivukangas. Technical accuracy of optical and the electromagnetic tracking systems. *SpringerPlus*, 2(1):90, dec 2013.

[KNTO11] Andreas Krauss, Simeon Nill, Martin Tacke, and Uwe Oelfke. Electromagnetic real-time tumor position monitoring and dynamic multileaf collimator tracking using a siemens 160 mlc: Geometric and dosimetric accuracy of an integrated system. *International Journal of Radiation Oncology* Biology* Physics*, 79(2):579–587, 2011.

[Kui75] Jack Kuipers. Object tracking and orientation determination means, system and process, February 25 1975. US Patent 3,868,565.

[KWVH03] C. L. Koerhuis, J. C. Winters, F. C T Van der Helm, and A. L. Hof. Neck mobility measurement by means of the 'Flock of Birds' electromagnetic tracking system. *Clinical Biomechanics*, 18(1):14–18, jan 2003.

[KXG+07] Jochen Krücker, Sheng Xu, Neil Glossop, Anand Viswanathan, Jörn Borgert, Heinrich Schulz, and Bradford J Wood. Electromagnetic tracking for thermal ablation and biopsy guidance: clinical evaluation of spatial accuracy. *Journal of Vascular and Interventional Radiology*, 18(9):1141–1150, 2007.

[LAH03] Suzanne LaScalza, Jane Arico, and Richard Hughes. Effect of metal and sampling rate on accuracy of Flock of Birds electromagnetic tracking system. *Journal of Biomechanics*, 36(1):141–144, jan 2003.

[LBR13] Mengfei Li, Tomasz Bien, and Georg Rose. Fpga based electromagnetic tracking system for fast catheter navigation. *Int J Sci Eng Res*, 4(9):2566–2570, 2013.

[LBR14] Mengfei Li, Tomasz Bien, and Georg Rose. Construction of a conductive distortion reduced electromagnetic tracking system for computer assisted image-guided interventions. *Medical Engineering and Physics*, 36(11):1496–1501, nov 2014.

[Lei12] Leigh. *Control Theory: A guided tour*. Institution of Engineering and Technology, jan 2012.

[LHR15] Mengfei Li, Christian. Hansen, and Georg. Rose. A robust electromagnetic tracking system for clinical applications. *Curac*, pages 31–36, 2015.

[LHR17] Mengfei Li, Christian Hansen, and Georg Rose. A software solution to dynamically reduce metallic distortions of electromagnetic tracking systems for image-guided surgery. *International Journal of Computer Assisted Radiology and Surgery*, pages 1–13, mar 2017.

[Lov11] Miodrag Lovric. *International Encyclopedia of Statistical Science*, volume Part 9. Springer Berlin Heidelberg, 2011.

[LSH+10] Mao Li, Shuang Song, Chao Hu, Dongmei Chen, and Max Q H Meng. A novel method of 6-DoF electromagnetic navigation system for surgical robot. *Proceedings of the World Congress on Intelligent Control and Automation (WCICA)*, pages 2163–2167, jul 2010.

[LSP+15] Elodie Lugez, Hossein Sadjadi, David R. Pichora, Randy E. Ellis, Selim G. Akl, and Gabor Fichtinger. Electromagnetic tracking in surgical and interventional environments: usability study. *International Journal of Computer Assisted Radiology and Surgery*, 10(3):253–262, mar 2015.

[Mar11] Klaus Dietmayer Marcel Schenderlein, Volker Rasche. *Three-Dimensional Catheter Tip Tracking from Asynchronous Biplane X-Ray Image Sequences using Non-Linear State Filtering - Bildverarbeitung für die Medizin 2011*. Informatik aktuell. Springer Berlin Heidelberg, Berlin, Heidelberg, 2011.

[Mea02] Russell L. Meade. *Foundations of Electronics*. Cengage Learning, 2002.

[Muc08] Julian Much. Error Classification and Propagation for Electromagnetic Tracking. *Dissertation*, 2008.

[Nar09] Roger Narayan. *Biomedical materials*. Springer Science & Business Media, 2009.

[Nav05] Carl R. Nave. Inductance of a coil. *HyperPhysics*, 2005.

[NB04] Gregory a Newman and Paul T Boggs. Solution accelerators for large-scale three-dimensional electromagnetic inverse problems. *Inverse Problems*, 20(6):S151–S170, dec 2004.

[NHP+07] Markus Nagel, Martin Hoheisel, Ralf Petzold, Willi A. Kalender, and Ulrich H. W. Krause. Needle and catheter navigation using electromagnetic tracking for computer-assisted c-arm ct interventions. *Medical Imaging*, pages 65090J–65090J.9, mar 2007.

[Nii03] Mitsuo Niinomi. Recent research and development in titanium alloys for biomedical applications and healthcare goods. *Science and Technology of Advanced Materials*, 4(5):445–454, jan 2003.

[NJBA06a] Christopher Nafis, Vern Jensen, Lee Beauregard, and Peter Anderson. Method for estimating dynamic em tracking accuracy of surgical navigation tools. *Proc. SPIE Medical Imag. 2006: Visualizat., Image-Guided Procedures, Display*, 6141:61410K, 2006.

[NJBA06b] Christopher Nafis, Vern Jensen, Lee Beauregard, and Peter Anderson. Method for estimating dynamic EM tracking accuracy of Surgical Navigation Tools. *Proc. SPIE Med. Imag. Visualizat., Image-Guided Procedures Model*, 6141:152–167, mar 2006.

[NJvJ08] Christopher Nafis, Vern Jensen, and Ron von Jako. Method for evaluating compatibility of commercial Electromagnetic (EM) micro sensor tracking systems with surgical and imaging tables. *Proc SPIE*, 6918:691820–691820–15, mar 2008.

[NK08] John M Nieminen and Stefan R Kirsch. Eddy current detection and compensation, April 1 2008. US Patent 7,353,125.

[OCM15] Kilian O'Donoghue and Padraig Cantillon-Murphy. Planar Magnetic Shielding for Use With Electromagnetic Tracking Systems. *IEEE Transactions on Magnetics*, 51(2):1–12, feb 2015.

[OEG+14] Kilian O'Donoghue, David Eustace, James Griffiths, Michael O'Shea, Timothy Power, Hilary Mansfield, and Padraig Cantillon-Murphy. Catheter position tracking system using planar magnetics and closed loop current control. *IEEE Transactions on Magnetics*, 50(7):1–9, jul 2014.

[PA02] François Poulin and L. P. Amiot. Interference during the use of an electromagnetic tracking system under OR conditions. *Journal of Biomechanics*, 35(6):733–737, jun 2002.

[PBI+09] Tobias Penzkofer, P. Bruners, P. Isfort, R. Elfring, A. Fritschi, F. Van Roost, M. Hormes, R. W. Günther, T. Schmitz-Rode, and A. H. Mahnken. Vascular electromagnetic tracking: Experiences in phantom and animal cadaveric models. *IFMBE Proceedings*, 25(6):232–234, 2009.

[PC08a] Terry Peters and Kevin Cleary. Image-guided interventions: Technology and applications. *Image-Guided Interventions: Technology and Applications*, pages 23–36, 2008.

[PC08b] Terry Peters and Kevin Cleary. *Image-guided interventions: technology and applications*. Springer Science & Business Media, 2008.

[PGMH05] Zhang P., J. Gu J. Gu, E.E. Milios E.E. Milios, and P. Huynh P. Huynh. Navigation with IMU/GPS/digital compass with unscented Kalman filter. *IEEE International Conference Mechatronics and Automation, 2005*, 3(July):1497–1502, 2005.

[PKHP08] Anton Plotkin, Vladimir Kucher, Yoram Horen, and Eugene Paperno. A new calibration procedure for magnetic tracking systems. *IEEE Transactions on Magnetics*, 44(11 PART 2):4525–4528, nov 2008.

[PP03] Anton Plotkin and Eugene Paperno. 3-D Magnetic Tracking of a Single Subminiature Coil with a Large 2-D Array of Uniaxial Transmitters. *IEEE Transactions on Magnetics*, 39(5 II):3295–3297, sep 2003.

[PSL01] Eugene Paperno, Ichiro Sasada, and Eduard Leonovich. A new method for magnetic position and orientation tracking. *IEEE Transactions on Magnetics*, 37(4 I):1938–1940, jul 2001.

[PSPK10] Anton Plotkin, Oren Shafrir, Eugene Paperno, and Daniel M. Kaplan. Magnetic eye tracking: A new approach employing a planar transmitter.

IEEE Transactions on Biomedical Engineering, 57(5):1209–1215, may 2010.

[RA11] Taher Rabizadeh and Saeed Reza Allahkaram. Corrosion resistance enhancement of Ni-P electroless coatings by incorporation of nano-SiO2 particles. *Materials and Design*, 32(1):133–138, 2011.

[RBSJ79] Fredereick H. Raab, Ernest B. Blood, Terry O. Steinder, and Herbert R. Jones. Magnetic Position and Orientation Tracking System. *IEEE Transactions on Aerospace and Electronic Systems*, AES-15(5):709–718, sep 1979.

[RGN13] Tobias Reichl, José Gardiazabal, and Nassir Navab. Electromagnetic servoing - A new tracking paradigm. *IEEE Transactions on Medical Imaging*, 32(8):1526–1535, aug 2013.

[Ros08] E. B. Rosa. The self and mutual-inductances of linear conductors. *Bulletin of the Bureau of Standards*, 4(2):301, 1908.

[Row96] Sam Roweis. Levenberg-Marquardt Optimization. *Notes, University Of Toronto*, 1996.

[RTL+02] P Reittner, M Tillich, W Luxenberger, R Weinke, K Preidler, W Köle, H Stammberger, and D Szolar. Multislice CT-image-guided endoscopic sinus surgery using an electromagnetic tracking system. *European radiology*, 12(3):592–6, mar 2002.

[Sch01] Mark Schneider. Distortion immune magnetic field generator for magnetic tracking systems and method of generating magnetic fields, March 15 2001. US Patent App. 09/809,523.

[SCK+10] Faustin Stevens, Michael A. Conditt, Nikhil Kulkarni, Sabir K. Ismaily, Philip C. Noble, and David R. Lionberger. Minimizing electromagnetic interference from surgical instruments on electromagnetic surgical navigation. *Clinical Orthopaedics and Related Research*, 468(8):2244–2250, aug 2010.

[SE01] Gera M Strommer and Uzi Eichler. Medical positioning system, May 15 2001. US Patent 6,233,476.

[SFD+05a] K Schicho, M Figl, M Donat, W Birkfellner, R Seemann, A Wagner, H Bergmann, and R Ewers. Stability of miniature electromagnetic tracking systems. *Phys Med Biol*, 50(9):2089–2098, may 2005.

[SFD+05b] Kurt Schicho, Michael Figl, Markus Donat, Wolfgang Birkfellner, Rudolf Seemann, Arne Wagner, Helmar Bergmann, and Rolf Ewers. Stability of miniature electromagnetic tracking systems. *Physics in medicine and biology*, 50(9):2089, 2005.

[SHA+16] Hanne Sorger, Erlend Fagertun Hofstad, Tore Amundsen, Thomas Lang, and Hakon Olav Leira. A novel platform for electromagnetic navigated ultrasound bronchoscopy (EBUS). *International Journal of Computer Assisted Radiology and Surgery*, 11(8):1431–1443, aug 2016.

[SHL+13a] Shuang Song, Chao Hu, Baopu Li, Xiaoxiao Li, and Max Q H Meng. An electromagnetic localization and orientation method based on rotating magnetic dipole. *IEEE Transactions on Magnetics*, 49(3):1274–1277, mar 2013.

[SHL+13b] Shuang Song, Chao Hu, Baopu Li, Xiaoxiao Li, and MQ-H Meng. An electromagnetic localization and orientation method based on rotating magnetic dipole. *IEEE Transactions on Magnetics*, 49(3):1274–1277, 2013.

[SHOM15] Navid Shahriari, Edsko Hekman, Matthijs Oudkerk, and Sarthak Misra. Design and evaluation of a computed tomography (CT)-compatible needle insertion device using an electromagnetic tracking system and CT images. *International Journal of Computer Assisted Radiology and Surgery*, 10(11):1845–1852, nov 2015.

[SHZF16] Hossein Sadjadi, Keyvan Hashtrudi-Zaad, and Gabor Fichtinger. Simultaneous electromagnetic tracking and calibration for dynamic field distortion compensation. *Crop and Pasture Science*, 63(8):1771–1781, aug 2016.

[SLPD07] Jason T. Sherman, Jonathan K. Lubkert, Radivoje S. Popovic, and Mark R. Disilvestro. Characterization of a novel magnetic tracking system. *IEEE Transactions on Magnetics*, 43(6):2725–2727, jun 2007.

[SMC01] B Stenger, P.R.S. Mendonça, and R Cipolla. Model-based hand tracking using an unscented kalman filter. *Proc. British Machine Vision Conference*, 1:63–72, 2001.

[SMH+08] Lakshmi Santanam, Kathleen Malinowski, James Hubenshmidt, Steve Dimmer, Martin L. Mayse, Jeffrey Bradley, Amir Chaudhari, Kirsten Lechleiter, Sree Krishna Murty Goddu, Jacqueline Esthappan, Sasa Mutic, Daniel A. Low, and Parag Parikh. Fiducial-Based Translational Localization Accuracy of Electromagnetic Tracking System and On-Board Kilovoltage Imaging System. *International Journal of Radiation Oncology Biology Physics*, 70(3):892–899, mar 2008.

[SS07] Mark Schneider and Charles Stevens. Development and testing of a new magnetic-tracking device for image guidance. In *Medical Imaging*, pages 65090I–65090I. International Society for Optics and Photonics, 2007.

[TIU+07] C. Tercero, S. Ikeda, T. Uchiyama, T. Fukuda, F. Arai, Y. Okada, Y. Ono, R. Hattori, T. Yamamoto, M. Negoro, and I. Takahashi. Autonomous catheter insertion system using magnetic motion capture sensor for endovascular surgery. *International Journal of Medical Robotics and Computer Assisted Surgery*, 3(1):52–58, mar 2007.

[Uti13] D D S Memory Utilization. Understanding Direct Digital Synthesis (DDS), 2013.

[WB06a] Greg Welch and Gary Bishop. An Introduction to the Kalman Filter. *In Practice*, 7(1):1–16, 2006.

[WB06b] Greg Welch and Gary Bishop. An introduction to the kalman filter. department of computer science, university of north carolina. *ed: Chapel Hill, NC, unpublished manuscript*, 2006.

[WB10] Jr. William H. hayt and John A. Buck. Engineering Electromagnetics. *Journal of Chemical Information and Modeling*, page 614, 2010.

[WBW+99] F. Watzinger, W. Birkfellner, F. Wanschitz, W. Millesi, C. Schopper, K. Sinko, K. Huber, H. Bergmann, and R. Ewers. Positioning of dental implants using computer-aided navigation and an optical tracking system: Case report and presentation of a new method. *Journal of Cranio-Maxillo-Facial Surgery*, 27(2):77–81, apr 1999.

[Wil06] Emmanuel Wilson. Accuracy analysis of electromagnetic tracking within medical environments. *CAIMR TR-2006-2 Technical Report*, page 10, 2006.

[WMH06] Xiaona Wang, Max Q-H Meng, and Chao Hu. A localization method using 3-axis magnetoresistive sensors for tracking of capsule endoscope. In *Engineering in Medicine and Biology Society, 2006. EMBS'06. 28th Annual International Conference of the IEEE*, pages 2522–2525. IEEE, 2006.

[WTF04] Andrew D Wiles, David G Thompson, and Donald D Frantz. Accuracy assessment and interpretation for optical tracking systems. In *Proceedings of SPIE*, volume 5367, pages 421–432, 2004.

[WYZ+07] Emmanuel Wilson, Ziv Yaniv, Hui Zhang, Christopher Nafis, Eric Shen, Guy Shechter, Andrew D. Wiles, Terry Peters, David Lindisch, and Kevin Cleary. A hardware and software protocol for the evaluation of electromagnetic tracker accuracy in the clinical environment: a multi-center study. *Proceedings of SPIE*, 6509(1):65092T–65092T–11, mar 2007.

[WZD+05] Bradford J Wood, Hui Zhang, Amir Durrani, Neil Glossop, Sohan Ranjan, David Lindisch, Eliott Levy, Filip Banovac, Joern Borgert, Sascha Krueger, Jochen Kruecker, Anand Viswanathan, and Kevin Cleary. Navigation with electromagnetic tracking for interventional radiology procedures: a feasibility study. *Journal of vascular and interventional radiology : JVIR*, 16(4):493–505, apr 2005.

[YR10] Ke Yang and Yibin Ren. Nickel-free austenitic stainless steels for medical applications. *Science and Technology of Advanced Materials*, 11(1):014105, feb 2010.

[YWLC09] Ziv Yaniv, Emmanuel Wilson, David Lindisch, and Kevin Cleary. Electromagnetic tracking in the clinical environment. *Medical physics*, 36(3):876–892, 2009.

[Zac97] Gabriel Zachmann. Distortion correction of magnetic fields for position tracking. In *Computer Graphics International, 1997. Proceedings*, pages 213–220. IEEE, 1997.

Nomenclature

3D Three–dimensional, page 3

AC Alternating Current, page 11

ADC Analog to Digital Converter, page 21

AGWN Gaussian-white noise, page 114

AO Analog Output, page 20

BPF Band–pass Filter, page 6

CMM Coordinate Measuring Machine, page 96

DAC Digital to Analog Converter, page 20

DAQ Data Acquisition, page 15

DMA Direct Memory Access, page 7

DSP Digital Signal Processing, page 21

EMTS Electromagnetic Tracking System, page 1

FFT Fast Fourier Transform, page 69

FG Field Generator, page 2

FIFO First–in–first–out, page 7

FLE Fiducial Localization Error, page 92

FPGA Field Programmable Gate Array, page 6

FRE Fiducial Registration Error, page 92

IGS Image–guided Surgery, page 1

IIR Infinite Impulse Response, page 69

LM Lenvenberg–Marquardt, page 11

ME Mean Error, page 49

OTS Optical Tracking System, page 1

PCB Printed Circuit Board, page 15

Pose Position and Orientation, page 2

RMS Root Mean Squire, page 4

RMSE Root-mean-square Error, page 49

SNR Signal–to–noise Ratio, page 68

SROI Surgical Region of Interest, page 3

TRE Target Registration Error, page 92

US Ultrasound, page 3

VOI Volume of Interest, page 16

List of Publications

Journal Articles

[1] Mengfei Li, Christian Hansen, and Georg Rose. A software solution to dynamically reduce metallic distortions of electromagnetic tracking systems for image-guided surgery. *International Journal of Computer Assisted Radiology and Surgery*, (first online): 11-13, 2017.

[2] Mengfei Li, Tomasz Bien, and Georg Rose. Construction of a conductive distortion reduced electromagnetic tracking system for computer assisted image-guided interventions. *Medical Engineering & Physics*, 36(11): 1496-1501, 2014.

[3] Tomasz Bien, Mengfei Li, Zein Salah, and Georg Rose. Electromagnetic tracking system with reduced distortion using quadratic excitation. *International Journal of Computer Assisted Radiology and Surgery*, 9(2): 323-332, 2014.

[4] Mengfei Li, Tomasz Bien, and Georg Rose. FPGA based electromagnetic tracking system for fast catheter navigation. *International Journal of Scientific and Engineering Research*, 4(9): 2566-2570, 2013.

[5] Mengfei Li, Christian Hansen, and Georg Rose. A Simulator for Advanced Analysis of a 5-DOF EM Tracking Systems in use for Image-guided Surgery. *International Journal of Computer Assisted Radiology and Surgery*, (revised version in pending): 11-13, 2017.

Conference Proceedings

[1] Mengfei Li, Christian Hansen, and Georg Rose. A robust electromagnetic tracking system for clinical applications. *Deutschen Gesellschaft für Computer-und Robeterassistierte Chirurgie*, in Bremen, Session of Excellence: p.31-36, 2015.

[2] Mengfei Li, Tomasz Bien, and Georg Rose.Developing an electromagnetic tracking system with reduced distortions basing on LabVIEW FPGA. *Image-Guided Interventions*, in Magdeburg, p.35-36, 2014.

[3] Tomasz Bien, Mengfei Li, Zein Salah, and Georg Rose.Distortion-immune electromagnetic tracking system - a new approach using quadratic excitation. *Computer assisted radiology and surgery*, in Heidelberg, p.137-138, 2013.

[4] Mengfei Li, Tomasz Bien, and Georg Rose. (Abstact) FPGA based electromagnetic tracking system for fast catheter navigation. *Design of Medical Devices (Europe Edition)*, in Delft, p.7, 2013.